UNIVERSITY OF ANBAR
1987 1408

EXPERIMENTAL INVESTIGATION OF THE HEAT TRANSFER ENHANCEMENT IN A PARABOLIC TROUGH SOLAR COLLECTOR USING NANOFLUIDS

A Thesis
submitted to the College of Engineering of University of Anbar in partial fulfillment of the requirements for the Master Degree of Science in Mechanical Engineering

By
Tahseen Ali Salih
(B.Sc. in Mechanical Engineering - 2004)

Supervised by

Asst. Prof Dr. Haitham K. Dawood

Asst. Prof Dr. Sattar A. Mutlag

2021 A.D   1443 A.H

بِسْمِ اللَّهِ الرَّحْمَٰنِ الرَّحِيمِ

﴿ وَلِيَعْلَمَ الَّذِينَ أُوتُوا الْعِلْمَ أَنَّهُ الْحَقُّ مِن رَّبِّكَ فَيُؤْمِنُوا بِهِ فَتُخْبِتَ لَهُ قُلُوبُهُمْ ۗ وَإِنَّ اللَّهَ لَهَادِ الَّذِينَ آمَنُوا إِلَىٰ صِرَاطٍ مُّسْتَقِيمٍ ﴾

صدق الله العظيم

الحج ﴿54﴾

Supervisor's Certification

We certify that this thesis entitled **"Experimental Investigation of The Heat Transfer Enhancement in a Parabolic Trough Solar Collector Using Nanofluids"** was prepared under our supervision at the college of Engineering /University of Anbar in partial fulfillment of the requirements for the degree of **Master of Science in Mechanical Engineering**.

Asst. Prof. Dr. Haitham Kamil Dawood

Supervisor

/   / 2021

Asst. Prof. Dr. Dr. Sattar Abed Mutlag

Supervisor

/   / 2021

In view of the available recommendation, I forward this thesis for debate by the **Examining Committee.**

Asst. Prof. Dr. Saad Mohammed Jalil

Head of the Mechanical Engineering Department

/   / 2021

Linguist Certification

This is to certify that I have read the thesis titled **" Experimental Investigation of The Heat Transfer Enhancement in a Parabolic Trough Solar Collector Using Nanofluids"** and have corrected grammatical mistake that found. Therefore, the thesis is qualified for debate as far as language is concerned.

Dr. Arz Yahya Qwam Alden

/   / 2021

Committee Certification

We certify, as an Examining Committee, that we have read this thesis entitled **"Experimental Investigation of The Heat Transfer Enhancement in a Parabolic Trough Solar Collector Using Nanofluids"** and examined the student **"Tahseen Ali Salih"** in its content and what related to it, and found it adequate for the standard of a thesis for the degree of **Master of Science** in **Mechanical Engineering.**

Asst. Prof. Dr. Mohammed Abed Ahmed

(Chairman)

/   / 2021

Asst. Prof. Dr. Basim Hammed A. Freegah   **Dr. Kadhum Ahmed Abed**

(Member)   **(Member)**

/   / 2021   /   / 2021

Asst. Prof. Dr. Haitham K. Dawood

(supervisor and Member)

/   / 2021

Asst. Prof. Dr. Sattar A. Mutlag

(supervisor and Member)

/   / 2021

Approved by the College of Engineering / Al- Anbar University

Asst. Prof. Dr. Ameer Abdulrahman Hilal

Dean of the College of Engineering

/   / 2021

DECLARATION

I hereby declare that this thesis, submitted to mechanical engineering department at University of Anbar as a requirement for master degree has not been submitted as an exercise for similar degree at any other universities. I also support this work that is qualified here is entirely my own except for excerpts and summaries whose sources are congruently cited in the references.

Tahseen Ali Salih

2021

Abstract

The fabrication of a parabolic trough solar collector system has been experimentally designed and tested to improve of the thermal performance of the parabolic trough solar collector. Three working fluids were used water, distilled water with copper oxide nanoparticles, distilled water with titanium dioxide nanoparticles with a volume concentration of 0.02.

Experimental tests are conducted at the University of Anbar-Ramadi (32.559°N - 41.9196°E) during selected days from January 2021 to March 2021. The performance of the PTSC system is evaluated using three main indicators outlet water temperature, useful energy and thermal efficiency. The influence of mass flow rate ranges from (30 to 80) L/hr. In parallel, an artificial neural network has been proposed to predict the thermal efficiency of parabolic trough solar collector depending on the experimental results. An artificial neural network model consists of four inputs and one output parameter, the input parameters include inlet water temperature, solar density, ambient temperature and receiver temperature. While the output parameter includes thermal efficiency. Two neural network models (4-2-2-1) and (4-9-9-1) are built by using MATLAB. The experimental results show that distilled water with copper oxide nanoparticles and distilled water with titanium dioxide nanoparticles have higher thermal performance than water. Overall, it is verified that distilled water with titanium dioxide nanoparticles achieved an enhanced thermal efficiency of PTSC around 7.12% while the maximum increase in thermal efficiency around 19.2% is recorded for distilled water with copper oxide nanoparticles compared to water.

List of Contents

Contents	Page No.

CHAPTER FOUR:

IV

List of Figures

List of Tables

Nomenclatures

Symbols	Definitions	Units
A_a	Collector aperture area	m²
A_c	Cross-sectional area of the flow	m²
A_r	Surface area of the receiver	m²
A_s	Surface area of the concentrator	m²
C_p	Specific heat capacity of water	J/kg.˚C
d_r	Diameter of absorber tube	m
d_h	Hydraulic diameter	m
f	Friction factor	-
H_p	Height of the parabola	m
h	Average heat transfer coefficient	W/m².˚C
I	Direct beam solar irradiation	W/m²
K	Thermal conductivity of fluid	W/m.˚C
L	Length of absorber tube	m
$\dot{m}$	Mass flow rate	kg/s
SWH	Solar water heating	-
Nu	Nusselt number	-
P	Wetted perimeter of the flow	m
Q_s	Solar energy	W
Q_u	Useful heat gain	W
R	Ratio of arc-plug radius to the receiver radius	-
Re	Reynolds number	-
T	Temperature	˚C
U	Velocity of fluid	m/s
V	Volumetric flow rate	m³/s
W_a	Aperture width	m

Greek Symbols	Description	Units
μ	Viscosity of working fluid	$N.s/m^2$
η_{th}	Thermal efficiency	-
ρ	Fluid density	kg/m^3
ΔP	Pressure drop	Pa
$\varnothing$	Latitude angle	Degree
ω	Hour angle	Degree
δ	The sun's declination angle	Degree
θ_z	Zenith angle	Degree
α	Altitude angle	Degree
γ_s	Azimuth angle	Degree
Φ_r	Rim angle	Degree
Φ_m	Half acceptance angle	Degree
λ	Wavelength	Degree
φ	nanofluid concentration	-

List of Subscripts

Notation	Description
a	Aperture
ri	Inner receiver
ro	Outer receive
out	Outlet
in	Inlet
m	Mean
r	Receiver
s	Surface
n_f	Nanofluid
np	Nanoparticles
bf	Base fluid
f	Fluid
z	Zenith
u	Useful
th	Thermal
max	Maximum
min	Minimum

List of Abbreviations

Abbreviation	Description
Al_2O_3	Aluminum oxide
ANFIS	Adaptive neuro-fuzzy interface system
ANN	Artificial neural network
COG	Center of gravity
CuO	Copper oxide
CR	Concentration ratio
D_{12} Oil	H2O oil
FIS	Fuzzy inference system
Ag	Silver
Cu	Copper
MBE	Mean bias error
MFs	Membership functions
MLP	Multilayer layer perceptron
Au	Gold
PTSC	Parabolic trough solar collector
TiO_2	Titanium oxide
R2	Maximum correlation coefficient
RMSE	Root mean square error
SWHS	Solar water heating system
PV	Photo voltage
RPF	Radial basis function
EBP	Elman back propagation
GA	Genetic algorithm
GMDH	Group Method of Data Handling
AI	Artificial intelligence
UV	Ultraviolet radiation

CHAPTER ONE

INTRODUCTION

CHAPTER ONE

INTRODUCTION

1.1 Background

Solar radiation is the most evenly distributed energy resource on earth and the most abundant. The sun constantly emits a huge amount of radiant energy in the solar system. Earth intercepts a small portion of this energy with an average of 1,367 watts per square meter [1]. Solar energy is converted into two types of energy. The first technique is defined as a Photovoltaic (PV) solar cell that converts the solar energy into DC electrical energy. This energy either used directly or stored in batteries and then converted to AC energy. While, the second techniques are summarized as a solar thermal system which turn the solar energy into thermal energy so as to generate mechanical energy and thus generating electricity[2]. Solar Water Heating System (SWHS) is a simple system that captures energy from solar radiation falling on it, which is converted into heat energy for the fluid passing through it, which can be used for domestic, commercial or industrial purposes [3]. SWHS consists of several parts, one window is one of the most important parts is solar collector. In general, there are two types of solar thermal collectors: stationary (non-concentrating) solar thermal collectors and solar tracking (concentrating) solar thermal collectors[4]. A non-concentrating collector is permanently fixed in position and do not track the sun besides the area for intercepting and absorbing solar radiation is the same. Whereas, the tracking concentrating solar collector usually has concave reflecting surfaces to intercept and focus the suns beam radiation to a smaller receiving area, hence increasing the radiation flux. Solar concentrating collectors are distinguished by their motion (single or two-axis tracking) and by their operating temperature [5]. These types of collectors permit to gather the

solar radiation on a concentrated area for increasing the thermal energy. The principal operation of these solar collectors is used with devices like Stirling motors, heating systems, solar kitchens, and vapor turbines or photovoltaic cells [6]. As a result, the concentrator is making from a high-reflectance material that permit to collect the solar radiation components (visible radiation, infrared and ultraviolet rays). In addition, the concentrators should be directed towards the sun by using solar tracker to correct their function. All the concentrators have the same operating principle, but present differences regarding geometry, amount of energy concentrated, and how the energy is used [5, 6].

1.2 Parabolic Trough Solar Collector

The parabolic trough solar collector (PTSC) is a widely used in the world among the concentrated solar power systems, John Erksson creates the first collector parabola in 1880, which is used to power a hot air engine. Also, a parabola had also been devised by Germans Wilhelm Meier and Adelf Remshardt to generate steam [7]. PTSCs are the most attractive technology used in solar thermal power generation, as well as in industrial processes such as drying, sterilization and seawater desalination, cooling and air-conditioning, steam generation (for electricity power-plants), production of hot water for domestic and industrial use and production of hydrogen gas [8]. The PTSC unit is made up of a parabolic trough that concentrates solar beam radiation into the receiver tube and a protective glass enclosure that reduces losses and protects the tube from external climate restrictions, as shown in Figure 1.1. A solar tracking device is also included with the collector to ensure that the solar beam falls perpendicularly on the aperture region. Most commercial PTSC plants, according to state of the art PTSC technology, run at temperatures up to 400 °C

with synthetic oil as the working fluid [7,8]. One of the most considerable challenges in the PTSC is the thermal efficiency enhancement in order to produce higher amount of useful heat, especially in higher temperature levels. Thus, a lot of researchers have been focused on various techniques which can enhance the performance of PTSC. These techniques usually aim to increase the heat transfer coefficient between the fluid and the absorber tube in order to achieve high useful heat rates [9].
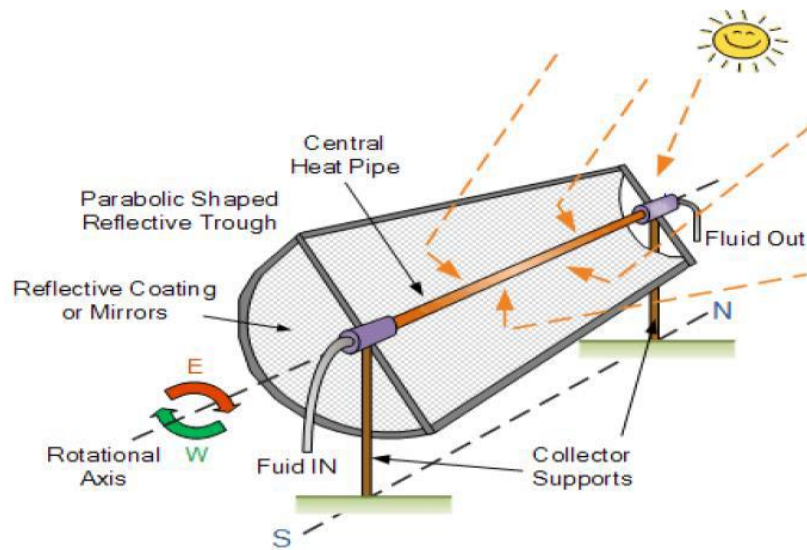
Figure 1.1: The main components of parabolic solar collector [10].

1.3 Solar Radiation Types

The ultraviolet radiation (UV) radiations are absorbed by the Ozone layer and infrared radiations are absorbed by the water vapors, and carbon dioxide. So the intensity of radiation reaches the earth decreases. Radiations reaches on the earth are [11].

1.3.1 Diffuse Solar Radiation

 Diffuse solar radiation is called as the results of absorbing, scattering and reflecting of the sunlight due to its passing through the atmosphere [11].

1.3.2 Direct (beam) Solar Radiation

Direct solar radiation is solar radiation that reaches the earth's surface without being dispersed. It's also known as solar radiation that travels along the line connecting the receiving surface to the sun. Direct beam radiation can be reduced by 10% on clear, dry days and by 100% on heavy, cloudy days due to atmospheric circumstances. The solar constant (I_r)is the radiant energy flux received per second by a surface of unit area kept normal to the direction of the sun's beams at the mean earth sun distance outside the atmosphere. Its approved value of 1367 W/m^2 is largely stable throughout the year [11].

1.3.3 Methodology of Earth-Sun Angle

There are several basic angles between the sun and the earth as shown in Figure 1.2. The following are the important sun-earth angles [12]:

a. Zenith angle (θ): It is the angle between sun's ray and perpendicular line to the horizontal plane.

b. Altitude angle (α): It is defined as the angle between sun rays and a horizontal plane.

c. Surface Azimuth angle (γ): It is the angle in a horizontal plane, between the line due south and the projection of normal to the surface on the horizontal plane.
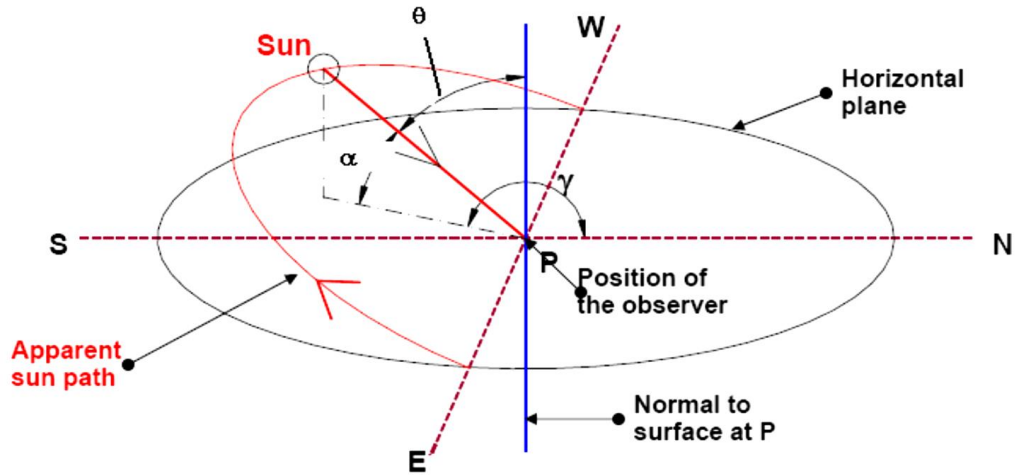
Figure 1.2: Sun and Earth angles [12]

1.4 Mathematical Model of Design the PTSC

The design parameters of PTSC are calculated from the geometric relations of the parabolic reflective surface, the angle of incidence of sunlight and the receiver tube[13]. As shown in Figure 1.3.
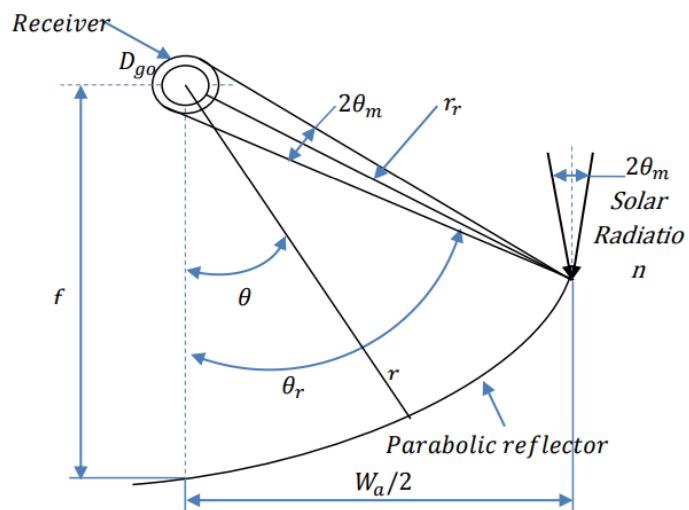
Figure 1.3: Design specifications of a parabolic reflector [13].

The concentration ratio is defined as the ration between the area of reflector to the area of receiver that is given by:

$$CR = \frac{A_a}{A_r} = \frac{W_a l}{\pi D l} = \frac{W_a}{\pi D} \qquad (1.1)$$

Rim angle is given by:

$$\Phi_r = \sin^{-1}\left(\frac{W_a}{2\,r_r}\right) \qquad (1.2)$$

For any point of the parabolic reflector, the local mirror radius is represented as:

$$r = \frac{2\,F}{1+Cos\Phi_r} \qquad (1.3)$$

Aperture width is given by:

$$W_a = 4\,F\,\tan\frac{\Phi_r}{2} \qquad (1.4)$$

The Focal length can be represented as:

$$F = \frac{W_a}{4\tan\left(\frac{\Phi_r}{2}\right)} \qquad (1.5)$$

The vertical height of the parabola is given by:

$$H_p = \frac{W_a^2}{16\,F} \qquad (1.6)$$

Arc length of parabolic curve (the curve length of the parabolic surface):

$$s = \frac{H_p}{2}\left\{Sec\left(\frac{\Phi_r}{2}\right)\tan\left(\frac{\Phi_r}{2}\right) + \ln\left[Sec\left(\frac{\Phi_r}{2}\right)\tan\left(\frac{\Phi_r}{2}\right)\right]\right\} \qquad (1.7)$$

The half acceptance angle is given by:

$$\Phi_m = \sin^{-1}\left(\frac{D}{2r_r}\right) \qquad (1.8)$$

1.5 Mathematical Model of Heat Transfer Analysis in PTSC

The heat transfer process deals with the transfer of solar radiation from the sun to the absorber and then transfer the heat from it to the receiver as shown in Figure 1.4. Generally, the heat transfer depends on the coefficient of heat convection [14].
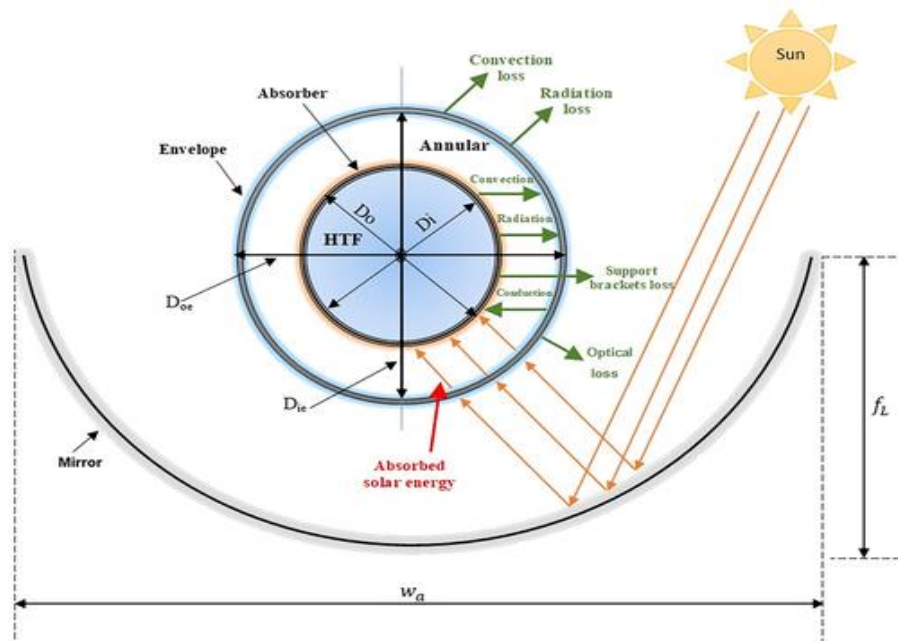
Figure 1.4: The schematic cross section of a typical PTSC [14]

The resultant of the collecting area (A_a) and the direct beam solar irradiation I is used to determine the solar energy Qs incident on the collector aperture, as shown in the equation below [15]:

$$Q_s = A_a\, I_r \tag{1.9}$$

Where: Aa is the collecting area of receiver (m^2) and defined as:

$$A_a = (W_a - d_{ro})L \tag{1.10}$$

Water in the absorber tube obtained useful energy rate Q_u from the solar radiation mainly through the process of convective heat transfer. Thereby, Qu

was assumed to be equal to the heat flow convective inside the test tube and can be expressed as [16]:

$$Q_u = \dot{m} \, C_p \, (T_{out} - T_{in}) \tag{1.11}$$

$$\dot{m} = \rho \, \overset{\circ}{V} \tag{1.12}$$

The most important index for the solar water collectors' evaluation is their thermal efficiency η_{th}. This parameter is calculated as the ratio of the useful energy to the solar energy available, as indicated below by equation [17]:

$$\eta_{th} = \frac{Q_u}{Q_s} = \frac{Q_u}{A_a \, I_r} \tag{1.13}$$

$$A_r = \pi \, d_{ri} \, L \tag{1.14}$$

$$T_m = \frac{(T_{in} + T_{out})}{2} \tag{1.15}$$

$$T_r = \frac{T_{s1} + T_{s2} + T_{s3}}{3} \tag{1.16}$$

Reynolds number *Re* for circular tube for the PTSC system was expressed as [18]:

$$u_m = \frac{4 * \overset{\circ}{m}}{\pi * \rho * d_{ri}^2} \tag{1.17}$$

$$Re = \frac{\rho \, u_m d_{ri}}{\mu} = \frac{4 \, \dot{m}}{\pi \, d_{ri} \, \mu} \tag{1.18}$$

$$A_C = \frac{\pi \, d_{ri}^2}{4} \tag{1.19}$$

The friction factor *f* can be calculated using the pressure drop *ΔP* along the tube [19]:

$$f = \frac{\Delta P}{\frac{1}{2}\rho \, u^2} \frac{d_{ri}}{L} \tag{1.20}$$

1.6 Nanofluids

Nanofluid technology is considered to be one of the main emerging technologies currently attracting significant research efforts in thermal engineering. The main goal of this technology is to improve the thermal characteristics (heat transfer coefficient) of the working fluids and then produce a high heat flux generating devices for effective thermal dissipation [20]. Nanofluides are formed by dispersing the powdered nanoparticles in the base fluid. Various nanoparticle materials involve metals (Cu, Ag, Au), nitride ceramics (AlN, SiN), ceramic oxide (Al_2O_3, CuO), carbide ceramics (SiC, TiC) and semiconductor (TiO_2 and SiO_2). The main important parameters that are affected on the heat transfer process in fluid with nanoparticles are viscosity, thermal conductivity, density and specific heat [21].

There are several steps must be taken in consideration to prepare the nanofluids. For example, good dispersion, surfactants to enhance the stability of nanofluids, modification of the dispersed particles and application of strong force on the clusters of the dispersed nanoparticles to increase the stability of nanofluids. One of the main conditions for obtaining a usable nanofluid is the stability of nanoparticles in a conventional fluid. To produce an even and stable suspension, several techniques are applied, such as the use of ultrasonic equipment, pH control or addition of stabilizers [22, 23]. The van der Waal force causes nanoparticles to stick together while suspended in liquids. This force prevents the nanoparticles from settling in the base liquid and thus prevents the formation of a homogeneous mixture. To solve this problem, chemical or physical treatment should be used such as modifying the surface of suspended particles, adding surfactant or applying strong force to the suspended particle assemblies, since the thermal conductivity of nanofluids is greatly improved due to their stability [24].

1.7 Problem Statement

One of the most important requirements for most solar energy research is to improve thermal efficiency, and in order to obtain as much energy as possible and for the purpose of increasing the heat gain and enhancing the heat transfer to the working fluid used in the concentrated solar collector used in this research. Concentrated solar energy systems are considers one of the important applications in heat transfer analysis. The individual analysis of the physical associated with solar collectors is easy, but also it is very difficult in the case of the whole system analysis. It is very difficult to understand the behavior of the parameters of the solar system with each other, due to the complexity of the processes that are related to the atmosphere and solar radiation and not subject to a static state. As well as, the large variability of measurement according to the time and place in which the experiment is performing. Most of the data obtained of solar energy systems are not correlate; therefore, these data are treating as physical models to predict thermal performance. Where, the data of the current experiment can be used to develop a model based on artificial neural networks. The application of ANN analysis is encouraged to the difficult and critical problems of solar energy systems due to recent developments in ANN methodology and good results. And use this data in several models of neural networks to determine the best model to implement the behavior of this system.

1.8 Aim and Objectives

The main aim of the current investigation is to evaluate thermal efficiency of the PTSC using artificial neural network model with nanofluids.

The current study has the following objectives:

1. To investigate the effect of working fluid on the heat transfer enhancement in parabolic trough solar collector (PTSC).

2. To study the effect of volumetric flow rate on the flow and thermal characteristics of PTSC.

3. To determine the effect of local time on the performance of PTSC

1.9 Scope of Current Study

 The scopes of this study that used to achieve the above objectives are:

1- The experimental is conducted at four different mass flow rates of 30 L/hr to 80 Lt/hr and corresponding Reynolds number was calculated in the ranges of 500 to 1500.

2- Reflected Concentration was metal of Nickel-Chrome sheet, Aperture area A=2 m², Focal distance F=0.24 m.

3- Using nanofluid with CuO and TiO$_2$ nanoparticle volume fraction in the range of 0.02%, and nanoparticles diameter in the range of 30 nm on the heat transfer characteristics and thermal performance of the PTSC system.

1.10 Thesis Outlines

The significance and objectives of this project are disclosed in the next section of this chapter. Additional information is discussed in the balance of this thesis to achieve its objectives. This thesis is divided into five chapters

Chapter Two: Describes the literature review of topics related to this thesis. The literature studies were divided according to the main objective investigated in the study including a simple introduction to the chapter. This chapter also includes short writings on enhancing the efficiency of solar collectors using water as a working fluid. In addition, a summary is written about solar collectors using nanofluid as a working fluid. Finally, a summary of the literature discussed in this research.

Chapter Three: Deals with the materials and project description, that are included research requirements, preparation of nanofluids, system description and its installation. The experimental setup components are described in details. This chapter also includes data acquisition and experimental setup. Finally, the methodology of Artificial Neural Networks (ANNs) is discussed, including the definition, structure and architecture of Artificial Neural Networks

Chapter Four: Surveys and discusses the experimental and ANN results. Comparisons between the experimental results with the predicted results of ANN are presented.

Chapter Five: Concludes the thesis results and provides suggestions for future studies in this field to improve and develop the behavior and performance of PTSC system.

CHAPTER TWO
LITERATURE REVIEW

CHAPTER TWO

LITRETURE REVIEW

2.1 Overview

This chapter introduces the previous studies that are related to the topic of present thesis. There are a lot of the numerical and the experimental studies are investigated to analyze the thermal performance of parabola trough solar collector (PTSC) systems. In addition, the (ANNs) has taken up a fair number of studies about predicting the Thermal Efficiency (η) of solar thermal systems. Therefore, the outlines of this chapter will be survey according to the main objectives and goals of the previous studies in literature. Then, this chapter divided into three main sections as below.

2.2. PTSC System with Water

Alzahrani and Khaled [25] conducted an experimental study on a parabolic solar collector in Saudi Arabia using a unidirectional tracking system. The main characteristics of their study were: the sensor area about was 175 m^2, the receiver tube from glass with 3 cm inner diameter and tested at water mass flow rate about 0.03 kg/s. The experimental results show that the maximum overall efficiency was 38.3%.

Wahiba and Evgueniy [26] investigated the applicability of adaptive neuro fuzzy inference system (ANFIS) approach to predict the performance of a solar thermal energy system depending on a set of experimental data. The ANFIS were predicted values and found to be quite close to the experimental values with mean relative errors of less than 18% and 3.26 %, respectively, for the warmup tank stratification temperatures and sunlight percentages. Finally, the

findings showed that the ANFIS method was useful and reliable in predicting the performance of energy systems.

Kajavali et al. [27] investigated an experimental study to compare between a single tube absorber and a modified absorber that was constructed from scratch. The experimental tests showed that the adjusted absorber was recorded a higher solar energy recovery efficiency than a single tube where its efficiency was about 42.1%.

Valenciaa et al. [28] designed and tested a PTSC model in dimensions of 95 cm long and 50 cm wide with a uniaxial solar tracking unit. The highest outlet temperature was recorded about 47.3°C in a constant flow rate of 0.2 L / min and solar irradiance of 783.58 W/m^2 at 13 pm.

Sivaram et al. [29] conducted experimental and numerical study to investigate the efficiency of a small-sized basin solar collector integrated with a thermal energy storage device. The thermal storage capacity contains 60 liter from phase change material (paraffin). The PTSC system consists from a collector with 3 m length, an aperture area of 7.5 m^2 and a focal distance of 0.976 m. Furthermore, the output parameters estimated from the numerical model were compared to the experimental outputs with deviations less than 10%.

Tajik et al. [30] investigated an experimental study to improve the heat transfer and to increase the efficiency of a PTSC system using an absorber filled with the metal of copper foam. Their study was dealt with two different absorbers. The first one was a copper tube with black chrome coating with metal foam and the second one without metal foam. Water was used as a working fluid in different mass flow rate (0.5 to 1.5) L/min and Reynold number (500 to 2500). The experimental tests showed that the overall loss coefficient decreases by

45% in case of absorber filled with metal foam and then lead to increase the efficiency by 3%.

Fahim et al. [31] performed an empirical study to improve the heat transfer of PTSC using solar tracking system. The dimensions of collector were 2.44 m length, 1.04 m width and a focal length of 0.004 m. the absorber tube was selected from aluminum with 2 cm inner diameter. The sun falling onto the reflecting surface improves the heat transfer and thus the amount of distilled water produced.

Debnath et al. [32]Carried out an experimental study of flat solar collector modeling and improvement by predicting the performance of solar air flat collector using the ambiguous integrated fog method. Parameter input layer from they are the solar radiation, the air mass flow rate, and ambient temperature and collector tilt angle. The output parameters were energy efficiency, thermal efficiency, and temperature rise and the pressure drop. The ifm model was they have been validated in order to demonstrate the reliability and accuracy of the model. The results obtained they correlated with experimental results with an accuracy of 95.5%. Moreover, the the results were validated using the confirmatory method with experimental data, artificially generated data and published data. The accuracy of the result obtained the solar air collector was 97.5%

Abiem and Akoshile [33] designed and tested a PTSC to obtain output temperatures up to 150 to 350 ℃. Parabola equation was used to design the collector and manufactured from locally available materials. The results were recorded a high output temperature about 105 °C at a pressure of 120 kpa. In the same manner, the highest efficiency was recorded about 46.48%.

Harish et al. [34] used an artificial neural network and pertinent input parameters. The thermal performance of two different types of solar air heaters (arc shaped wire rib) and (smooth duct) were predicted. The following nine input parameters were selected in this study (mass flow rate, solar intensity, ambient air temperature, solar elevation, inlet air temperature, wind direction, air mean temperature, plate temperature and relative humidity). While, the output parameter was performance of the system. The prediction results found that the structure of ANN-II with (8-14-1) was the optimal model as compared to other models. The values of MRE, SSE and R^2 were found to be 1.82%, 0.0213 and 0.9938 respectively.

2.3 PTSC System with Nanofluids

Wang et al. [35] presented a three-dimensional a numerical simulation to improve the performances of the PTSC system using Al_2O_3/synthetic oil as a nanofluid with non-uniform heat flux distributions. The numerical study was taken in consideration the influence of six different volumetric concentrations of Al_2O_3 with size 28 nm on the thermal performance of PTSC. As compared with traditional PTSC, using Al_2O_3/synthetic oil nanofluid enhanced and improved the heat transfer and thermal performance.

Mwesigye et al. [36] presented a numerical study to analyze the thermodynamic performance of a PTSC system using Cu-Therminol nanofluid as the working fluid. According to the conditions of study such as inlet temperature (350–650) K, Reynolds number ($20x10^4$ to $300x10^4$), and flow rates (1.22-135) m³/h, the thermal efficiency of the system was increased by 12.5% when the nanoparticle volume fraction increased to 6%.

Menbari et al. [37] investigated an experimental and numerical study to improve the thermal performance of direct absorption PTSC using CuO-water nanofluid nanofluid with a volume fraction (0.002 to 0.008) % with size <100 nm. The results showed that the thermal efficiency of the system directly depended on the nanoparticle volume fraction. Where, the efficiency of the system was increased from 18 to 52 % when the volume fraction was increased from (0.002 to 0.008) %.

Subramani et al. [38] presented an experimental study to investigate thermal performance and heat transfer characteristics of a PTSC system using Al_2O_3/water nanofluids as working fluid. The experimental tests under different nanofluid concentration, particles size, and mass flow rate showed that the maximum efficiency was recorded 55.8 % at mass flow rate and volume concentration (m= 0.05 kg/s and φ= 0.5 %).

Mwesigye and Meyer [39] investigated a numerical study to analyze the thermal efficiency and thermodynamic performance of a PTSC system using copper-Therminol®VP-1, silver-Therminol, and Al_2O_3-Therminol nanofluids as working fluid. The analysis was take in account the effect of mass flow rate, inlet temperature, nanoparticle concentration and Reynolds number. The results showed that the using of nanofluids improve the thermal efficiency and thermodynamic performance of a PTSC system. So, heat transfer coefficient was increased by 7.9 %, 6.4 % and 3.9 % while, the thermal efficiency of the PTSC system was increased by 13.9%, 12.5% and 7.2% for silver-Therminol®VP-1, copper-Therminol and Al_2O_3-Therminol nanofluids, respectively as the volume fraction increased from 0 to 6 %.

Bellos and Tzivanidis [40] presented a numerical study to investigate thermal efficiency enhancement of PTSC system using hybrid and mono nanofluid by using Syltherm 800 as the base fluid. Nanofluids was used: 3 % TiO_2/Oil, 3 % Al_2O_3/Oil, and 1.5 % Al_2O_3-1.5% TiO_2/Oil. According to the final results, Hybrid nanofluids was provided a greater increase in thermal efficiency when compared to other working fluids. The enhancement in the heat coefficient was found 35.2 % for the TiO_2 nanofluid, 142.1% for the hybrid nanofluid and 34.9 % for the Al2O3 nanofluid. The enhancement in the Nusselt number was found 23.8% for the TiO_2 nanofluid, 121.7% for the hybrid nanofluid and 23.4% for the Al_2O_3 nanofluid. The thermal efficiency enhancement with the TiO_2 nanofluid 0.341 % while with the hybrid nanofluid was found 0.74 % and with the Al_2O_3 nanofluid 0.340 %. Thus, the enhancement is approximately 10%, which is due to the increased thermal conductivity of the nano-fluids (nano-oil) compared to the pure oil.

Bellos and Tzivanidis [41] presented a numerical study to investigate the thermal efficiency of a PTSC system using various nanoparticles (SiO_2, Cu, Al_2O_3, CuO, TiO_2 and Fe_2O_3) dispersed in thermal oil (Syltherm 800). The most efficient nanoparticles, according to the results, was Cu, followed by CuO, Fe_2O_3, TiO_2, Al_2O_3, and SiO_2. Lower flow rates, higher inlet temperatures, and larger nanoparticle concentrations were all reported to result in greater enhancement. For Cu concentrations of 2, 4, and 6%, the enhancement of thermal efficiency was found to be 31, 54, and 74%, respectively.

Subramani et al. [42] presented an experimental study to investigate the influence of TiO_2/DI-H_2O (De-Ionized water) on the efficiency of a PTSC system. The results show that the convective heat transfer coefficient was improved up to 22.76 % by using TiO_2 nanofluids. The maximum overall

efficiency of the PTSC was recorded 57% when using TiO_2 nanofluid which is 9 % greater than that of the base fluid.

Bellos et al. [43] presented a numerical analysis to investigate CuO nanoparticle dispersion in Syltherm 800 and nitrate molten salt (60 % $NaNO_3$-40 % KNO_3) with a volume fraction of 6%. The use of oil-based nanofluids improves thermal efficiency by up to 0.76 % to a pure fluid, according to the final results. On the other hand, the results showed that using Syltherm 800-CuO gives an average thermal enhancement of 0.65% compared to pure Syltherm, while using CuO molten salt leads to only 0.13% of the average thermal efficiency.

Soledad et al. [44] investigated an experimental study to analyse the thermal efficiency of a PTSC system using Al_2O_3/water nanofluid with a volume fraction of 1% and 3%. The tests were run for different values of inlet fluid temperature and ambient temperature. The results showed that using the nanofluids instead of water as the working fluid of the PTSC improved its thermal efficiency. The nanofluid with a 3% volume fraction reached the maximum efficiency of 52.4 %, whereas in the case of water, this value was 40.8 %. While, in case of 1% volume concentration, a maximum efficiency was reached to 57.7 %, while in case of the water was 46.5 %.

Milad et al. [45] carried out an experimental study to predict the efficiency of a flat-plate collector using three methods of machine-learning. These methods were defined as: a Radial Basis Function Artificial Neural Network (RBF-ANN), Multi-Layers Perceptron Artificial Neural Network (MLP-ANN), and Elman Back Propagation Neural Network (Elamn BP-ANN). The experiment tests were done using TiO_2 (30 nm)/water nanofluids, mass flow rate, inlet temperature and the weight concentration of nanofluid. While, the thermal efficacy was considered the output data. The results revealed that all of these

machine learning algorithms were suitable for predicting nanofluid thermal performance in solar systems. However, as a compared between the three methods, the MLP-ANN was the accurate method for predicting the efficiency of flat-plate solar collector with a value of Coefficient of determination (R^2) about 0.96.

Shahram et al. [46] predicted the performance of a nanofluid-based direct absorption solar collector using artificial neural network (ANN) based Multi-Layer Perceptron (MLP-ANN) system. The parameters that selected as input for the MLP networks were the collector length, depth, working fluid flow rate, concentration and temperature difference. While, the output was the collector efficiency and Nusselt number. The statistical results show that the proposed ANN approach prove that the collector depth has significant effect on the collector efficiency while the collector length had an insignificant effect. On the other side, the depth of collector and nanofluid flow rate had a significant effect on Nusselt number. Generally, a significant concordance between experimental and anticipated was considered. The findings demonstrate the MLP-ANN model's superior ability to predict output data.

Okonkwo et al. [47] used the genetic algorithm (GA) and artificial neural network (ANN) to minimize the entropy generation in a solar parabolic trough collector (PTSC) with SiO_2–water nanofluid as a working fluid. The results showed that the optimal mean square error was 0.02288 for validation stage, 0.02288 for training and 0.0282 for testing with value of R^2 about 0.9999. It was concluded that within the constraints of specific parameters, machine learning techniques could be effective for predicting the rate of entropy generation in a collector.

Ali et al. [48] used three types of basal fluids to predict the thermal conductivity of nanofluids containing CuO nanoparticles. The researchers used the accuracy of the group method to process data for artificial neural network and polynomial correlation. The concentration of nano, thermal conductivity, temperature, and nanoparticle dimension were used as inputs in both models. The values of R^2 were recorded 0.9862 and 0.9996 in cases of polynomial and ANN, respectively. Furthermore, the average absolute relative deviation values for the two approaches were 5.25 percent and 0.881 percent, respectively. These statistics came from statistical analysis, using an ANN-based regression to anticipate the thermal conductivity of nanofluids containing CuO nanoparticles yields a more reliable model.

Gholamabbas et al. [49] presented an experimental study to improve of the thermal performance of an evacuated tube solar collector by using Cu_2O/Water nanofluid. The experiments were conducted out at three different fluid flow rates (10, 30 and 50) L/h with various volume fractions of the Cu_2O/Water nanofluid. Artificial Neural Networks were used to verify the accuracy of the experiment data. The performance of the constructed tubular collector was predicted using the Multi-layer Perceptron (MLP) and Radial Basis Function (RBF) models, respectively. The following three input parameters (nanofluid concentration, tank volume, and flow rate) with two outputs make up the prediction technique (energy efficiency and the difference in temperature of the fluid flowing through the coil). The results showed that the MLP technique might forecast collector performance more accurately than the RBF method. The highest error rate for the MLP model was less than that of the RBF mode. It was also discovered that increasing both the flow rate and concentration of the nanofluid was improved the solar collector's thermal performance.

2.4 Summary Table for Previous Researches

By reviewing the previous literature, it was found that a lot of research has been conducted by researchers in the field of solar energy systems. Heat transfer techniques for solar energy systems are carried out either through the design aspect using a tracking system or changing dimensions, or by using different nanofluids. focus on making simulations of solar energy systems using artificial intelligence techniques Appendix A shows a summary of previous research that was addressed in this research.

CHAPTER THREE

EXPERIMENTAL WORK

CHAPTER THREE

EXPERIMENTAL WORK

3.1 Introduction

The current chapter attempts to describe the experimental parts of this thesis. The description includes the preparation and fabrication of PTSC system components, system installation and nanofluids preparation. Furthermore, the measurements, instrumentations, data acquisition and experimental setup are briefly covered.

3.2 Description of the Parabolic Trough Solar Collector

The PTSC is the model of the system that consists from the following parts: a mechanical part, reflector, heat collection element, and solar tracking system moves in two axes as shown in Figure 3.1.
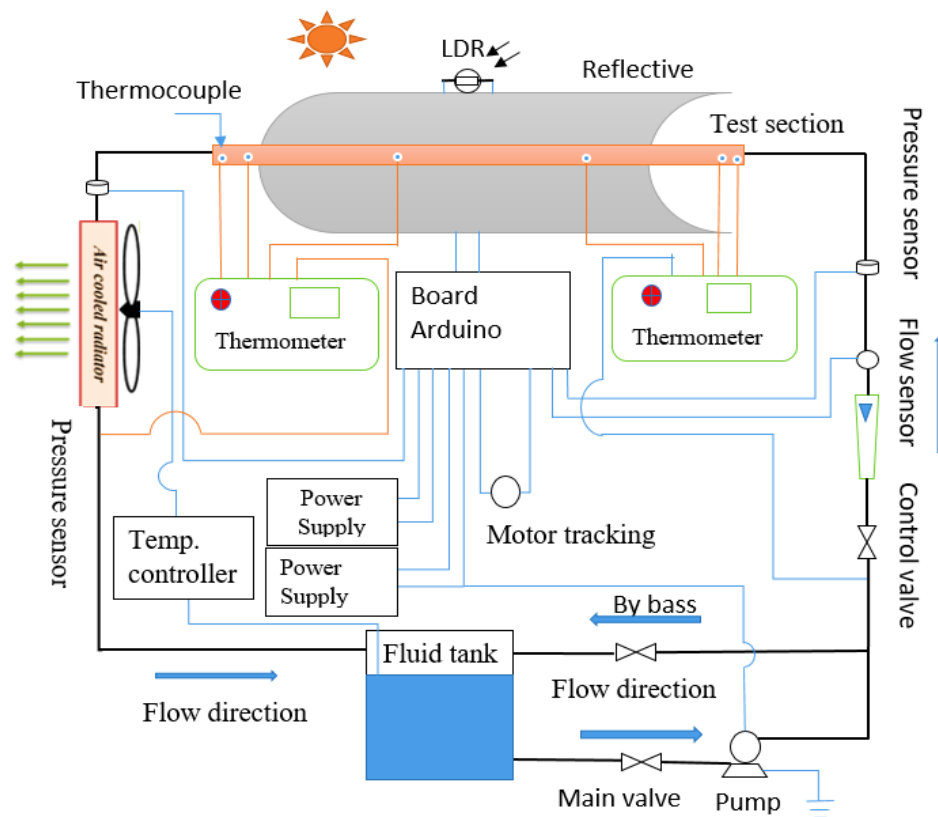
Figure 3.1: Schematic diagram of the experimental

1- Reflective surface   8- pump

2- Receiver   9- Pressure sensor

3- Thermometer   10- Flow meter Sensor

4- Motor tracking   11- Radiator

5- Control Panel   12- Thermocouple

6- Fluid tank   13- LDR

7- By bass

Figure 3.2: Photograph of the experimental.

3.2.1 Design and Manufacture of the Structure Trough

The design and manafcture of the reflective surface arc were depended on the dimensions obtained from the software such as length of the reflector (2 m), the focal length (0.24 m), and the diameter of the reflecting surface (1 m) and the angle of rim 90º as shown in (Appendix B.1). Firstly, the basement of the frame

was made as rectangular section from steel square channel with dimensions (40×20) mm and (20×20) mm as shown in Figure 3.3. To support the reflective surface, the right and left edges of upper structure was manufactured from steel square channel with dimensions (20×20) mm. In addition, four cross arches had been installed along the structure. The arches were fabricated from iron sheet with 4 mm thickness and prepared using CNC machine. For greater durability, three screw of 2 m length and 14 mm diameter were used to connect between the arches.

Figure 3.3: Frame structure of the reflector

3.2.2 Surface of the Reflector

The function of the reflector is to focus the sun's rays on the absorbing tube placed at the focal point of the reflecting surface. There are several types of reflective surface material. In this research, a reflective surface of nickel chrome type was used that is characterized by a good reflectivity for the sun's rays. After taking the required measurements, the reflector was fixed on the iron structure by welding Alarcon Texture as shown in the Figure 3.4.

Figure 3.4: Reflective surface structure

3.2.3 Stationary Part

The function of the stationary part is to hold and support the assembly of reflective surface structure unit. The basement of stationary part was formed as a cross section from iron channel (40×20) mm and length 800 mm. Additionally, four holes with 10 mm diameter was opened at the end of iron channel to support the basement with floor. The vertical axis of stationary part was fabricated and welded with the basement part from iron channel (80×60) mm and 400 mm height as shown in Figure 3.5.a another column was used from iron channel (60×40) mm to control the length of stationary part as shown in Figure 3.5.b.
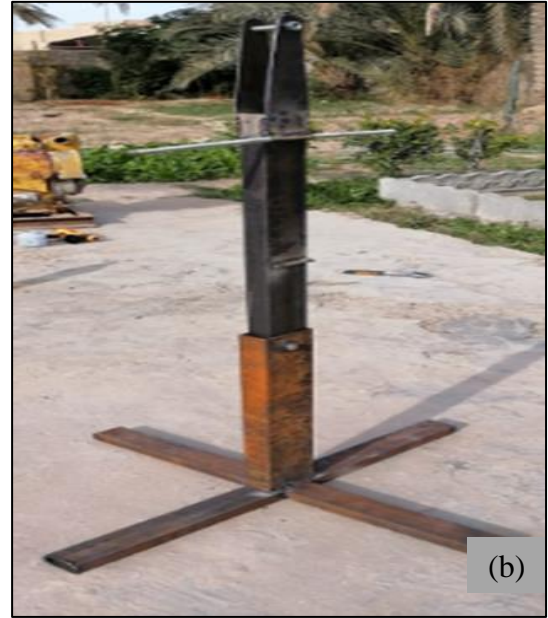
Figure 3.5: (a) Main base and (b) Supporting the main base.

3.2.4 Moving Parts

A moving part as half rectangular was fabricated from channel iron (30×20) mm in length 1800 mm to make the surface of reflector moving in up and down as shown in Figure 3.6. This part was connected to the vertical support using screw in the middle while the its two ends connect to the structures.

Figure 3.6: parts responsible for movement

The second part responsible for the movement of the reflective surface left and right was fabricated from iron channel (30 x 20) mm and was formed as a

rectangle with 1800 mm length and 740 mm width as shown in Figure 3.7.a. It was supported with previous part in Figure 3.7.b using two screws. An electric motor was connected between the fixed vertical support and this moving part to be responsible for movement left and right.

Figure 3.7: (a) Rear view of the reflective surface. (b) Moving part left and right.

3.3 Experimental Equipments or Instruments

3.3.1 Digital Thermometer

A digital thermometer unit model GM-1312 SD was used to collect the measured temperatures using a temperature recorder. Nine K-type thermocouples (-200 to 1372) °C were used and connected to a digital thermometer. The thermocouples were distributed as follows: the first and

second were installed at the inlet and outlet of the tank respectively, the third and fourth were at the inlet and outlet of the copper tube, two thermocouples were used at the inlet and outlet of the heat exchanger. In addition, three thermocouples were installed on the absorbent tube surface. (Appendix C.1) showed the thermometer specifications in more details. Calibration of thermocouples was described in (Appendix D.2).

3.3.2 Solar Cell

A standard PV solar cell was used to measure the intensity of solar radiation by connecting with Arduino. The temperature range of solar cell (-40 to 65) ^{o}C and solar radiation range (0-1500) W/m^2 with an accuracy $\pm$ 0.499%. Solar cell is presented in (Appendix B.2) and more specifications about the solar cell were defined in (Appendix C.2).

3.3.3 Fluid Flow Measurement Sensor

Water flow sensor model YF-S201 with flow rate ranging between (1 to 30) LPM and with an accuracy of about $\pm$10% was installed to measure the water mass flow rate. The water flow sensor operates with maximum liquid temperature and maximum pressure until 120°C and 2 MPa. flow sensor is presented in (Appendix B.2). More details were defined in (Appendix C.3).

3.3.4 Pump

A booster water pump with a maximum flow rate 1.2 m^3/hr, head 12 m and operation power of about 120 W was installed to circulate the water in the system. Pump is presented in (Appendix B.2) more details summarized in (Appendix C.4).

3.3.5 Pressure Sensor

Two pressure sensors type PIA works with a pressure range between (0 to 16) bar were installed at the entrance and exit of the system. The housing material of pressure sensors was 304 stainless steel and supported with the system by using two triple connections. Pressure sensor is presented in (Appendix B.2) for more specifications were defined, (Appendix C.5).

3.4 Electrical System

It is a system of great importance, especially in the solar tracking system, and it consists of:

3.4.1 Electrical Motors

Two electric motors were used to direct the solar collector with appropriate tracking to ensure the sun's rays were perpendicular to the reflecting surface. One of the electric motors was responsible for the linear movement up and down. The second electric motor was responsible for the movement to the right and left. These two motors work with a voltage of 12 volts DC and a rotation speed of 120 revolutions per minute (low rotation speed) as shown in Figure 3.8. The internal structure of this type of motor contains a set of gears to reduce the rotational speed, and high torque. The electric motor was installed on the main fixed headrest by the belt of the motor on the one hand, and on the other hand, it was connected the electric motor to the iron structure responsible for the movement. So, the linear movement of the solar collector in all directions according to the electrical signal received by the electronic part of the movement of the electric motor was considered.

Figure 3.8: Electric motor for tracking.

3.4.2 Light Dependent Resistance (LDR)

The photoresist was used as one of the important parts to control the movement of the solar collector, depending on the intensity of the solar radiation and to ensure that the reflective surface of the solar collector was perpendicular at any moment to the rays of the sun falling on it. The basis of the work of the optical was to resist the changes with the changing of the intensity of the radiation that falling on it. This property could be used for that resistance in solar tracking systems when the intensity of solar radiation increases, its resistance decreases, the optical resistance decreases, and when the intensity of radiation decreases, its resistance increases, resulting in a change in the value current, thus changing the voltage drop across both ends of the photo resistor. Four optical resistors had used; each resistance was responsible for movement in a certain direction. When there was a difference in the intensity of illumination between the four optical resistors, it was heading in the direction of seeking that all optical resistors were in equal value. The resulting voltage through the optical resistance could be used by entering it into an electronic circuit (Arduino) to give commands in the form of electrical signals to the relays for the movement of the motor responsible for the movement of the solar collector.

3.4.3 Installing the LDR

The base for fixing the light resistance was made of a board of wood, in the form of a cross, this wooden base was fixed in the middle of the upper frame of the reflective surface, utilizing fixing screws. An electronic control circuit was used to ensure that the reflective surface of the solar collector was perpendicular to the sunlight that falls on it. This process was carried out using the Arduino system. The Arduino circuit receives the signal from the photoresistors and translates it into a signal outside it that controls the circuit of the four relays responsible for the movement of the motor in order to make the movement of the reflecting surface always perpendicular to the falling sunlight (solar tracking) as shown in Figure 3.9.
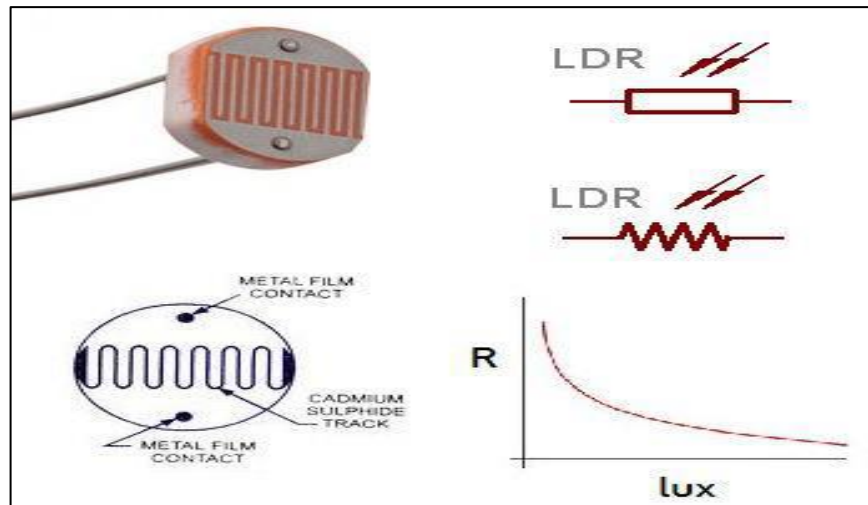
Figure 3.9: LDR composition.

3.4.4 Connect The Arduino to the Relay Circuit

In the solar tracking system, an Arduino Mega was used to connect all the power connections, the entry and exit connections of the Arduino is presented in (Appendix B.2). The operating voltage of the Arduino was 5 volts DC and was connected the input connections with the optical resistors. And the output

connections of the Arduino were connected to control the circuit of the four relays. Since the electric motors operate on a DC system with 12 volts at low speed and high torque, Therefore, a relatively high electric current is required. For this reason, four additional relays are used (12VDC and 10A per contact) to take control feed from the Arduino circuit relays. The high power provided to electric motors was employing a battery source (12 volts DC, 40 amperes current) passing through the relay relays. Relays were also used to reverse the rotation of the two motors when responding to the tracking system.

3.5 Heat Collecting Elements (HCE)

In this section, the parts that receive the reflected rays from the reflecting surface and which could be used to heat the fluid were introduced.

3.5.1 Copper Tube

Copper tube was used in the solar collector parabolic trough in the most important area of exchange and concentration of the reflected rays from the reflecting surface. The specification of copper tube is 23 mm outer diameter, 0.7 mm in thickness and 210 cm in length as presented in (Appendix B.2). The copper tube was installed horizontally to ensure that the center of the copper tube is at the center of the reflecting surface, to ensure the focus of all the rays reflected from the reflecting surface to the absorbent. The copper tube was painted black to increase the absorption of the reflected rays.

3.5.2 Heat Exchanger

The heat exchanger is an important part of experimental work, it is installed on the support body. The heat exchanger was used to dissipate heat from the working fluid leaving the test section and passing inside the heat exchanger

tubes. The presence of fins around the exchanger tubes and a fan that pushes the air were helped to dissipate the heat of the working fluid to be used again in the experiment (close system) as shown in Figure 3.10.

Figure 3.10: Heat exchanger.

3.6 Thermo-Physical Properties of Nanofluids

This section deals with the calculations of thermo-physical properties of nanofluids. The thermo-physical properties include density, heat capacity, effective dynamic viscosity, effective thermal conductivity and thermal expansion coefficient. The density of the TiO_2-water and CuO-water nanofluid is represented by [50]:

$$\rho_{nf} = (1 - \varphi)\rho_f + \varphi \, \rho_p \tag{3.1}$$

The specific heat of the TiO_2-water and CuO-water nanofluid is expressed by [50]:

$$C_{p,nf} = \frac{(1-\varphi)(\rho \, C_p)_f + \varphi(\rho \, C_p)_p}{\rho_n} \tag{3.2}$$

The dynamic viscosity of the TiO$_2$-water and CuO-water nanofluid provided by the equation as shown [50]:

$$\frac{\mu_{nf}}{\mu_f} = 1 + 2.5\,\varphi \tag{3.3}$$

The effective thermal of the TiO$_2$-water and CuO- water nanofluid conductivity is given as follows [50]:

$$\frac{k_{nf}}{k_f} = \frac{k_p + 2k_f + 2\varphi(k_f - k_p)}{k_p + 2k_f + \varphi(k_f - k_p)} \tag{3.4}$$

Finally, the thermophysical properties of nanoparticles and water at T=300K are presented in Table 3.1

Table 3-1 Thermophysical properties of nanoparticles and water [51].

Type of nanoparticles	Thermophysical properties		
	ρ (kg/m^3)	Cp (J/kg.k)	K (W/m.k)
Water	996.5	4181	0.613
TiO$_2$	4230	686.2	8.95
CuO	6500	533	17.65

3.7 Preparation of Nanofluid

To prepare the nanofluid with a volume concentration of 0.02, an average nanoparticle diameter of 30 nm and a purity of 99.99% for CuO and TiO$_2$. The mass of nanoparticles required, that was proportional to the specific volumetric concentration was calculated using the following equations [50].

$$\varphi\% = \frac{\left[\frac{w_p}{\rho_p}\right]}{\left[\frac{w_p}{\rho_p} + \frac{w_{bf}}{\rho_{bf}}\right]} \qquad (3.5)$$

$$w_p = \rho_p \left[\frac{\varphi}{1-\varphi}\right] \left[\frac{w_{bf}}{\rho_{bf}}\right] \qquad (3.6)$$

Then, the weight of the nanoparticles mass was measured using a high-precision digital scale as presented in (Appendix B.2)

 The nano-powder was mixed with the distilled water inside the measuring cylinder in the laboratories of the College of Science/ Department of Chemistry/ University of Anbar. The amount of distilled water was proportional to the weight of nanoparticles that were calculated in Table 3.2.

The graduated cylinder was placed inside a larger graduated cylinder. Small pieces of ice were placed to reduce the temperature rise of the nanofluid due to the mixing process. The mixing of nanoparticles with distilled water continued for 1 hour under an Ultra-Sonicator at frequency 60 kHz during a half-hour time as shown in Figure 3.11. The above process was repeated until the required volume 12 liters of the nanofluid. Then, the prepared stable solution was kept under ultrasonic vibration frequency again for better dispersal of the resulting nanofluid. The nanofluid was used in this experimental investigation after several days of preparation.

Table 3-2 Volume concentrations and weight of nanoparticles

Volume concentrations (Ø), %	W_{TIO2} (g)	W_{CuO} (g)
0.02	10.15	15.60

a) nanofluid CuO   b) nanofluid TiO$_2$

Figure 3.11: Ultrasonic device

3.8 Experimental Procedure

In this current research, a PTSC solar collector had studied for three cases and according to the type of used fluid:

1- Using water 2- Using (0.02 Nano-CuO-water) 3- Using (0.02 nano-TiO$_2$-water nanofluid).

The experiments were carried out in the Department of Mechanical Engineering Anbar University. After completing the installation of all parts of the system, the system was built with all its recommendations and install pressure and flow sensors and temperature sensors type k on the suction pipe (test section). The fluid flow pipes were connected to the fluid tank, pump, and the rest of the fluid system parts. The system was turned on half an hour before the set time for operation and to record the first reading. The fluid passed from the fluid tank to the test section by the pump, the fluid flow was controlled by the valves in the pipe joints between the pump, the test section and the reverse feed pipe. The fluid gains heat from a heated copper tube (test section) by focusing solar rays

on it from the reflective surface of the solar collector and the fluid comes out hot. Temperatures are calculated using temperature sensors mounted on the test tube at specific positions to measure inlet and outlet temperatures, tube surface temperature, and tank temperature and we can the uncertainty for all devices as shown in Appendix D.1

3.9 Artificial Neural Network (ANNS)

The theory and design of the artificial neural network have advanced significantly over the past years. The purpose of ANNS is to provide an algorithms solution for complex problems such as classification, clustering, data compression, pattern coupling, function approximation, prediction, control, and optimization applications.

3.9.1 Artificial Neural Network Model

Artificial neural network (ANN) is defined as a mathematical model represented by a structure has a function similar to the human brain. The function of ANN structure is summarizing in memorizing and learning various tasks and behaving accordingly. ANN has been successfully used in various applications including those in the digital human model world and predicting the performance of the system outputs, for more details are in (Appendix E.1) Whereas, ANN is better to other regression models since it is more capable of tackling real-world and complex situations. ANN is applied and used by researchers in a system of prediction issues when:

1. Initialization of the input/output data for the parameters (training data).

2. It is necessary to predict the system's behavior quickly.

3. The system is complex, and mathematical formulas are difficult to express. In general, ANN can predict any system reliably and quickly, no matter how complex [52].

In general, Artificial Intelligence (AI) is shaping and deeply changing modern society along with the way acknowledges reality. Moreover, the AI has the ability to predict things like weather or market trends. Nowadays many tasks and services are generally assigned to AI algorithms [53].

3.9.2 Steps to build ANN model

The process of building a neural network goes through several stages [54].

1- Preparation and collection Data: parameters must be chosen so that the problem is well represented; some operations must be performed on the data used, and focus on the relationship between the parameters. During the network building stage, the data is divided into three groups to measure the efficiency of the artificial neural network (training set, validation set and test set) [55].

2- Define the network architecture: choosing the network architecture is one of the most difficult problems in designing artificial neural networks. Choosing the number of layers and the appropriate number of neurons in each layer is another challenge. All these choices must be made before starting training. Therefore, choosing of the right network depends on trial and error .

3- Choose a learning algorithm: the learning algorithm that matches the neural network architecture can be selected for the purpose of network training. One of the most important training algorithms is the back propagation algorithm [56].

4- Determining the Initialization Weights and the Learning Rate: the values of the initial weights and bias and its values for the learning rate are chosen

before starting the training of the neural network. The learning rate is what determines the speed of updating the weights and reaching the final weights. The learning rate must be chosen appropriate, because if the learning rate is slow, the update weights is also slow, but if the rate of learning is slow Learning quickly may cause weights to fluctuate and lead to instability in the training process [55].

5- Network training: the training time depends on the architecture of the network, the number of layers, the number of processing units, initial values for weights, and the learning rate [56].

6- Testing: the neural network is tested after completing the network training process. The purpose of testing is to ensure the performance of the neural network and its ability to calculate the correct output. The test process depends on the final weights of the training phase and the sum of squares of errors.

7- Implementation: it is considered one of the most important steps in building a neural network model. It is defined as the ability of the neural network to adapt the purpose for which it was built is tested, for example: prediction, follow-up and continuous development to improve the performance of the network [57].

3.9.3 Learning process

The learning process neural network is carried out in the same way that a person acquires knowledge. A number of examples are given of the desired pattern of the network are presented and identified by adjusting the weights of the interconnections between the network units by forming an internal representation of the desired pattern and store it in its memory to be available for later use [57].

The steps of building the ANN model can be represented in the flow chart, as shown in Figure 3.12.
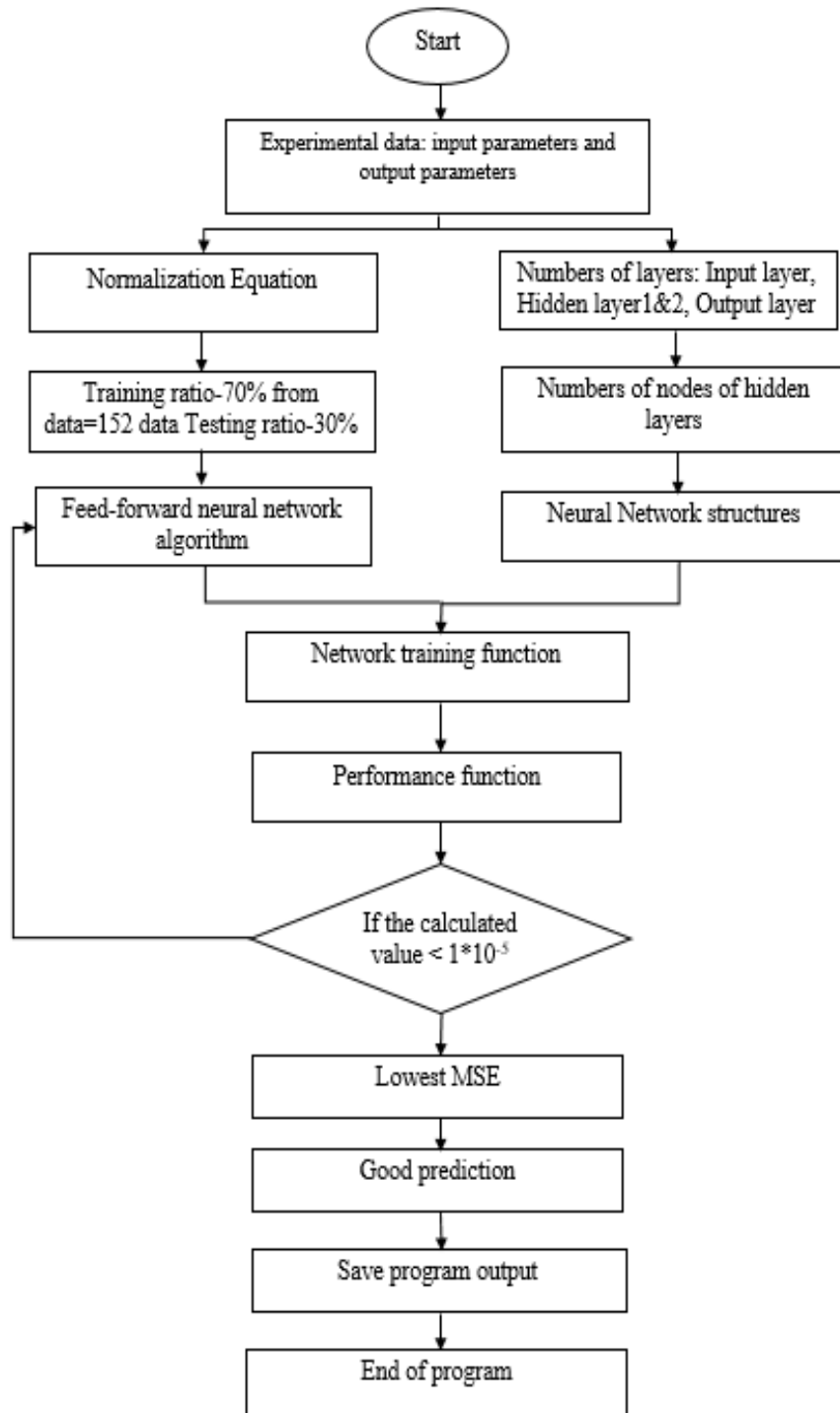
Figure 3.12: Flow chart of Artificial Neural Network program.

3.9.4 Neural Network Structure:

The ANN structure is made up of three layers an input layer, a hidden layer, and an output layer, as shown in Figure 3.13. The first hidden layer has I nodes, the second hidden layer has j nodes, and the output layer has one node. When applied to a single hidden layer, ANN is a 5-i-1, and when applied to two hidden layers, it is a 5-i-j-1. The number of nodes in the hidden layer is a function of the number of input nodes as shown in Equation 3.7 [58], and is denoted as:

$$i \; or \; j = \begin{cases} n/2 \\ n \\ 2*n \\ 2*n+1 \end{cases}$$
(3.7)

Where: n is the number of input nodes.
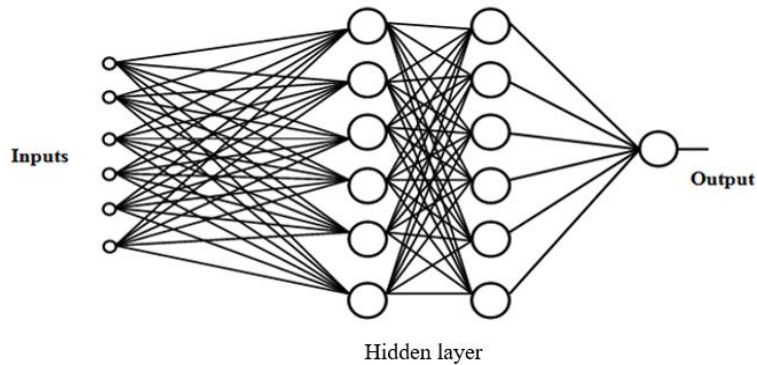
Figure 3.13: Network structures models [58].

3.9.5 Normalization

Before training the neural networks, the input vectors and the target vectors were normalized from 0 to 1 as the standard range. Equation 3.8 The input and output data were normalized using this method. [59].

$$x_i = \frac{0.8}{d_{max}-d_{min}}(d_i - d_{min}) + 0.1$$
(3.8)

CHAPTER FOUR

RESULTS AND DISCUSSION

CHAPTER FOUR

RESULTS AND DISCUSSION

4.1 Overview

This chapter showed the experimental results of this work ,which was done in Iraq / Ramadi city at the mechanical engineering department at the University of Anbar. Three different fluids were used as a working fluid (water, nanoparticles of CuO mixed with distilled water and nanoparticles of TiO_2 mixed with distilled water) with a closed-loop system. The results showed performance parameters of a parabolic collector as output temperature (T_o), useful heat gain (Q_u), and Thermal efficiency (η) of three different used fluids. The climate situation was taken from experimental calculations from (January 2021 to March 2021). The values of solar radiation were calculated by solar intensity power. These experiments were performed during sunny days. The volumetric flow rate ($\overset{o}{V}$) that were taken (30, 40, 60, and 80) L/hr and the measured and calculated data are presented in (Appendix B.3) Then, the neural network model was used to predict the experiment data and choose the best model for the structure of the neural network.

4.2 Effect of Volumetric Flow Rate

4.2.1 Solar Intensity

The intensity of solar radiation is measured using the solar radiation measurement system (solar cell, tracking system and Arduino). Solar radiation intensity readings are recorded every 30 minutes for sunny days: (16/1/2021, 17/1/2021, 19/1/2021, 20/1/2021) when using water. (5/2/2021, 6/2/2021, 8/2/2021, 9/2/2021) when using CuO-water nanofluid nanofluid. (2/3/2021, 3/3/2021, 4/3/2021, 5/3/2021) when using TiO_2-water nanofluid nanofluid. The

intensity of solar radiation was measured from 9:00 to 15:00. Figure 4.1 shows the behavior of solar radiation versus local time, where the solar radiation intensity increases gradually until it reaches its peak at midday 12:30 when using CuO-watre nanofluid due to the amount of solar radiation falling on the tube area and also clear sky at this time. Then the intensity of solar radiation begins to decrease gradually at the local time from 13:00 to 15:00.
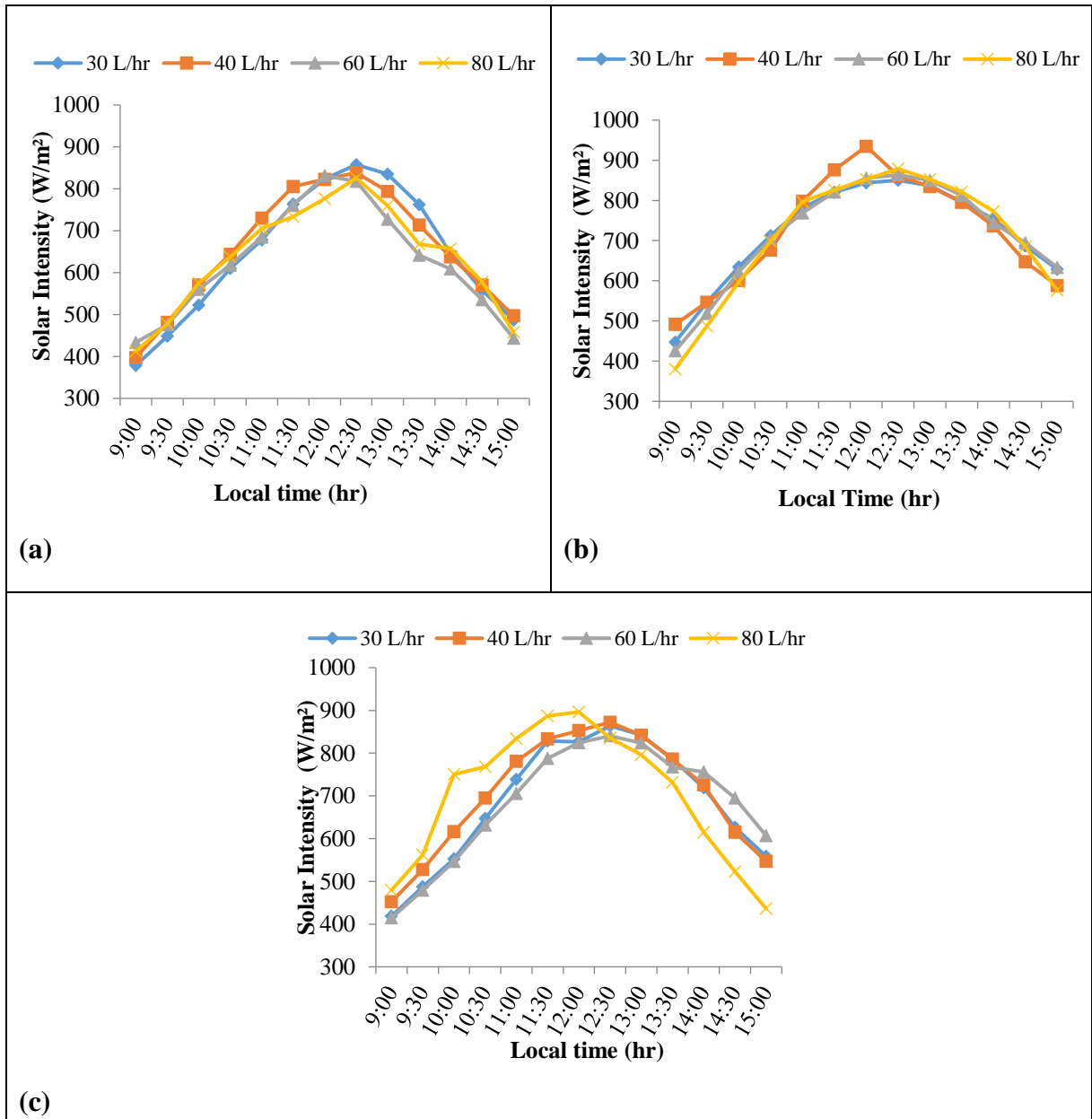
Figure 4.1: Variation of intensity solar radiation with a volumetric flow rate at (a) water (b) CuO-watre nanofluid, (c) TiO$_2$-watre nanofluid.

4.2.2 Inlet Temperature

The fluid inlet temperature, which was measured by a recorded temperature when the fluid entered the tube, gradually increases with the increase in the intensity of the solar radiation and the inlet temperature continues to increase as the fluid circulation system is closed. Figure 4.2 depicted that the behavior of inlet temperature with time for the three used fluids in this investigation.
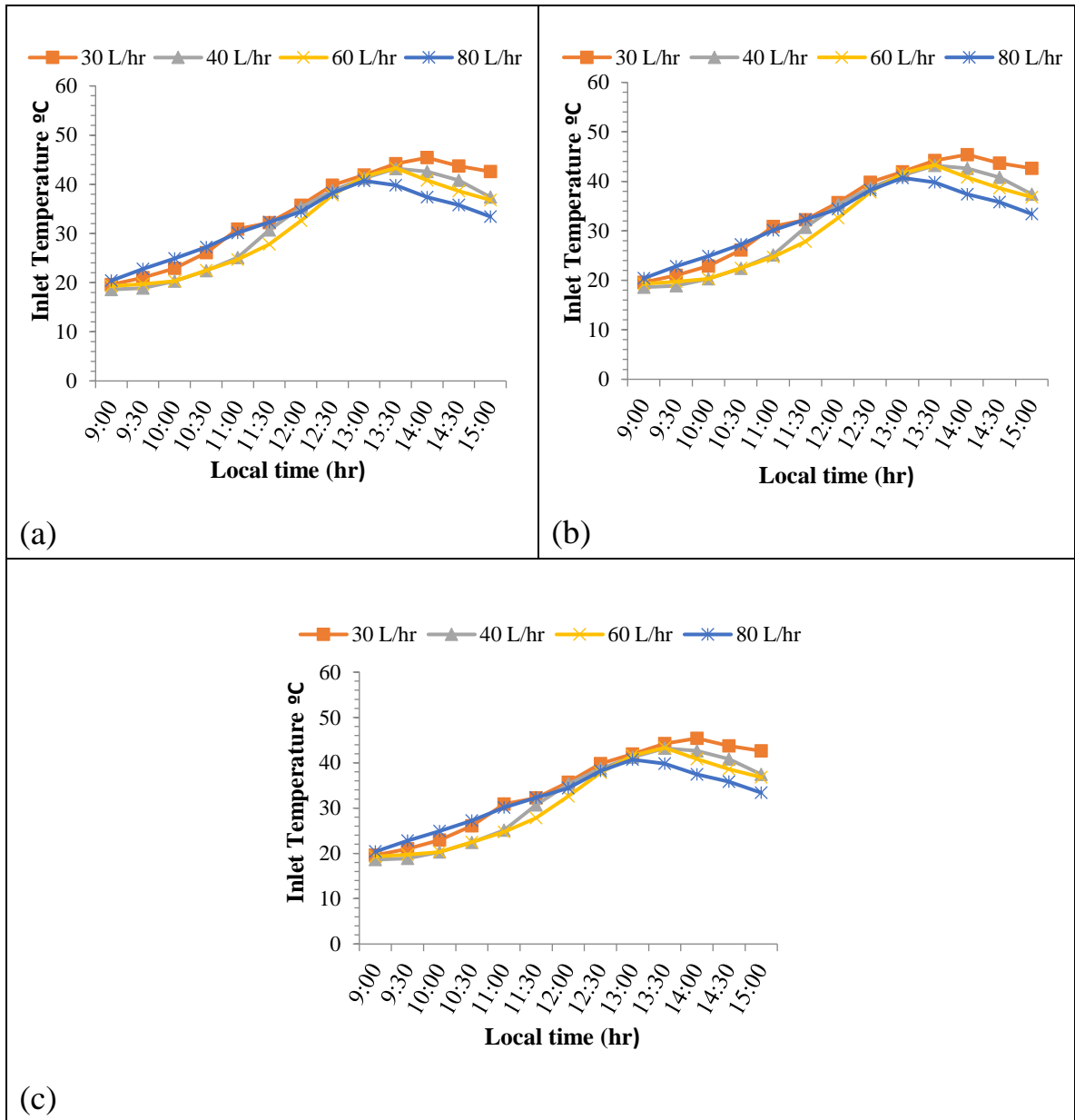
Figure 4.2: Variation of inlet Temperature with a mass flow rate of (a) water, b) CuO-watre nanofluid , (c) TiO$_2$-watre nanofluid.

4.2.3 Outlet Temperature

The outlet temperature of the fluid leaving the absorber tube is affected by the change in the fluid mass flow rate. The average outlet temperature was:

For water (40.8, 36.1, 30.7, 30.3) ºC at (30,40,60 and 80) L/hr mass flow rates respectively as shown in Figure 4.3.a. Notice that outlet temperature of mass flow rate (30 L/hr) is more than (40, 60,80) L/hr. for water CuO/ water respectively (49.8, 44.7, 41.3, 39.4) ºC at (30,40,60 and 80) L/hr mass flow rates respectively as shown in Figure 4.3.b. Notice that outlet temperature of mass flow rate (30 L/hr) is more than (40, 60,80) L/hr. for water TiO_2-water nanofluid (49.6, 42.6, 37.8, 36.9) ºC at (30,40,60 and 80) L/hr mass flow rates respectively as shown in Figure 4.3.c. Notice that outlet temperature of mass flow rate (30 L/hr) is more than (40, 60,80) L/hr.

It is observed that the fluid outlet temperature decreases with the increase in the mass flow because the high flow of fluid means the increase in the fluid velocity inside the absorber and it passes quickly and does not have enough time for heat exchange and this leads to a decrease in the outlet temperature when the flow increases.

(a)

(b)

46

(c)
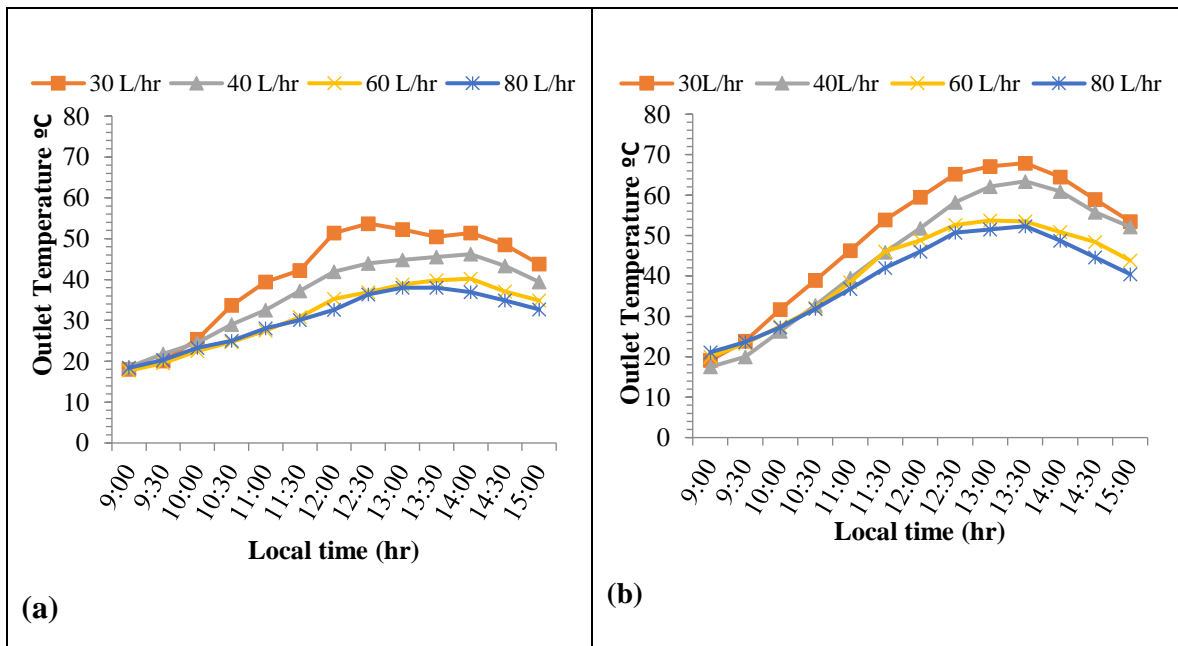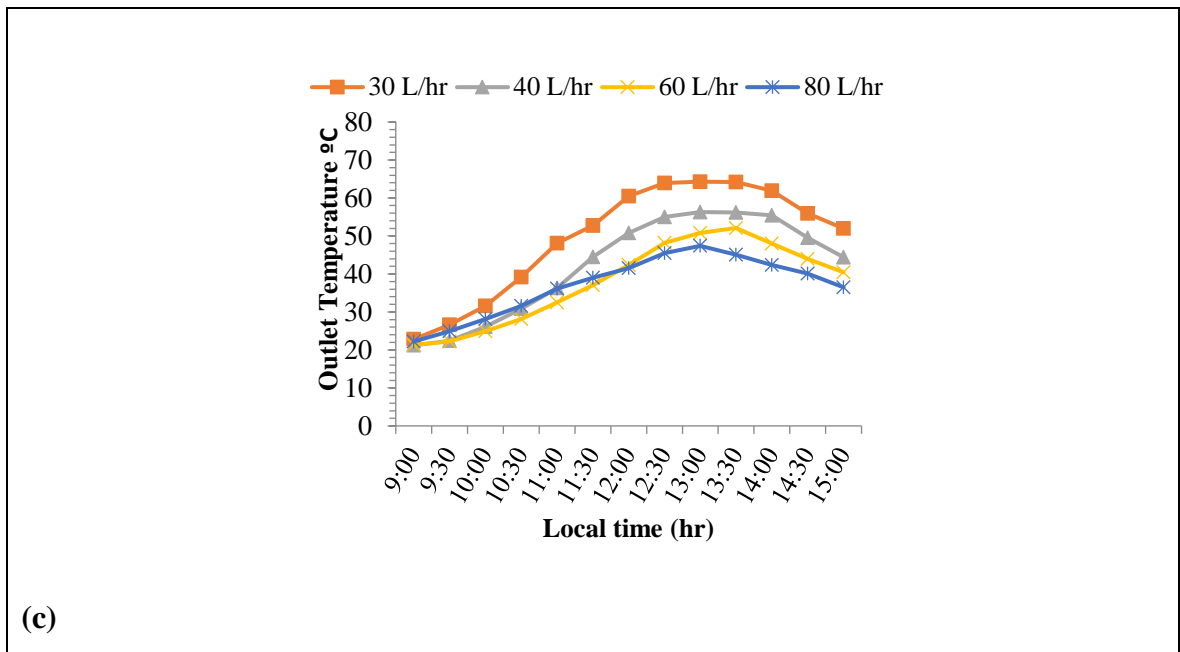
Figure 4.3: Variation of output temperature with time of (a) water, (b) CuO-water nanofluid., (c) TiO$_2$-water nanofluid.

4.2.4 Pressure Drop

Figure 4.4 shows the measured pressure drop (ΔP) for the three fluid flow rates (water, CuO water, TiO$_2$-water nanofluid) that were used in this experiment. It is observed that the pressure drop increases with the increase in the flow rate. Because the increase in the flow leads to an increase in the fluid velocity, which leads to an increase in the pressure drop and for all working fluids used.
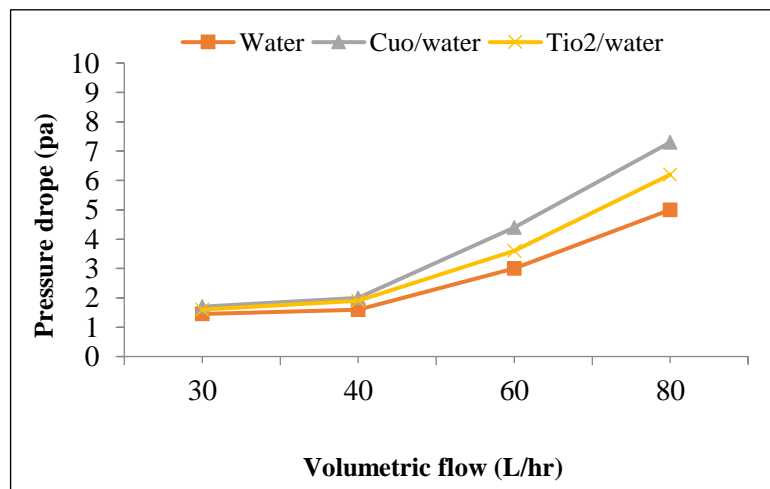
Figure 4.4: Pressure Drop versus Volumetric flow

4.2.5 Useful Heat Gain

Useful heat gain is one of the most significant solar collector parameters , collectors to determine performance. Figure 4.5 shows the Useful Heat gain during 9:00 to 15:00 for the three fluids used in this research. The average heat gain became**:**

for water (448.4, 440.3, 434, 388.9) watt at (30,40,60 and 80) L/hr mass flow rates respectively as shown in Figure 4.5.a. Notice that the useful heat gain of mass flow rate (30 L/hr) is more than (40, 60,80) L/hr by (4.9, 11.1, 15.3)% respectively.

For CuO-water nanofluid (594.5, 582.94, 572.8, 554.3) watt at flow rate 30,40,60 and 80 L/hr mass flow rates respectively as shown in Figure 4.5.b. Notice that the useful heat gain of mass flow rate (30 L/hr) is more than (40, 60,80) L/hr by (2.3, 6.2, 8.5)% respectively.

For TiO_2-water nanofluid (491.2, 479.2, 463.8, 452) watt at (30,40,60 and 80) L/hr mass flow rates respectively as shown in Figure 4.5.c. Notice that the useful heat gain of mass flow rate (30 L/hr) is more than (40, 60,80) L/hr by (2, 7.2, 11)% respectively.

Through these results, it has been observed that when the flow rate of the three fluids is increased and in all cases, the useful heat extracted from the absorber tube decreases with the increase in the flow for each fluid, because the useful heat depends in its effect on the difference in the temperature of the inlet and outlet of the fluid and the amount of mass flow and constant temperature quality. Since the flow is located within the laminar flow zone and the use of the solar tracking system, all these lead to the effect of the temperature difference (ΔT) being higher than the effect of the fluid flow on the useful heat. Therefore, the useful heat decreases with increasing fluid flow for all cases. The highest useful heat is obtained at a flow rate of 30L/hr.
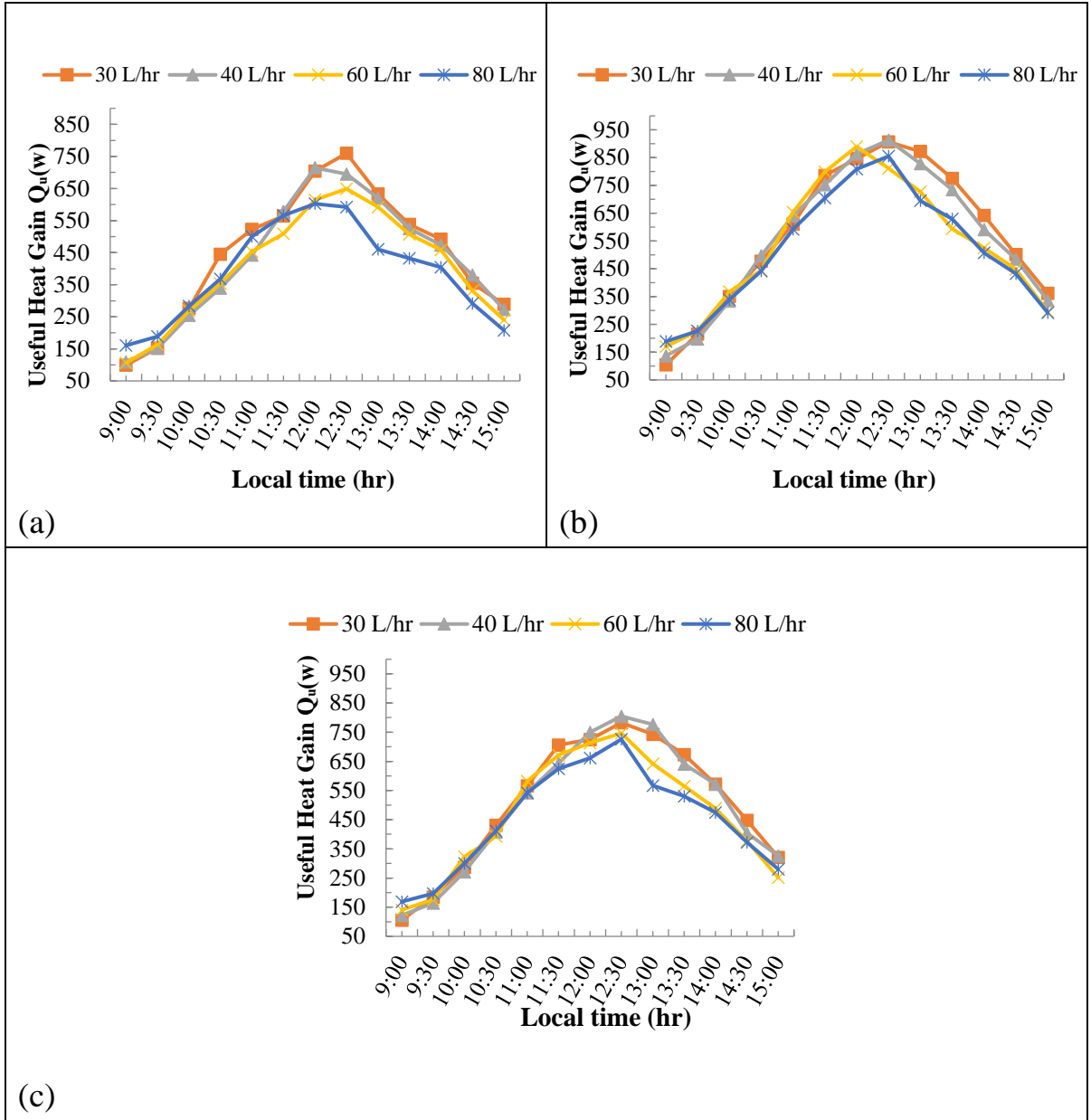
Figure 4.5: Variation of Useful heat gain with time of (a) water, (b) CuO-water nanofluid., (c) TiO$_2$-water nanofluid.

4.2.6 Efficiency

Thermal efficiency changes were changed with time 9:00 to 15:00 for the days during which the test was performed. Thermal efficiency was gradually increased with the increasing the useful heat gain until midday, after which the thermal efficiency began to decrease gradually. Efficiency was increased with time until the maximum efficiency became: For water (45.3, 44.4, 41.7, 39.7) % at (30,40,60 and 80) L/hr mass flow rates respectively as shown in Figure 4.6.a. Notice that the thermal efficiency of mass flow rate 30 L/hr is more than (40, 60,80) L/hr.

For CuO-water nanofluid (54.6, 54.1, 53.2, 49.8) % at (30,40,60 and 80) L/hr mass flow rates respectively as shown in Figure 4.6.b. Notice that the thermal efficiency of mass flow rate 30 L/hr is more than (40, 60,80) L/hr.

For TiO_2-water nanofluid (47.4, 46.4, 45.5, 44.4) % at (30,40,60 and 80) L/hr mass flow rates respectively as shown in Figure 4.6.c. Notice that the thermal efficiency of mass flow rate 30 L/hr is more than (40, 60,80) L/hr.

The average efficiency became: For water (33.7, 31.7, 31.5, 30.1)% at (30,40,60 and 80) L/hr mass flow rates respectively as shown in Figure 4.6.a. Notice that the thermal efficiency of mass flow rate 30 L/hr is more than (40, 60,80) L/hr by (6.2, 6.7, 11.8)% respectively.

For CuO-water nanofluid (38.7, 37.8, 36.4, 35.6) % at (30,40,60 and 80) L/hr mass flow rates respectively as shown in Figure 4.6.b. Notice that the thermal efficiency of mass flow rate 30 L/hr is more than (40, 60,80) L/hr by (2.3, 6.2, 8.5)% respectively.

For TiO$_2$-water nanofluid (35.6, 34.1, 33.4, 32.1) % at (30,40,60 and 80) L/hr mass flow rates respectively as shown in Figure 4.6.c.

 Notice that thermal efficiency of mass flow rate 30 L/hr is more than (40, 60,80) L/hr by (4.5, 6.8, 10.2)% respectively.

The effect of mass flow rate ranged (30 L/hr -80 L/hr) on the thermal efficiency with time for different working fluid. From figure 4.6, It has been observed that the thermal efficiency decreases with the increase in the mass flow rate because the thermal efficiency is affected by the mass flow rate and the temperature difference between the inlet and outlet of the fluid, since the mass flow of the fluid is within the laminar flow area and the presence of a solar radiation tracking system. Therefore, the effect of the temperature difference is greater than the effect of mass flow for that Thermal efficiency decreases with increasing mass flow.
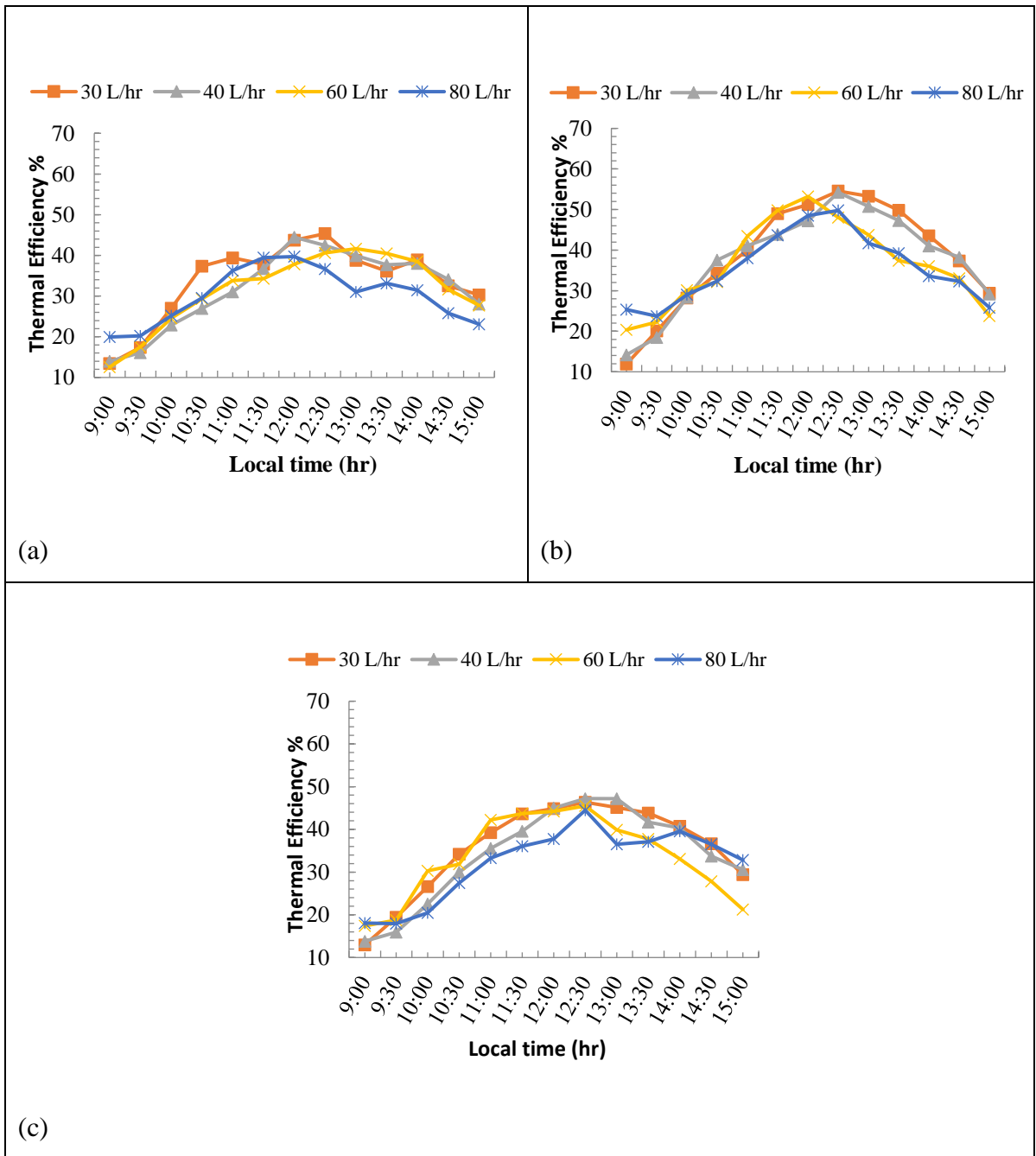
Figure 4.6 Variation of Efficiency with time of (a) water, (b) CuO-water nanofluid., (c) TiO$_2$-water nanofluid.

52

4.3 Effect of working fluid

4.3.1 Solar Intensity

The intensity of solar radiation is measured using the solar radiation measurement system (solar cell, tracking system and Arduino). Solar radiation intensity readings are recorded every 30 minutes for sunny days: (16/1/2021, 5/2/2021, 2/3/2021) when using water, CuO-water nanofluid and using TiO_2-water nanofluid respectively. The intensity of solar radiation was measured from 9:00 to 15:00. Where the intensity of radiation increases gradually until it reaches its peak at midday 12:30, and then the intensity of solar radiation decreases until 15:00. Figure 4.7 shows the behavior of solar radiation.
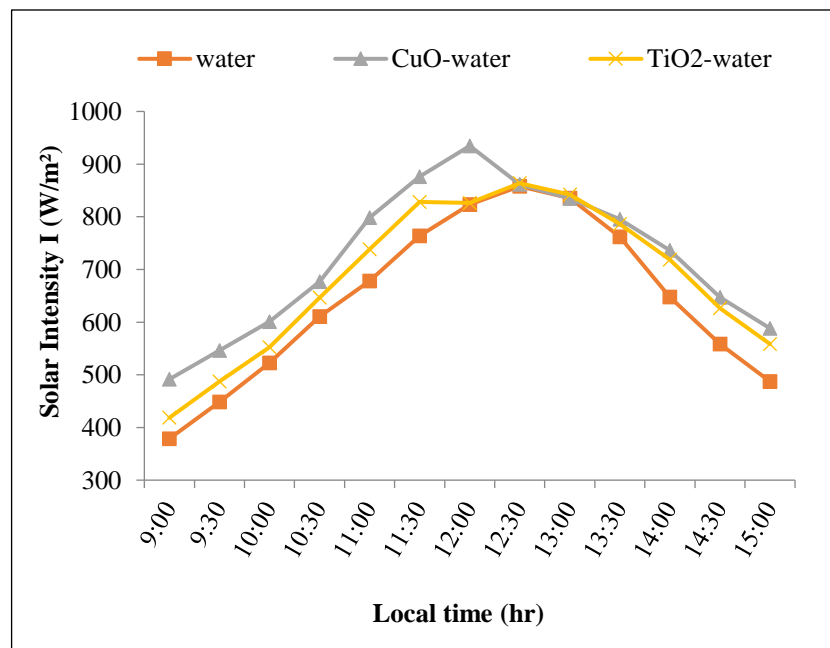
Figure 4.7: Variation of solar intensity with local time for different working fluid at $\overset{o}{V}$=30 L/hr.

4.3.2 Inlet Temperature

The fluid inlet temperature, which was measured by a digital temperature logger as the fluid entered the suction tube, every half hour. From Figure 4.8 it is noted that the fluid inlet temperature increases gradually with the increase in the intensity of solar radiation and that the use of a closed system for fluid circulation also led to an increase in the inlet temperature. The inlet temperature continues to increase gradually until it reaches its peak at midday, after which it begins to gradually decrease until 15:00. Figure 4.8 shows that the behavior of inlet temperature over time for the three fluids used in this research.
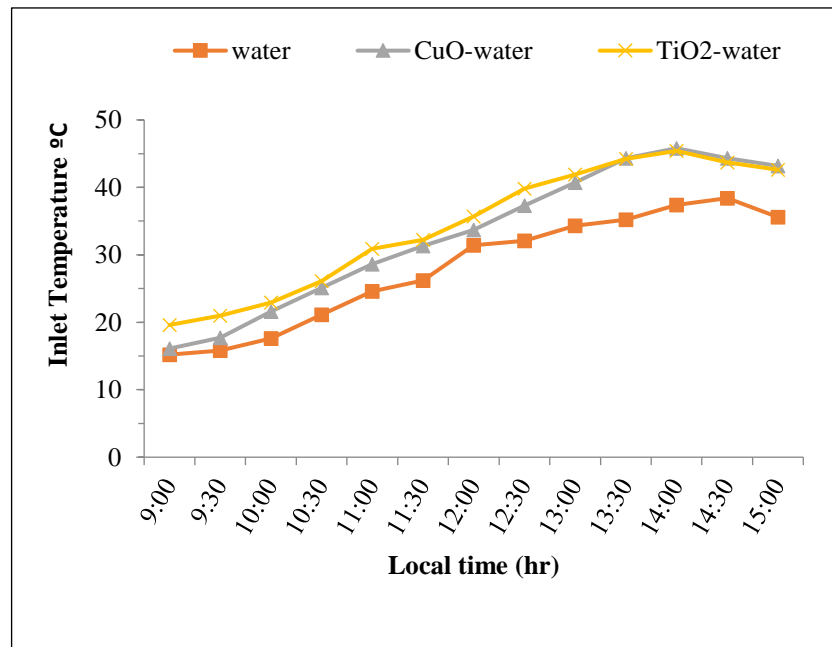
Figure 4.8: Variation of Inlet temperature with local time for different working fluid at $\overset{\circ}{V}$=30 L/hr.

4.3.3 Outlet Temperature

The outlet temperature of the three fluids used (water, CuO-water nanofluid and TiO$_2$-water nanofluid) in this experiment was measured using a digital temperature logger, from 9:00 to 15:00 at a volumetric flow rate of 30 L/hr

54

every half hour as shown in Figure 4.9. It is observe that the gradual increase in the output temperature of the working fluid is due to the increase in solar radiation and heat exchange between the hot absorber tube and the fluid passing through it. Therefore, the exit temperature of the fluid begins to rise from 9:00 and continues to rise with time until it reaches the maximum value at midday (53.7, 66.9, 64.8)°C for water, CuO-water nanofluid and TiO_2-water nanofluid respectively after which it begins to gradually decrease until 15:00.

The average outlet temperature was (40.8, 49.6, 47.8)°C for water, CuO-water nanofluid and TiO_2-water respectively for 30 L/hr mass flow rate as shown in Figure 4.9.It is noted that the outlet temperature of the nanofluids is higher than that of water, because the nanoparticles have a higher thermal conductivity, because the nanoparticles have a large surface area that they can contact with the surrounding materials.
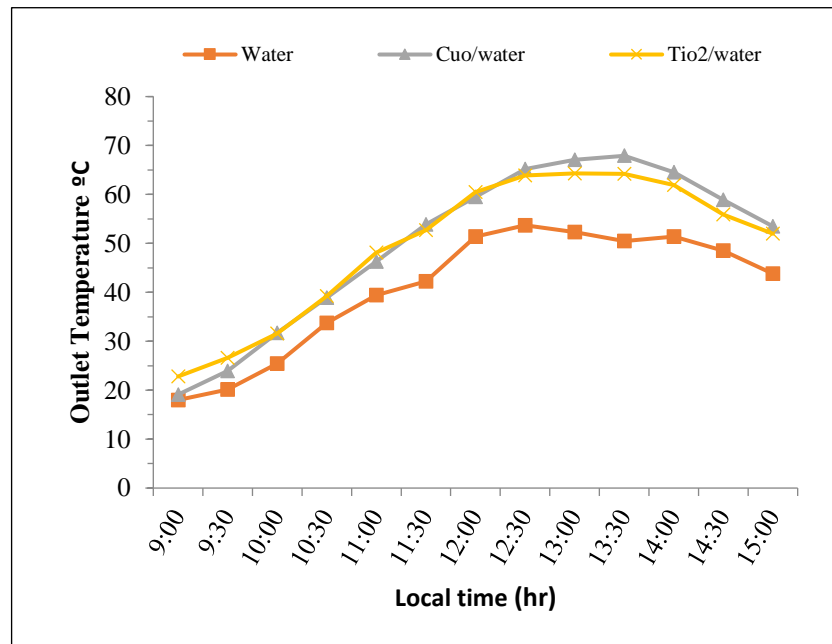
Figure 4.9: Variation of outlet temperature with local time for different working fluid at $\overset{\circ}{V}$=30 L/hr.

4.3.4 Pressure Drop

Figure 4.10 shows the measured pressure drop (ΔP) for the three fluid flows (water, CuO-water nanofluid, TiO$_2$-water nanofluid) that had been used in this experiment. Where the CuO nanofluid pressure drop appears larger than that of TiO$_2$ and greater than that of water. The real reason for this pressure drop increase is that when nanoparticles are added to water leads to an increase in the viscosity of the nanofluid, and this leads to an increase in pressure drop.
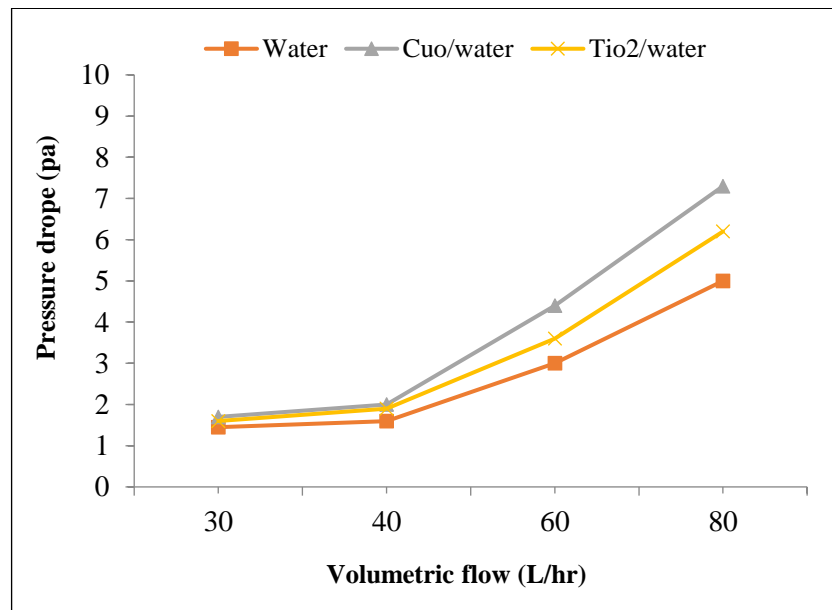
Figure 4.10: Pressure Drop versus Volumetric flow.

4.3.5 Useful Heat Gain

Figure (4.11) shows the behavior of the useful heat gain with the three working fluids used at the best flow rate of 30 L/hr. The useful heat gain begins to increase with the time and for all fluids used, from 9:00 the increase continues to reach the highest value at midday (759.7, 971.5,789) watt for water, CuO-water nanofluid and TiO$_2$-water nanofluid respectively for the mass flow rate of 30 L/hr. Due to an increase in the intensity of the solar radiation, which leads

to an increase in the temperature of the absorber tube and from it to an increase in the exit temperature of the fluid, which results in an increase in the difference in the temperature of the inlet and outlet of the fluid, which results in an increase in the useful heat gain until midday. After that, the intensity of the solar radiation begins to decrease gradually until 15:00 Which also leads to a gradual decrease in the useful heat gain for the fluids used. It is noted that The average heat gain for the working fluids used is at 30 L/hr the best flow rate of (759.7, 971.5,789) watt for water, CuO-water nanofluid and TiO$_2$-water nanofluid respectively.

The heat gain rate of CuO-water nanofluid is greater than TiO$_2$-water nanofluid and greater than that of water, because CuO-water nanofluid has a thermal conductivity greater than TiO$_2$-water nanofluid and the latter has a greater thermal conductivity than water.
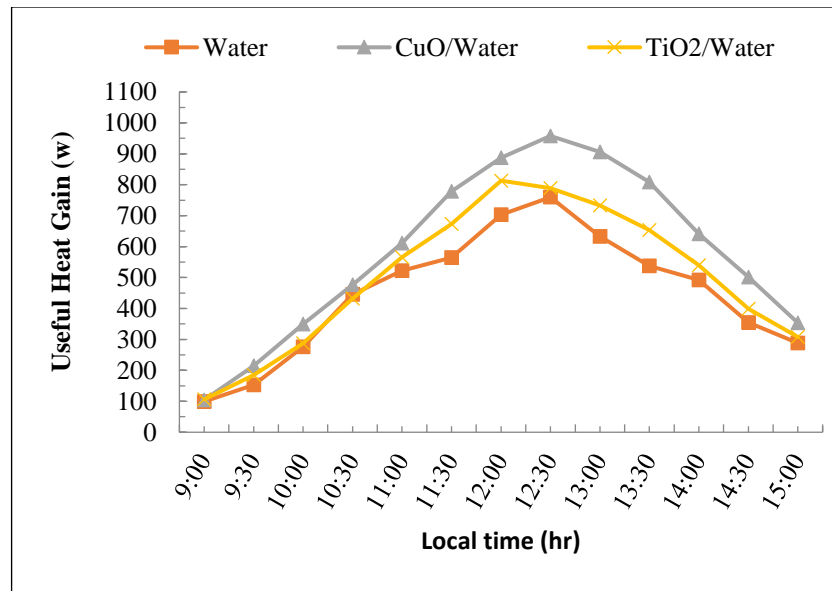
Figure 4.11: Variation of useful heat gain versus local time for different working fluid at $\overset{\circ}{V}$=30 L/hr.

4.3.6 Efficiency

Thermal efficiency changes with time from 9:00 to 15:00 for the best flow rate during which the test was performed. Thermal efficiency increases as the useful heat gain increases until the maximum efficiency becomes: (50.,57.5 , 51.4) % for water, CuO-water nanofluid and TiO$_2$-water nanofluid respectively for the mass flow rate of 30 L/hr as shown in Figure 4.12. Note that the average thermal efficiency for the best working fluid flow rate is (40.8,49.8 , 49.6) ℃ for water,CuO -water nanofluid and TiO$_2$- water respectively for 30 L/hr mass flow rate. where the thermal efficiency rate for CuO-water nanofluid is greater than TiO$_2$-water nanofluid and both are larger than water. Because CuO-water nanofluid has the highest thermal conductivity, which results in the highest output temperature and the highest useful heat gain compared to TiO$_2$-water nanofluid and both are larger than water.
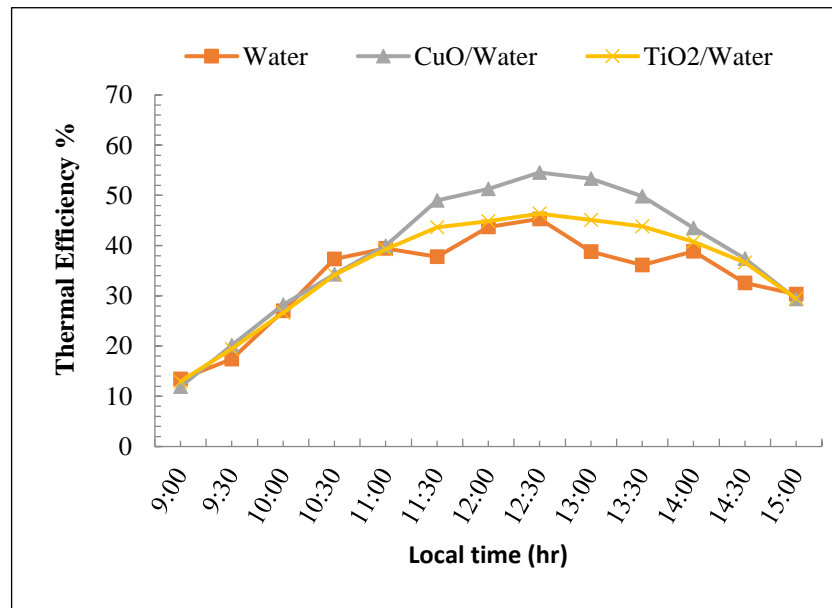
Figure 4.12: Variation of thermal efficiency with local time for different working fluid at $\overset{\circ}{V}$=30 L/hr.

4.4 Designing ANN Models

Several systemic approaches are used to create ANN models. There are five fundamental steps to follow in general: (1) data collection, (2) data preprocessing, (3) network building, (4) training, and (5) testing and validation performance of the model.

4.4.1 Comparing Data

The comparison between the experimental data and the structure of the trained neural networks (ANN) (4-2-2-1) shows that the average percentage of thermal efficiency difference between the experiment and ANN (4-2-2-1) is 14.4% with R = 0.99965for training and R = 0.99183 for the test as in the Figure 4.13.
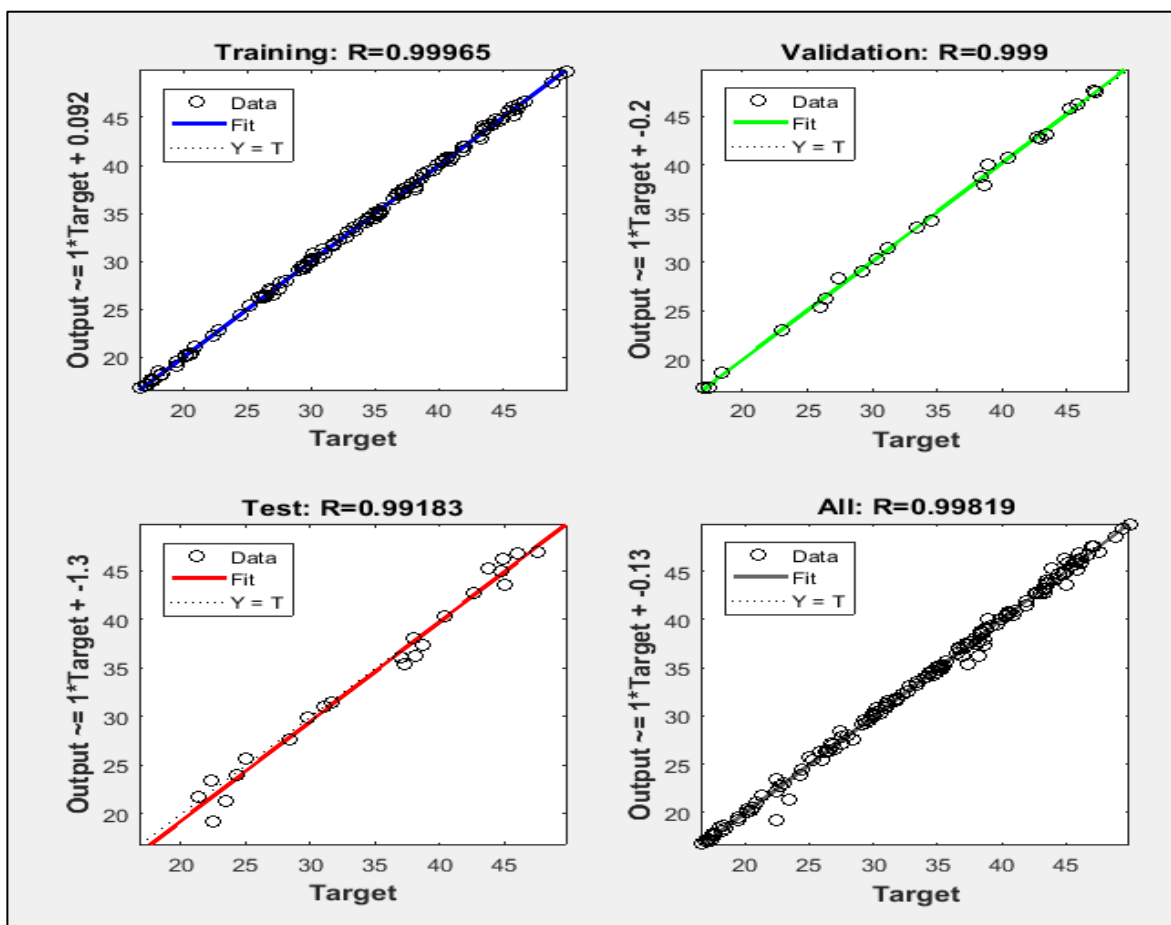
Figure 4.13: Neural Network Training Regression, Epoch 68, Validation stops for structure (4-2-2-1).

The comparison between the experimental data and the structure of the neural networks (ANN) on which the training is conducted (4-9-9-1) the average percentage of thermal efficiency difference between the experiment and ANN is 9.45% with R = 0.9997 for training and R = 0.99998 for testing as in the Figure 4.14.
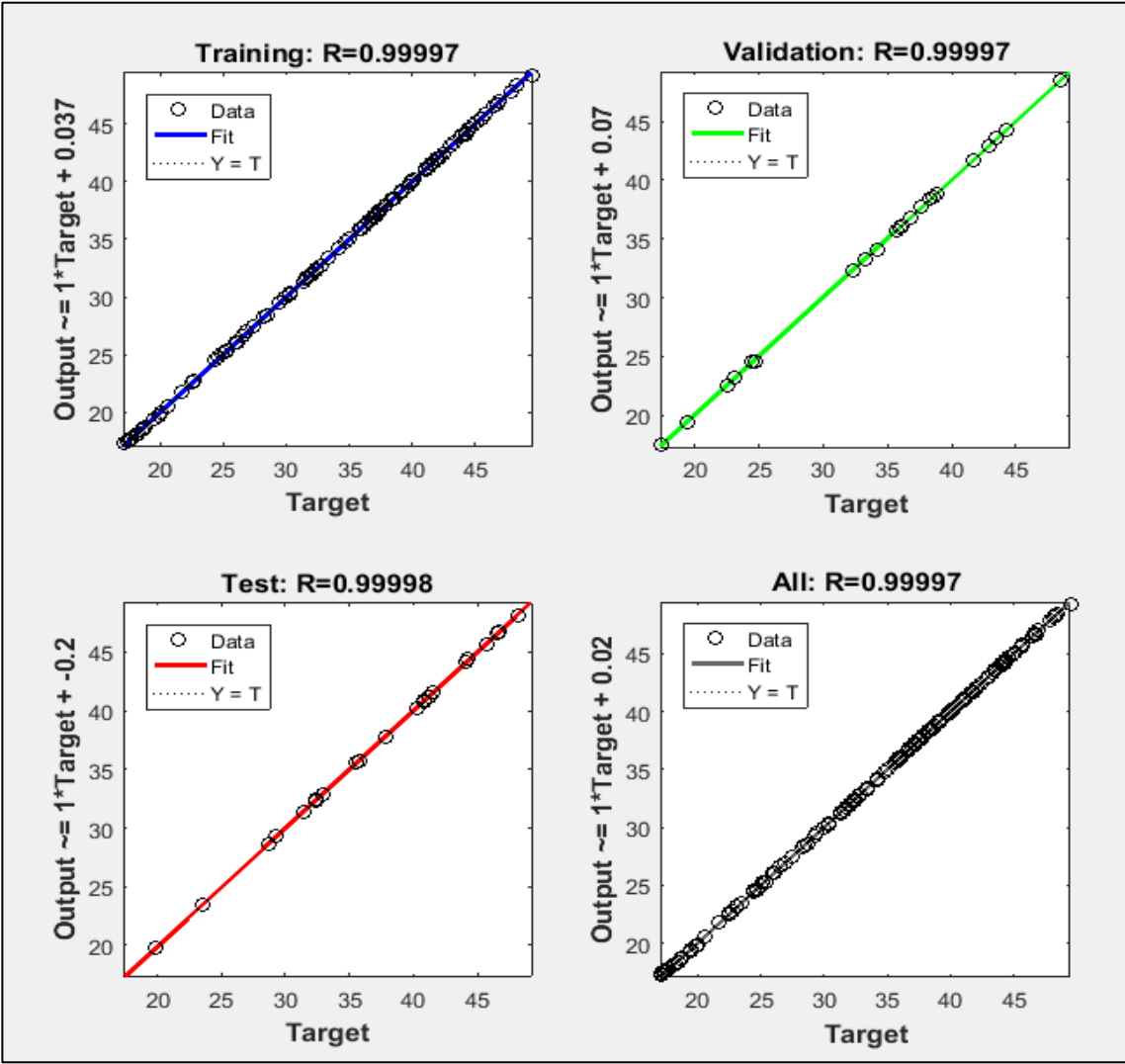
Figure 4.14: Neural Network Training Regression, Epoch 178, Validation stops for structure (4-9-9-1).

4.4.2 Predicting The Results Data

The structure of the neural network 4-2-2-1 and 4-9-9-1, after conducting the training and examination of the experiment data in MATLAB and choosing the command Regression, a chart appears showing the training and examination values of the experiment data thermal efficiency.

Table 4-1: Values of ANN structures of training, validation, testing phases and the all data.

Set	4-2-2-1				4-9-9-1			
	Training	Validation	Testing	all data	Training	Validation	Testing	all data
RMSE	5.292	2.167	5.278	4.403	5.533	3.398	3.951	4.603
R^2	0.984	0.996	0.978	0.984	0.975	0.991	0.987	0.983
MSE	28.007	4.696	27.857	19.390	30.610	11.547	15.613	21.191

The process of training the network ends when the minimum mean square error or the maximum of the epoch (1000). From Appendix E ,Table E.3, Table 4.1and Figure 4.15 represents the graph of the actual and expected thermal efficiency values for the two neural network models that are used in this experiment. It is noted that the models (4-2-2-1) and (4-9-9-1) have similar behavior to the experimental line.
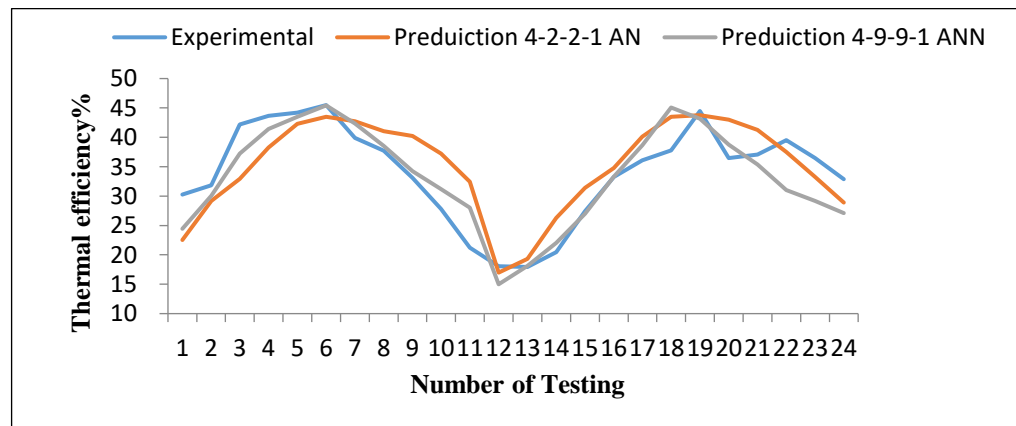
Figure 4.15: Investigation of the similarity of the line pattern between the experimental phase and the ANN of the test phase.

CHAPTER FIVE

CONCLUSIONS AND RECOMMENDATIONS FOR FUTURE WORK

CHAPTER FIVE

CONCLUSIONS AND RECOMMENDATIONS FOR FUTURE WORK

5.1 Conclusions

PTSC may be very effective and useful in heating water applications if the cost of the system is reduced to a certain limit.

The goal of the presented thesis is to implement an experimental work to study the thermal performance of a PTSC system. Three working fluids were used; water, CuO-water nanofiuid, and TiO_2-water nanofiuid. Also, a comparison of the thermal performance of a modified PTSC system with the conventional one is done. ANN is utilized to predict the thermal efficiency of the PTSC system. The experimental work has be conducted at four different mass flow rates of (30, 40,60, 80) L/hr. The experimental work has been carried out in the mechanical engineering department/ University of Anbar/ Al-Anbar city from January 2021 to March 2021. The work has been done from 09.00 to 15.00 daily for a whole length of the work span.

According to the data that had been obtained experimentally, ANN of the collector was created considering four inputs and one outputs. The input parameters included an inlet temperature of the fluid, the outlet temperature of the fluid, temperature of the receiver tube and solar intensity. The output parameters included thermal efficiency.

The useful heat gains, thermal efficiency, pressure drop, and coefficient of friction, were calculated in each case of the receiver tubes and mass flow rate. From the experimental results, the following could be concluded:

1- The nanofluids have a thermal performance higher than the conventional working fluid. In general, the thermal efficiency of the collector using the TiO_2 was higher than the smooth absorber tube by approximately 7.12%. Also, the experimental thermal efficiency of the collector using the CuO was higher than the smooth absorber tube by approximately 19.2%.

2- The Thermal efficiency of the experimental and the ANN results are compared. The results realize that there is a clear agreement between the crisp outputs that had been obtained for both methods. The results revile that the agreement in the thermal efficiency between the ANN analysis and the experimental results about 91% for 4-9-9-1, and 86% for 4-2-21.

5.2 Suggestions for Future Work

There are some suggestions to improve the present work:

1- Different types of nanoparticles such as AL_2O_3, ZnO, SiO_2 etc with different diameter and different volume fraction dispersed in water may be prepared and examined over the wide range of volumetric flow rate.

2- The experimental work may be extended to study the effect of wind speed, solar radiation tracking angle

3- Numerical study may be achieved to more different design parameters.

REFERENCES

REFERENCES

[1] Jemaa, A. B., Rafa, S., Essounbouli, N., Hamzaoui, A., Hnaien, F., and Yalaoui, F. 2013. Estimation of global solar radiation using three simple methods. Energy Procedia, 42, 406-415.

[2] Bhargva, M., and Agrawal, V. P. 2012. Modeling Analysis Evaluation Selection and Experimental Investigation of Parabolic Trough Solar Collector System (Doctoral dissertation).

[3] Nshimyumuremyi, E., and Junqi, W. 2019. Thermal efficiency and cost analysis of solar water heater made in Rwanda. Energy Exploration and Exploitation, 37(3), 1147-1161.

[4] Ghritlahre, H. K., and Prasad, R. K. 2018. Application of ANN technique to predict the performance of solar collector systems-A review. Renewable and Sustainable Energy Reviews, 84, 75-88.

[5] Kalogirou, S. 2007. Recent patents in solar energy collectors and applications. Recent Patents on Engineering, 1(1), 23-33.

[6] Alarcón Villamil, A., Hortúa, J. E., and López, A. 2013. Comparison of thermal solar collector technologies and their applications. Tecciencia, 8(15), 27-35.

[7] Günther, M., Eickhoff, M., Khalil, T., and Meyer-Grünefeldt, M. 2006. Linear fresnel technology. i Advanced CSP Teaching Materials, Enermena.

[8] Demagh, Y., Hachicha, A. A., Benmoussa, H., and Kabar, Y. 2018. Numerical investigation of a novel sinusoidal tube receiver for parabolic trough technology. Applied Energy, 218, 494-510.

[9] Bellos, E., and Tzivanidis, C. 2018. Investigation of a star flow insert in a parabolic trough solar collector. Applied Energy, 224, 86-102.

[10] Ebrahimi-Moghadam, A., Mohseni-Gharyehsafa, B., and Farzaneh-Gord, M. 2018. Using artificial neural network and quadratic algorithm for minimizing entropy generation of Al2O3-EG/W nanofluid flow inside parabolic trough solar collector. Renewable energy, 129, 473-485.

[11] Tiwari, G. N. 2002. Solar energy: fundamentals, design, modelling and applications. Alpha Science Int'l Ltd.

[12] Bhargva, M., and Agrawal, V. P. 2012. Modeling Analysis Evaluation Selection and Experimental Investigation of Parabolic Trough Solar Collector System (Doctoral dissertation).

[13] Hamidi, S. T., Mohammed, J. A. K., and Reda, L. M. (2018). Design and Implementation of an Automatic Control for Two Axis Tracking System for Applications of Concentrated Solar Thermal Power. Al-Khwarizmi Engineering Journal, 14(4), 54-63.

[14] Abed, N., and Afgan, I. 2020. An extensive review of various technologies for enhancing the thermal and optical performances of parabolic trough collectors. International Journal of Energy Research, 44(7), 5117-5164.

[15] Bellos, E., and Tzivanidis, C. 2018. Investigation of a star flow insert in a parabolic trough solar collector. Applied Energy, 224, 86-102.

[16] Bhakta, A. K., Panday, N. K., and Singh, S. N. 2018. Performance study of a cylindrical parabolic concentrating solar water heater with nail type twisted tape inserts in the copper absorber tube. Energies, 11(1), 204.

[17] Jaramillo, O. A., Borunda, M., Velazquez-Lucho, K. M., and Robles, M. 2016. Parabolic trough solar collector for low enthalpy processes: An analysis of the efficiency enhancement by using twisted tape inserts. Renewable Energy, 93, 125-141.

[18] Salman, S. D., Kadhum, A. A. H., Takriff, M. S., and Mohamad, A. B. 2014. Heat transfer enhancement of laminar nanofluids flow in a circular tube fitted with parabolic-cut twisted tape inserts. The Scientific World Journal, 2014.

[19] Mwesigye, A., Bello-Ochende, T., and Meyer, J. P. 2016. Heat transfer and entropy generation in a parabolic trough receiver with wall-detached twisted tape inserts. International Journal of Thermal Sciences, 99, 238-257.

[20] Muhammad, N. M. A., and Sidik, N. A. C. 2018. Utilisation of nanofluids in minichannel for heat transfer and fluid flow augmentation. J. Adv. Res. Design, 51(1), 18-45.

[21] Mutuku, W. N. 2016. Ethylene glycol (EG)-based nanofluids as a coolant for automotive radiator. Asia Pacific Journal on Computational Engineering, 3(1), 1-15.

[22] Ali, A. R. I., and Salam, B. 2020. A review on nanofluid: Preparation, stability, thermophysical properties, heat transfer characteristics and application. SN Applied Sciences, 2(10), 1-17.

[23] Ji, J., Lu, W., Si, C., Zhang, S., Yao, X., Wang, W., and Chu, D. 2020. Overview on the Preparation and Heat Transfer Enhancement of Nanofluids. In Journal of Physics: Conference Series (Vol. 1637, No. 1, p. 012003). IOP Publishing.

[24] Dawood, H. K., Mohammed, H. A., Sidik, N. A. C., Munisamy, K. M., and Wahid, M. A. 2015. Forced, natural and mixed-convection heat transfer and fluid flow in annulus: A review. International Communications in Heat and Mass Transfer, 62, 45-57.

[25] Al-Zahrani, K. 2013 . The application of parabolic trough technology under yanbu climatein saudi arabia. World applied sciences journal, 23(10), 1386-1391.

[26] Yaici, W., and Entchev, E. 2014 . Prediction of the performance of a solar thermal energy system using adaptive neuro-fuzzy inference system. In 2014 International Conference on Renewable Energy Research and Application (ICRERA) (pp. 601-604). IEEE.

[27] Kajavali, A., Sivaraman, B., and Kulasekharan, N. 2015 . Investigation of heat transfer enhancement in a parabolic trough collector with a modified absorber. International Energy Journal, 14(4).

[28] Macedo-Valencia, J., Ramírez-Ávila, J., Acosta, R., Jaramillo, O. A., and Aguilar, J. O. 2014. Design, construction and evaluation of parabolic trough collector as demonstrative prototype. Energy procedia, 57, 989-998.

[29] Kumaresan, G., Sudhakar, P., Santosh, R., and Velraj, R. 2017. Experimental and numerical studies of thermal performance enhancement in the receiver part of solar parabolic trough collectors. Renewable and Sustainable Energy Reviews, 77, 1363-1374.

[30] Jamal-Abad, M. T., Saedodin, S., and Aminy, M. 2017. Experimental investigation on a solar parabolic trough collector for absorber tube filled with porous media. Renewable Energy, 107, 156-163.

[31] Ullah, F., and Kang, M. 2019. Performance evaluation of parabolic trough solar collector with solar tracking tilt sensor for water distillation. Energy and Environment, 30(7), 1219-1235.

[32] Debnath, S., Reddy, J., Das, B., and Jagadish. 2019. Modeling and optimization of flat plate solar air collectors: an integrated fuzzy method. Journal of Renewable and Sustainable Energy, 11(4), 043706.

[33] Tersoo, A. L., and Olufemi, A. C. Thermal Efficiency Evaluation of a Solar Thermal Steam Generating System Using Thermosiphon Technique with Parabolic Trough Collector.

[34] Ghritlahre, H. K., Chandrakar, P., and Ahmad, A. 2020. Application of ANN model to predict the performance of solar air heater using relevant input parameters. Sustainable Energy Technologies and Assessments, 40, 100764.

[35] Ghritlahre, H. K., Chandrakar, P., and Ahmad, A. 2020. Application of ANN model to predict the performance of solar air heater using relevant input parameters. Sustainable Energy Technologies and Assessments, 40, 100764.

[36] Mwesigye, A., Huan, Z., and Meyer, J. P. 2016. Thermal performance and entropy generation analysis of a high concentration ratio parabolic trough solar collector with Cu-Therminol® VP-1 nanofluid. Energy conversion and management, 120, 449-465.

[37] Menbari, A., Alemrajabi, A. A., and Rezaei, A. 2016. Heat transfer analysis and the effect of CuO/Water nanofluid on direct absorption concentrating solar collector. Applied Thermal Engineering, 104, 176-183.

[38] Subramani, J., Nagarajan, P. K., Wongwises, S., El-Agouz, S. A., and Sathyamurthy, R. 2018. Experimental study on the thermal performance and heat transfer characteristics of solar parabolic trough collector using Al2O3 nanofluids. Environmental Progress and Sustainable Energy, 37(3), 1149-1159.

[39] Mwesigye, A., and Meyer, J. P. 2017. Optimal thermal and thermodynamic performance of a solar parabolic trough receiver with different nanofluids and at different concentration ratios. Applied Energy, 193, 393-413.

[40] Bellos, E., and Tzivanidis, C. 2018. Thermal analysis of parabolic trough collector operating with mono and hybrid nanofluids. Sustainable Energy Technologies and Assessments, 26, 105-115.

[41] Bellos, E., and Tzivanidis, C. 2019. Thermal efficiency enhancement of nanofluid-based parabolic trough collectors. Journal of Thermal Analysis and Calorimetry, 135(1), 597-608.

[42] Subramani, J., Nagarajan, P. K., Mahian, O., and Sathyamurthy, R. 2018. Efficiency and heat transfer improvements in a parabolic trough solar collector using TiO_2 nanofluids under turbulent flow regime. Renewable energy, 119, 19-31.

[43] Bellos, E., Tzivanidis, C., and Tsimpoukis, D. 2018. Thermal, hydraulic and exergetic evaluation of a parabolic trough collector operating with thermal oil and molten salt based nanofluids. Energy Conversion and Management, 156, 388-402.

[44] De los Rios, M. S. B., Rivera-Solorio, C. I., and García-Cuéllar, A. J. 2018. Thermal performance of a parabolic trough linear collector using Al2O3/H2O nanofluids. Renewable Energy, 122, 665-673.

[45] Sadeghzadeh, M., Ahmadi, M. H., Kahani, M., Sakhaeinia, H., Chaji, H., and Chen, L. 2019. Smart modeling by using artificial intelligent techniques on thermal performance of flat-plate solar collector using nanofluid. Energy Science and Engineering, 7(5), 1649-1658.

[46] Delfani, S., Esmaeili, M., and Karami, M. 2019. Application of artificial neural network for performance prediction of a nanofluid-based direct

absorption solar collector. Sustainable Energy Technologies and Assessments, 36, 100559.

[47] Okonkwo, E. C., Adun, H., Babatunde, A. A., Abid, M., and Ratlamwala, T. A. 2019. Entropy Generation Minimization in a Parabolic Trough Collector Operating With SiO2–Water Nanofluids Using the Genetic Algorithm and Artificial Neural Network. Journal of Thermal Science and Engineering Applications, 12(3), 031007.

[48] Komeilibirjandi, A., Raffiee, A. H., Maleki, A., Nazari, M. A., and Shadloo, M. S. 2020. Thermal conductivity prediction of nanofluids containing CuO nanoparticles by using correlation and artificial neural network. Journal of Thermal Analysis and Calorimetry, 139(4), 2679-2689.

[49] Sadeghi, G., Nazari, S., Ameri, M., and Shama, F. 2020. Energy and exergy evaluation of the evacuated tube solar collector using Cu2O/water nanofluid utilizing ANN methods. Sustainable Energy Technologies and Assessments, 37, 100578.

[50] Ahmad, S., Abdullah, S., and Sopian, K. 2020. A review on the thermal performance of nanofluid inside circular tube with twisted tape inserts. Advances in Mechanical Engineering, 12(6), 1687814020924893.

[51] Mohammed, H. A., Al-Shamani, A. N., and Sheriff, J. M. 2012. Thermal and hydraulic characteristics of turbulent nanofluids flow in a rib–groove channel. International Communications in Heat and Mass Transfer, 39(10), 1584-1594.

[52] Bataineh, M. H. 2012. Artificial neural network for studying human performance. The University of Iowa.

[53] Caramazza, P. 2019. Artificial neural networks for scattered light imaging (Doctoral dissertation, University of Glasgow).

[54] Hagan, M. T., and Menhaj, M. B. 1994. Training feedforward networks with the Marquardt algorithm. IEEE transactions on Neural Networks, 5(6), 989-993.

[55] Dertat, A. 2018. Applied deep learning-part 1: Artificial neural networks, 2017. URl: https://towardsdatascience. com/applied-deep-learningpart-1-artificial-neural-networks-d7834f67a4f6.

[56] Lopez, G., Rubio, M. A., Martınez, M., and Batlles, F. J. 2001. Estimation of hourly global photosynthetically active radiation using artificial neural network models. Agricultural and forest Meteorology, 107(4), 279-291.

[57] Zurada, J. M. 1992. Introduction to artificial neural systems (Vol. 8). St. Paul: West.

[58] Zhang, G., Patuwo, B. E., and Hu, M. Y. 1998. Forecasting with artificial neural networks:: The state of the art. International journal of forecasting, 14(1), 35-62.

[59] Sanjay, C., and Jyothi, C. 2006. A study of surface roughness in drilling using mathematical analysis and neural networks. The International Journal of Advanced Manufacturing Technology, 29(9), 846-852.

APPENDIX A
Summary Table for Previous

Researches

Appendix A

Summary Table for Previous Researches

A.1 PTSC System with water

Ref. NO.	Type of study	Type of fluid	Results
25	Exp.	water	The experimental results show that the maximum overall efficiency was 38.3%.
26	adaptive neuro fuzzy inference system (ANFIS)	Flat solar thermal energy system	The predicted values of ANFIS were found to be in very good agreement with the experimental values with mean relative errors (MRE) less than 3.26 % and 18% for the solar fractions and the preheat tank stratification temperatures respectively. Finally, the results demonstrate the effectiveness and reliability of the (ANFIS) method to predict the performances of energy systems.
27	Exp.	water	The experimental tests show that the adjusted absorber was recorded a higher solar energy recovery efficiency than a single tube where its efficiency was investigated about 42.1%.
28	Num.	water	The highest outlet temperature was recorded about 47.3°C in a constant flow rate of 0.2 L / min and solar irradiance of 783.58 W/m2 at 13 pm.

29	Exp. and Num.	water	the output parameters estimated from the numerical model were compared to the experimental outputs with deviations less than 10%.
30	Exp.	water	The experimental tests show that the overall loss coefficient decreases by 45% in case of absorber filled with metal foam and then lead to increase the efficiency by 3%.
31	Num.	water	The dimensions of collector were 2.44 m length, 1.04 m width and a focal length of 0.004 m.
33	Num.	water	The results were recorded a high output temperature about 150 °C at a pressure of 120 kpa. In the same manner, the highest efficiency was recorded about 46.48%.
34	artificial neural network	solar air heater arc shaped wire rib and smooth duct	The prediction results found that the structure of ANN-II with structure (8-14-1) was the optimal model as compared to other models. The values of MRE, SSE, and R^2 were found to be 1.82%, 0.02138 and 0.99387 respectively.

A.2 PTSC System with nonofluids

Ref. NO.	Type of study	Type of fluid	Results
35	Num.	Al_2O_3/synthetic oil	As compared with traditional PTSC, using Al2O3/synthetic oil nanofluid enhances and improves the heat transfer and thermal performance.
36	Num.	Cu-Therminol	The thermal efficiency of the system increases by 12.5% when the nanoparticle volume fraction increase to 6%.
37	Exp. & Num.	CuO/water	The results show that the thermal efficiency of the system directly depending on the nanoparticle volume fraction. Where, the efficiency of the system increases from 18 to 52 % when the volume fraction increase from (0.002 to 0.008) %.
38	Exp.	Al_2O_3/water	The maximum efficiency was recorded 55.8 % at mass flow rate and volume concentration (m= 0.05 kg/s and φ= 0.5 %).
39	Num.	Copper Therminol VP-1, silver Therminol, and	The results showed that the using of nanofluids improve the thermal efficiency and thermodynamic performance of a PTSC system. So, heat transfer coefficient increased

		Al$_2$O$_3$-Therminol	by 7.9 %, 6.4 % and 3.9 % while, the thermal efficiency of the PTSC system increased by 13.9%, 12.5% and 7.2% for silver-Therminol®VP-1, copper-Therminol and Al$_2$O$_3$-Therminol nanofluids, respectively as the volume fraction increased from 0 to 6 %.
40	Num.	3 % Al$_2$O$_3$/Oil, 3 % TiO$_2$/Oil and 1.5 % Al$_2$O$_3$-1.5% TiO$_2$/Oil	The mean thermal efficiency enhancement with the hybrid nanofluid was found 0.74 %, while with the TiO$_2$ nanofluid 0.341 % and with the Al$_2$O$_3$ nanofluid 0.340 % and the difference between these enhancements are about 10% and it is depended on the higher thermal conductivities of the nanofluids compared to the pure oil.
41	Num.	(SiO$_2$, Cu, Al2O$_3$, CuO, TiO$_2$ and Fe$_2$O$_3$) dispersed in thermal oil (Syltherm 800)	The maximum enhancement is observed for higher inlet temperatures, lower flow rates and higher nanoparticle concentrations. The enhancement of efficiency enhancement is found to be 31, 54, and 74 % for Cu concentrations 2, 4, and 6 %, respectively.
42	Exp.	TiO$_2$/DI-H$_2$O (De-Ionized water)	The maximum overall efficiency of the PTSC was recorded 57% when using TiO$_2$ nanofluid which is 9 % greater than that of the base fluid.

43	Num.	CuO nanoparticles in Syltherm 800 and in nitrate molten salt (40 % KNO_3 - 60 % $NaNO_3$)	According to the final results, using of oil-based nanofluids leads to enhance the efficiency up to 76 % as compared to a pure fluid. While, using of molten salt-based nanofluids enhanced up to 26 %. Using of Syltherm 800-CuO leads to enhance the efficiency to 65 % as compared to pure Syltherm.
44	Exp.	Al_2O_3/water nanofluid	The nanofluid with a 3% volume fraction reaches the maximum efficiency of 52.4 %, whereas in the case of water, this value was 40.8 %. While, in case of 1% volume concentration, a maximum efficiency reached to 57.7 % while in case of the water was 46.5 %.

45	Radial Basis Function Artificial Neural Network (RBF-ANN), Multi-Layers Perceptron Artificial Neural Network (MLP-ANN) and	flat-plate solar collector	The study indicate that all of these machine and deep learning algorithms are suitable for predicting nanofluid thermal performance in solar systems. However, as a compared between the three methods, the MLP-ANN was the accurate method for predicting the efficiency of flat-plate solar collector with a value of R^2 about 0.96.

	Elman Back Propagation Neural Network (Elamn BP-ANN)		
46	Artificial neural network (ANN) based Multi-Layer Perceptron (MLP-ANN) system	direct absorption solar collector	The statistical results show that the propose artificial neural network (ANN) approach proved that the collector depth has significant effect on the collector efficiency while the collector length has an insignificant effect. On the other side, the depth of collector and nanofluid flow rate have a significant effect on Nusselt number. Generally, a significant agreement between the predicted and experimental results confirms that the great ability of the (MLP-ANN) model to predict the output data.
47	used artificial neural network (ANN) and the genetic algorithm (GA)	PTSC system	The results show that the optimal mean square error (MSE) was 0.02288 for training stage, 0.02288 for validation stage and 0.0282 for testing with value of R^2 about 0.99999. It is determined that, within the constraints of the stated parameters, machine learning

			approaches can be an effective tool for predicting the rate of entropy formation in a collector.
48	artificial neural network (ANN)	flat-plate solar collector	The values of (R^2) were recorded 0.9862 and 0.9996 in cases of polynomial and ANN, respectively. Moreover, the average absolute relative deviation value was 5.25% and 0.881% for the indicated methods, respectively.
49	Artificial Neural Networks	an evacuated tube solar collector	The results showed that the MLP technique could forecast collector performance more accurately than the RBF method. The MLP model's greatest error rate was lower than the RBF model's. It was also discovered that increasing both the flow rate and concentration of the nanofluid improves

APPENDIX B

EXPERIMENTAL WORK

Appendix B

EXPERIMENTAL WORK

B.1 Reflective Design and Manufacture

The reflector is one of the most important parts of the solar collector system; it is designed by the method of theoretical calculations after determining the dimensions of the parabolic plate and applying them to the parabola equation:

$$x^2 = 4 F y \qquad (B.1)$$

In addition, some of software is available to calculate the design parameters of parabola. In this study, the dimensions of the PTSC were based on the Parabolic Calculator 0.2 software to calculate the optical focus position after entering the value of the arc diameter and depth (the vertical distance from the parabola to the edge of the arc). Finally, the program was calculated and determined the optical focus of the reflective surface as shown in the Figure B.1.
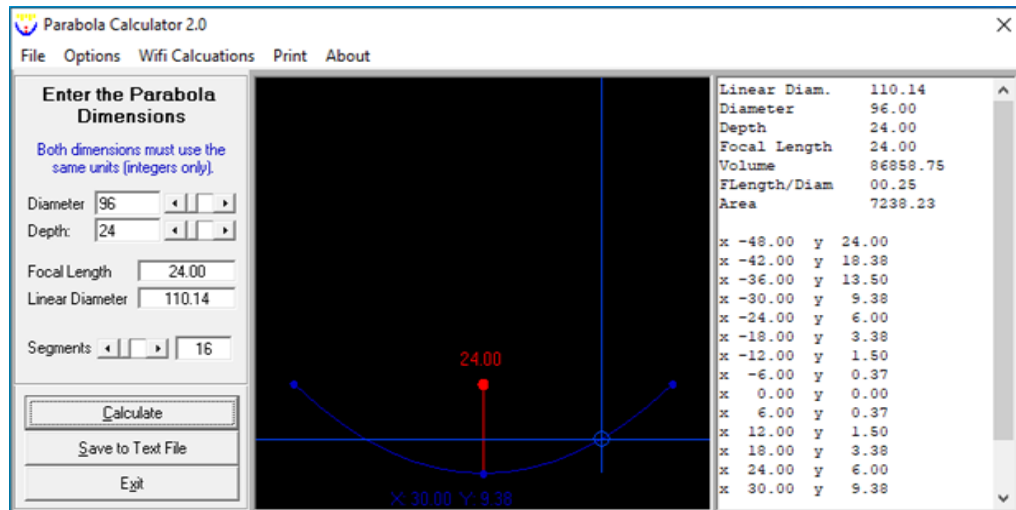
Figure B.1: Parabola dimensions from Parabola Calculator 2.0 software.

The length of reflector was proposed (2 m) depending on the length of the structure that assigned reflector. The rim angle of the designed parabolic trough was selected 90° to investigate the basis of focal length equal to the height of the parabola collector as well easily identified on the focal line.

B.2 Experimental instruments

(a) (b) (c)
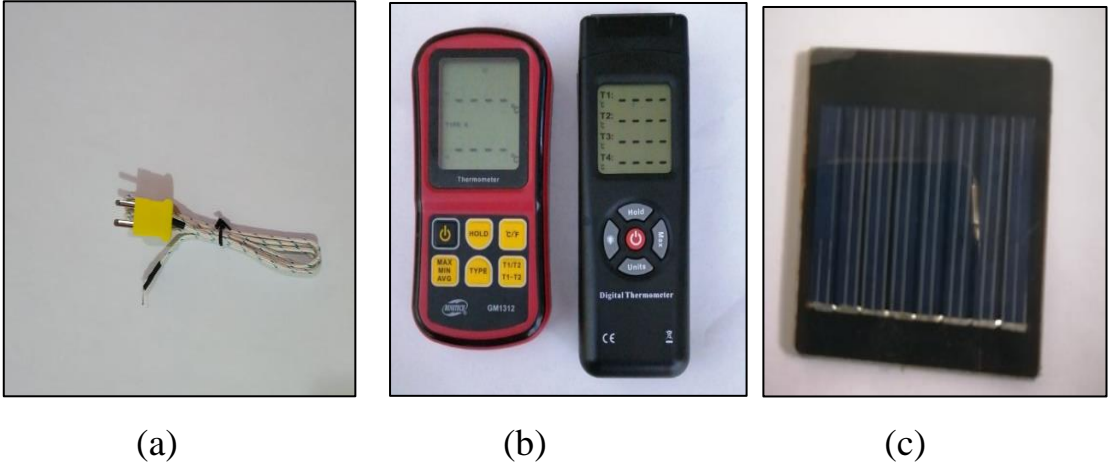
Figure B.2 (a) Thermocouples K-Type. (b) Digital thermometer system. (c) Solar cell.

(a) (b) (c)
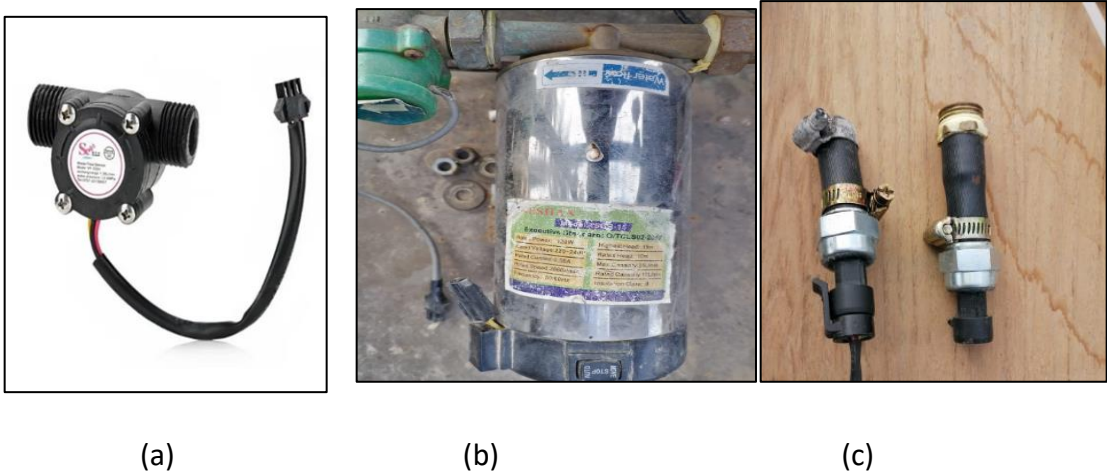
Figure B.3 (a) Fluid flow measurement sensor. (b) fluid pump. (c) Pressure sensors.
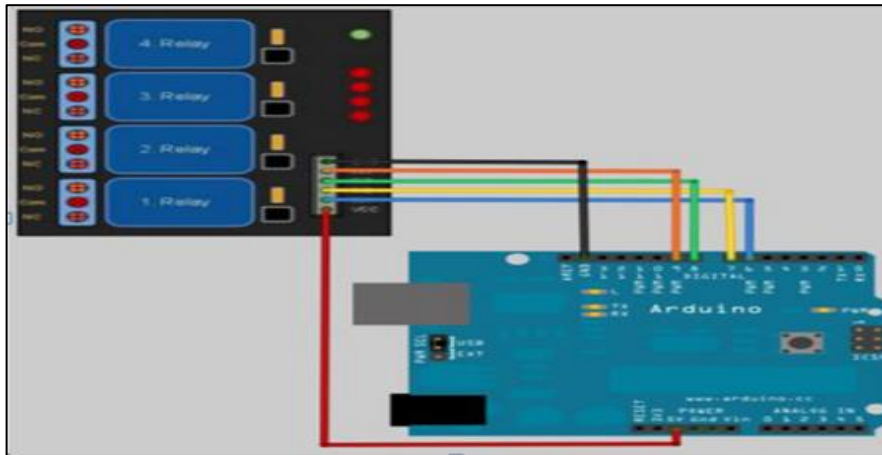
Figure B.4 Connect the Arduino to the relay circuit.

Figure B.5 Copper tube.

Figure B.6 Digital balance

B-3

B.3 Result

B.3.1 Water Experimental Results Table

Table B.1 Experimental results of water

Volumetric. flow	Time	$T_{in,}$ (č)	$T_{amb.}$ (č)	T_{out} (č)	T_r (č)	I (w/m²)	Q_u (w)	η%	ΔP (pas)	f
V̊=30 L/hr Water	9:00	15.2	9.3	18	20.3	378.7	99.31	13.42	1.45	0.068
	9:30	15.8	8.6	20.1	24.8	448.7	152.44	17.39	1.45	0.068
	10:00	17.6	9.6	25.4	31.6	522.5	276.09	27.04	1.45	0.068
	10:30	21.1	11.4	33.7	40.5	610.5	445.26	37.33	1.45	0.068
	11:00	24.6	13.7	39.4	47.2	678.2	522.22	39.41	1.45	0.069
	11:30	26.2	17.3	42.2	50.1	763.8	564.06	37.79	1.45	0.069
	12:00	31.4	23.7	51.4	53.8	823.6	703.66	43.72	1.45	0.069
	12:30	32.1	27.2	53.7	54.6	857.8	759.71	45.33	1.45	0.069
	13:00	34.3	24.8	52.3	56.2	835.3	632.72	38.77	1.45	0.069
	13:30	35.2	24.1	50.5	56	762.2	537.78	36.11	1.45	0.069
	14:00	37.4	22.6	51.4	55.2	647.5	491.94	38.88	1.45	0.069
	14:30	38.4	21.2	48.5	52.7	558.4	354.96	32.53	1.45	0.069
	15:00	35.6	22.6	43.8	49.8	487.2	288.56	30.31	1.45	0.069
	Time	$T_{in,}$ (č)	$T_{amb.}$ (č)	T_{out} (č)	T_r (č)	I (w/m²)	Q_u (w)	η%	ΔP (pas)	f
V̊=40 L/hr Water	9:00	16.3	10.2	18.6	22.1	397.5	108.71	14	1.6	0.042
	9:30	18.6	11.6	21.8	26.2	481.6	151.10	16.06	1.6	0.042
	10:00	19.1	12.9	24.5	33.4	570.7	254.79	22.85	1.6	0.042
	10:30	21.8	14.8	29	41.3	643.8	339.38	26.98	1.6	0.042
	11:00	23.1	18.2	32.5	48.9	730.3	442.63	31.02	1.6	0.043
	11:30	24.9	22.8	37.2	52.1	805.5	578.78	36.77	1.6	0.043
	12:00	26.7	24.2	41.9	54.2	822.7	714.58	44.45	1.6	0.043
	12:30	29.2	25.1	44	56.1	838.3	695.24	42.44	1.6	0.043
	13:00	31.6	25.7	44.8	56.8	794.1	619.64	39.93	1.6	0.043
	13:30	34.3	25.3	45.5	57.2	713.6	525.34	37.68	1.6	0.043
	14:00	36.1	24.8	46.2	55.8	637.4	473.67	38.03	1.6	0.043
	14:30	35.2	24.1	43.3	53.6	570.4	380.11	34.1	1.6	0.043
	15:00	33.6	23.6	39.4	51.4	497.5	272.39	28.02	1.6	0.043
	Time	$T_{in,}$ (č)	$T_{amb.}$ (č)	T_{out} (č)	T_r (č)	I (w/m²)	Q_u (w)	η%	ΔP (pas)	f
V̊= 60 L/hr Water	9:00	15.8	9.3	17.3	21.6	433.6	106.39	12.56	3	0.035
	9:30	17.2	11.3	19.5	26.4	476.3	163.03	17.52	3	0.035
	10:00	18.2	14.8	22	33.6	560.6	269.18	24.57	3	0.035
	10:30	19.6	16.2	24.6	42.4	617.7	353.92	29.32	3	0.035
	11:00	20.3	18.6	26.7	49.2	684.7	452.78	33.84	3	0.035
	11:30	22.5	26.4	29.7	51.4	760.2	508.90	34.26	3	0.035
	12:00	25.6	23.1	34.3	54.8	831.5	614.25	37.81	3	0.035

	Time	$T_{in,}$ (℃)	$T_{amb.}$ (℃)	T_{out} (℃)	T_r (℃)	I (w/m²)	Q_u (w)	η%	ΔP (pas)	f
	12:30	27.3	21.3	36.5	58.6	818.1	649.03	40.6	3	0.035
	13:00	30.1	20.9	38.5	57.1	727.6	592.21	41.65	3	0.035
	13:30	31.6	20.8	38.8	56.8	641.5	507.44	40.48	3	0.035
	14:00	33.7	18.9	40.2	56.2	609.2	458.07	38.48	3	0.036
	14:30	32.4	19.6	37.1	53.4	535.9	331.38	31.65	3	0.035
	15:00	31.5	18.2	34.9	52.1	443.6	239.83	27.67	3	0.035
	Time	$T_{in,}$ (℃)	$T_{amb.}$ (℃)	T_{out} (℃)	T_r (℃)	I (w/m²)	Q_u (w)	η%	ΔP (pas)	f
$\mathring{V}$=80 L/hr Water	9:00	16.7	10.1	18.4	23.1	412.6	160.72	19.94	5	0.033
	9:30	18.3	9.6	20.3	27.6	478.3	188.96	20.22	5	0.033
	10:00	20.3	10.8	23.3	32.8	575.6	283.20	25.18	5	0.033
	10:30	21.1	13.3	25	40.2	637.5	368.01	29.54	5	0.033
	11:00	22.8	15.4	28.1	50.4	705.7	499.82	36.25	5	0.033
	11:30	24.1	14.5	30.1	53.2	733.6	565.51	39.45	5	0.033
	12:00	26.2	15.2	32.6	58.3	776.6	602.48	39.7	5	0.033
	12:30	30.1	16.4	36.4	60.5	826.1	592.30	36.69	5	0.033
	13:00	32.9	24	37.8	61.2	759.4	460.45	31.03	5	0.033
	13:30	33.4	20.6	38	58.6	667.9	432.32	33.13	5	0.033
	14:00	32.6	21	36.9	56.1	657.8	404.28	31.45	5	0.033
	14:30	31.8	19.2	34.9	53.2	578	291.62	25.82	5	0.033
	15:00	30.5	19.1	32.7	48.4	458.5	207.04	23.11	5	0.033

B.3.2 CuO-water Experimental Results Table

Table B.2: Experimental results of CuO/ water

Volumetric. flow	Time	$T_{in,}$ (℃)	$T_{amb.}$ (℃)	T_{out} (℃)	T_r (℃)	I (w/m²)	Q_u (w)	η%	ΔP (pas)	f
	9:00	16.1	10.2	19.1	24.4	447.5	104.13	11.91	1.7	0.082
	9:30	17.7	12.8	23.9	30.8	546.4	214.85	20.12	1.7	0.073
	10:00	21.6	15.4	31.7	40.1	634.3	349.45	28.19	1.7	0.073
	10:30	25.1	16.5	38.9	46.6	712.5	476.74	34.24	1.7	0.073
	11:00	28.6	18.8	46.3	51.6	781.8	610.67	39.97	1.7	0.073
$\mathring{V}$=30 L/hr CuO-water nanofluid	11:30	31.3	20.6	54.1	57.5	820.5	785.32	48.98	1.7	0.073
	12:00	33.7	22.6	58.3	64.3	844.3	845.75	51.26	1.7	0.073
	12:30	37.3	23.7	63.7	67.6	850.3	906.26	54.55	1.7	0.073
	13:00	40.7	24.7	66.1	68.7	836.7	871.31	53.29	1.7	0.073
	13:30	44.3	21.2	66.9	69.6	796.2	774.74	49.8	1.7	0.073
	14:00	45.8	20.4	64.5	67.8	753.8	641.26	43.54	1.7	0.073
	14:30	44.3	19.1	58.9	65.2	686.5	501.22	37.36	1.7	0.073
	15:00	43.2	18.7	53.7	58.2	628.6	360.92	29.38	1.7	0.073
	Time	$T_{in,}$ (℃)	$T_{amb.}$ (℃)	T_{out} (℃)	T_r (℃)	I (w/m²)	Q_u (w)	η%	ΔP (pas)	f
	9:00	14.6	9.3	17.5	28.6	491.6	136.33	14.19	2	0.048

B-5

	Time	$T_{in,}$ (℃)	$T_{amb.}$ (℃)	T_{out} (℃)	T_r (℃)	I (w/m^2)	Q_u (w)	η%	ΔP (pas)	f
	9:30	15.2	11.6	19.4	31.2	546.4	197.17	18.47	2	0.054
	10:00	18.8	12.5	25.9	42.6	600.8	332.87	28.35	2	0.054
	10:30	21	14.7	31.6	47.5	676.9	496.29	37.52	2	0.054
	11:00	25.5	13.3	39.2	55.3	798.4	640.70	41.07	2	0.054
	11:30	29.8	14.8	45.9	61.7	876.4	751.83	43.9	2	0.054
$\mathring{V}$=40 L/hr CuO/Water	12:00	34.2	18.6	52.7	67.1	934.6	862.43	47.23	2	0.055
	12:30	38.5	20.3	58.1	69.2	861.5	912.74	54.22	2	0.055
	13:00	43.8	21.8	61.6	72.8	834.9	827.96	50.75	2	0.055
	13:30	47.6	19.2	63.4	73.1	795.3	734.60	47.27	2	0.055
	14:00	47.1	18.6	59.8	71.6	736.5	590.49	41.03	2	0.055
	14:30	45.1	18.2	55.5	66.2	647.4	483.81	38.24	2	0.055
	15:00	42.9	17.4	50.1	62.1	588.1	335.20	29.17	2	0.055
	Time	$T_{in,}$ (℃)	$T_{amb.}$ (℃)	T_{out} (℃)	T_r (℃)	I (w/m^2)	Q_u (w)	η%	ΔP (pas)	f
	9:00	17.6	11.6	20	26.2	425.8	169.38	20.36	4.4	0.047
	9:30	20.3	12.4	23.5	31.2	518.5	225.61	22.27	4.4	0.047
	10:00	22.4	14.2	27.6	42.2	622.6	366.23	30.1	4.4	0.047
	10:30	25.8	16.8	32.1	49.2	705.7	443.16	32.14	4.4	0.047
	11:00	29.1	18.1	38.4	56.2	768.9	653.07	43.47	4.4	0.047
	11:30	34.8	20.1	46.2	62.1	820.8	798.89	49.81	4.4	0.047
$\mathring{V}$=60 L/hr CuO/Water	12:00	36.2	22.4	48.9	69.3	855.3	889.43	53.22	4.4	0.047
	12:30	40.6	23.3	52.2	72.2	863.9	810.87	48.04	4.4	0.047
	13:00	42.3	24.1	52.7	71	849.8	726.79	43.77	4.4	0.047
	13:30	44.2	21.5	52.7	74.1	812.9	594.01	37.4	4.4	0.047
	14:00	43.1	19.6	50.6	72.3	744.3	524.48	36.06	4.4	0.047
	14:30	41.8	17.8	48.2	68.6	694.5	447.90	33.01	4.4	0.047
	15:00	39.6	17.1	43.8	64.5	632.8	294.22	23.8	4.4	0.047
	Time	$T_{in,}$ (℃)	$T_{amb.}$ (℃)	T_{out} (℃)	T_r (℃)	I (w/m^2)	Q_u (w)	η%	ΔP (pas)	f
	9:00	19.2	9.8	21.2	23.2	380.3	188.11	25.31	7.3	0.044
	9:30	21.2	10.3	23.6	26.1	487.1	225.65	23.71	7.3	0.044
	10:00	23.7	13.4	27.3	35	596.4	338.35	29.03	7.3	0.044
	10:30	26.8	15.2	31.5	40.7	698.3	441.62	32.37	7.3	0.044
	11:00	29.7	17.6	36	52	796.5	591.86	38.03	7.3	0.044
	11:30	33.8	20.1	41.3	56.6	825.8	704.52	43.66	7.3	0.044
$\mathring{V}$=80 L/hr CuO/Water	12:00	37.2	23.5	45.8	59.3	852.4	807.84	48.5	7.3	0.044
	12:30	41.6	24.4	50.7	61.3	878.8	854.83	49.78	7.3	0.044
	13:00	43.3	25.5	50.7	63.5	852.8	695.15	41.72	7.3	0.043
	13:30	45.1	22.7	51.8	62.1	820.9	629.38	39.24	7.3	0.043
	14:00	42.3	19.8	47.7	59.1	773.1	507.25	33.58	7.3	0.044
	14:30	39.6	18.5	44.2	54.1	685.4	432.10	32.26	7.3	0.044
	15:00	36.7	18	39.8	49.4	576.8	291.20	25.84	7.3	0.044

B.3.1 TiO₂- Water Experimental Results Table

Table B.3: Experimental results of TiO$_2$-water nanofluid

Volumetric. flow	Time	T_{in} (c̊)	$T_{amb.}$ (c̊)	T_{out} (c̊)	T_r (c̊)	I (w/m²)	Q_u (w)	η%	ΔP (pas)	f
	9:00	19.6	17.6	22.8	24.7	418.4	105.86	12.95	1.6	0.071
	9:30	21	18.2	26.6	29.6	487.2	185.09	19.44	1.6	0.071
	10:00	22.9	19.6	31.6	36.6	552.3	287.16	26.61	1.6	0.071
	10:30	26.1	20.7	39.2	45.2	646.7	431.66	34.16	1.6	0.071
	11:00	30.9	21	48.1	50.7	738.2	565.98	39.24	1.6	0.071
V̊=30 L/hr	11:30	32.2	22.2	53.7	56.3	828.4	706.33	43.64	1.6	0.071
TiO₂-water	12:00	35.7	23.8	57.8	61.1	826.5	724.65	44.87	1.6	0.071
nanofluid	12:30	39.8	26.1	63.7	64.6	863.8	782.35	46.35	1.6	0.071
	13:00	41.9	24.8	64.6	66.8	842.4	742.50	45.11	1.6	0.072
	13:30	44.2	25.2	64.8	65.4	786.2	673.35	43.83	1.6	0.072
	14:00	45.4	23.2	62.9	64.2	718.6	572.09	40.74	1.6	0.072
	14:30	43.7	22.8	57.4	60.3	626.3	448.36	36.64	1.6	0.071
	15:00	42.6	22.2	52.4	56.7	558.6	321.10	29.42	1.6	0.071
	Time	T_{in} (c̊)	$T_{amb.}$ (c̊)	T_{out} (c̊)	T_r (c̊)	I (w/m²)	Q_u (w)	η%	ΔP (pas)	f
	9:00	18.6	19.5	21.2	25	452.3	122.02	13.81	1.9	0.047
	9:30	18.9	20.7	22.4	28.5	527.7	164.10	15.91	1.9	0.047
	10:00	20.3	21.8	26.1	34	616.4	271.63	22.55	1.9	0.047
	10:30	22.4	23.1	31.1	42.6	694.8	406.98	29.98	1.9	0.047
	11:00	25.1	22.1	36.7	46.5	780.7	542.07	35.53	1.9	0.048
V̊=40 L/hr	11:30	30.7	23.8	44.5	51.7	833.2	643.74	39.54	1.9	0.048
TiO₂-water	12:00	35.3	24.7	51.4	58.5	852.7	749.81	45	1.9	0.048
nanofluid	12:30	38.7	27.2	56	62.6	872.3	804.76	47.21	1.9	0.048
	13:00	41.2	26.3	57.9	63.7	841.9	776.23	47.19	1.9	0.048
	13:30	43.2	23.4	57	64	786.3	641.04	41.72	1.9	0.048
	14:00	42.6	22.4	54.9	62	725.9	571.75	40.31	1.9	0.048
	14:30	40.8	21.6	49.5	59.3	614.9	404.87	33.7	1.9	0.048
	15:00	37.4	21.1	44.4	55.4	546.8	326.24	30.53	1.9	0.048
	Time	T_{in} (c̊)	$T_{amb.}$ (c̊)	T_{out} (c̊)	T_r (c̊)	I (w/m²)	Q_u (w)	η%	ΔP (pas)	f
	9:00	19.3	17.3	21.3	25	414.3	140.82	17.4	3.6	0.04
	9:30	19.7	18.5	22.2	28.5	478.7	175.85	18.8	3.6	0.04
	10:00	20.3	19.8	24.9	34	546.4	323.24	30.28	3.6	0.04
V̊=60 L/hr	10:30	22.5	21.4	28.1	42.6	631.8	393.04	31.84	3.6	0.04
TiO₂-water	11:00	24.7	22.9	33	46.5	705.7	581.70	42.18	3.6	0.04
nanofluid	11:30	27.8	21.7	37.4	51.7	787.2	671.73	43.67	3.6	0.04
	12:00	32.6	23.6	42.8	58.5	824.7	712.69	44.23	3.6	0.04
	12:30	37.8	25.7	48.5	62.6	840.3	746.86	45.49	3.6	0.04

	Time	$T_{in,}$ (c)	$T_{amb.}$ (c)	T_{out} (c)	T_r (c)	I (w/m²)	Q_u (w)	η%	ΔP (pas)	f
	13:00	41.6	26.6	50.8	63.7	823.9	641.90	39.87	3.6	0.04
	13:30	43.3	24.8	51.4	64	767.3	565.38	37.71	3.6	0.04
	14:00	40.8	23.1	47.8	62	755.9	489.03	33.11	3.6	0.04
	14:30	38.6	22.5	44	59.3	694.9	377.55	27.81	3.6	0.04
	15:00	36.8	20.9	40.4	55.4	606.8	251.90	21.25	3.6	0.04
	Time	**$T_{in,}$ (c)**	**$T_{amb.}$ (c)**	**T_{out} (c)**	**T_r (c)**	**I (w/m²)**	**Q_u (w)**	**η%**	**ΔP (pas)**	**f**
$\overset{\circ}{V}$=80 L/hr TiO₂-water nanofluid	9:00	20.4	18.3	22.2	23.4	479	168.98	18.05	6.2	0.039
	9:30	22.8	19.8	24.9	28.7	562	196.95	17.93	6.2	0.039
	10:00	24.9	21.3	28.1	34.2	750.6	299.82	20.44	6.2	0.039
	10:30	27.2	22.7	31.6	42.9	768.2	411.76	27.43	6.2	0.039
	11:00	30.1	24.4	35.9	46.5	833.9	541.99	33.26	6.2	0.039
	11:30	32.3	26.6	39	52.7	886.7	625.08	36.08	6.2	0.039
	12:00	34.4	27.8	41.5	58.8	896.5	661.45	37.76	6.2	0.039
	12:30	38.2	27.2	46	63.6	835	725.92	44.49	6.2	0.039
	13:00	40.7	25.6	46.8	64.8	796	567.48	36.48	6.2	0.039
	13:30	39.8	24.5	45.5	64	732	530.48	37.09	6.2	0.039
	14:00	37.4	23.7	42.5	62.5	615	475.06	39.53	6.2	0.039
	14:30	35.8	22.4	39.8	59.6	523	372.89	36.49	6.2	0.039
	15:00	33.4	21.5	36.4	55.4	436	279.89	32.85	6.2	0.039

B-8

APPENDIX C
SPECIFICATIONS OF
THE SYSTEM

APPENDIX C

SPECIFICATIONS OF THE SYSTEM

C.1 Specifications of temperature recorder

1- Model: GM-1312 SD

2- 4 channels Temperature recorder, use SD card to save the data along with time information

3- Real time recorder, save the measuring data along the time information (year, month, date, minute, second) into the SD memory card and can be download to the Excel, extra software is no need.

4- Sensor type: Type J/K/T/E/R/S thermocouple.

5- Auto recorder or manual recorder.

6- Recorder sampling time range: 1 to 3600 second.

7- Type K thermometer: -100 to 1300 C.

8- Show CH1 to CH8 or CH9 to CH12 in the same LCD.

9- Display resolution: 1 degree/0.1 degree.

10- Time information: Year, Month, Date, Hour, Minute and Second.

11- Memory card size: 1 GB to 16 GB.

12- Data hold, Record (Max., Min.).

13- RS232 (optional)/USB computer interface.

14- DC Power supply.

C.2 Specifications of cell

1-Working temperature: (-40)-(+65) C°

2-Output signal: 0-3V

3-Supply voltage: 3,3-15V DC, allowed ripple voltage - 100mV

4-Sensing element fotodiode

5-Radiation intensity range: 0 … 1500 W/m2

6-Sensitivity: 2mV per W/m2

7-Accuracy: ±0.499%

8-Sensitivity range: 300 – 1000 nm

9-Response time: <1 second

10-Non-linearity: <± 1%

11-Long-term stability: <±/2% yr

12-Temperature influence on the measurement-: + 0,15% C°

13-Protection: IP67

14-Weight: 138g

15-Cable length 1m, optional extension

C.3 Specifications of flow meter

1-Sensor Type: Hall effect

2-Working Voltage: 5 to 18V DC (min tested working voltage 4.5V)

3-Max current draw: 15mA @ 5V

4-Output Type: 5V TTL

5-Working Flow Rate: 1 to 30 Liters/Minute

6-Working Temperature range: -25 to +80°C

7-Working Humidity Range: 35%-80% RH

8-Accuracy: ±10%

9-Maximum water pressure: 2.0 MPa

10-Output duty cycle: 50% +-10%

11-Output rise time: 0.04

12-Output fall time: 0.18

13-Flow rate pulse characteristics: Frequency (Hz) = 7.5 * Flow rate (L/min)

14-Pulses per Liter: 450

15-Durability: minimum: 300,000 cycles

16-Cable length: 15cm

17-1/2″ nominal pipe connections, 0.78″ outer diameter, 1/2″ of thread

18-Size: 2.5″ x 1.4″ x 1.4

C.4 Specifications of pump

Power Consumption 120 W

Power Supply 220V/50HZ

Max Capacity 1.2 m^3/hr

Max Head : 12 m

Pipe Diameter 1/2

Max section 4 m

RPM : 2850 rpm

C.5 Specifications of pressure sensor

1-Working Voltage: 5VDC

2-Output Voltage: 0.5-4.5 VDC

3-Sensor material: Carbon steel alloy

4-Working Current: 10 mA

5-Working Pressure Range: 0-1.2 MPa

6-The Biggest Pressure: 2.4 MPa

7-Cable length: 19cm

8-Destroy Pressure: 3.0 MPa

9-Working TEMP. Range: 0-85

10-Storage Temperature Range: 0-100

11-Measuring Error: 1.5 %FSO

12-Temperature Range Error: 3.5 %FSO

13-Response Time: 2.0 ms

14-Cycle Life: 500,000 pcs

C.6 Specifications of the Arduino UNO

Microcontroller: ATmega 328

Operation voltage: 5V

Input voltage (recommended): 7-12V

Input voltage (limits): 6-20V

Digital I/O pins: 14 (of which 6 provide PWM output

Analogue input pins: 6

DC current per I/O pin: 40 mA

DC current for 3.3V pin: 50 mA

Flash memory: 32 KB (ATmega 328) of which o.5 KB used by boot loader

S RAM: 2 KB (ATmega 328)

EEPROM: 1KB (ATmega 328)

Clock speed: 16 MHz

Appendix D
Uncertainty Analysis and Calibration

Appendix D

Uncertainty Analysis and Calibration

D.1 Uncertainty Analysis

D.1.1 Uncertainty of Key Parameters

The uncertainties of key various parameters are presented in follow Table.

Table D.1.1: The primary uncertainties for various parameters.

NO.	Variable	Uncertainty
1	Tube length, L	± 1.0 mm
2	The inner diameter of tube, d_{ri}	± 0.1 mm
3	Inlet temperature, T_{in}	$\pm 0.95\%$
6	outlet temperature, T_{out}	$\pm 0.95\%$
9	Surface temperature, T_s	$\pm 0.95\%$
10	Mass flow rate, $\dot{m}$	$\pm 5.0\%$
11	Pressure drop, Δp	3.53%

D.1.2 Uncertainty of Hydraulic Diameter

The hydraulic diameter was displayed in equation 4.5 as follows:

$$D_h = d_{ri} \tag{D.1}$$

The uncertainty of hydraulic diameter is expressed by:

$$U_{D_h} = \pm \sqrt{\left(\frac{\partial D_h}{\partial d_{ri}} U_{d_{ri}}\right)^2} \qquad (D.2)$$

Where

$$\frac{\partial D_h}{\partial d_{ri}} = 1 \qquad (D.3)$$

Substitute this value in equation D.2 as follows:

$$U_{D_h} = \pm \sqrt{\left(U_{d_{ri}}\right)^2} \qquad (D.4)$$

Substitute the value of dr_i from Table D.1 in above equation expresses:

$$U_{D_h} = \pm \sqrt{(0.1)^2} = \pm 0.1 \; mm \qquad (D.5)$$

Furthermore, the relative uncertainty is determined as follows:

$$\frac{U_{D_h}}{D_h} = \pm \frac{0.1}{22.3} = \pm 0.45 \; \% \qquad (D.6)$$

D.1.3 Uncertainty of Cross Sectional Area

The cross-sectional area was:

$$A_c = \frac{\pi D_h^2}{4} \qquad (D.7)$$

And the cross sectional area uncertainty (A_c) is computed as follows:

$$U_{A_c} = \pm \frac{1}{A_c} \sqrt{\left(\frac{\partial A_c}{\partial D_h} U_{D_h}\right)^2} \qquad (D.8)$$

Where

$$\frac{\partial A_c}{\partial D_h} = \frac{\pi D_h}{2} = \frac{2A_c}{D_h} \qquad (D.9)$$

Substitute the above terms in equation D.8 as follows:

$$U_{A_c} = \pm \sqrt{\left(\frac{2U_{D_h}}{D_h}\right)^2} \qquad (D.10)$$

$$= \pm \sqrt{\left(\frac{2 * 0.141}{23}\right)^2} = \pm 0.00901 \; mm^2 \qquad (D.11)$$

The relative uncertainty of A_c is obtained as follows:

$$\frac{U_{A_c}}{A_c} = \pm \frac{0.00901}{387.076} = \pm 0.00233 \; \% \qquad (D.12)$$

D.1.4 Uncertainty of Surface Area

The surface area of the inner tube is given as:

$$A_s = \pi d_{ri} L \qquad (D.13)$$

The relative uncertainty of A_S is evaluated as follows:

$$\frac{U_{A_S}}{A_S} = \pm \frac{1}{A_S} \sqrt{\left(\frac{\partial A_S}{\partial dr_i} U_{dr_i}\right)^2 + \left(\frac{\partial A_S}{\partial L} U_L\right)^2} \qquad (D.14)$$

Here,

$$\frac{\partial A_S}{\partial d_{ri}} = \frac{A_S}{d_{ri}} \qquad (D.15)$$

$$\frac{\partial A_S}{\partial L} = \frac{A_S}{L} \qquad (D.16)$$

Substituting the above terms in equation D.14 gives:

$$\frac{U_{A_S}}{A_S} = \pm \sqrt{\left(\frac{U_{dri}}{d_{ri}}\right)^2 + \left(\frac{U_L}{L}\right)^2} \qquad (D.17)$$

$$= \pm \sqrt{\left(\frac{0.1}{22.3}\right)^2 + \left(\frac{1}{2000}\right)^2} = \pm 0.453\% \qquad (D.18)$$

D.1.5 Uncertainty of Reynolds Number

Reynolds number can be expressed as follows:

$$Re = \frac{4\dot{m}}{\pi D_h \mu} \qquad (D.19)$$

The Reynolds number uncertainty is presented as follows:

$$U_{Re} = \pm \sqrt{\left(\frac{\partial Re}{\partial \dot{m}} U_{\dot{m}}\right)^2 + \left(\frac{\partial Re}{\partial D_h} U_{D_h}\right)^2} \qquad (D.20)$$

Where,

$$\frac{\partial Re}{\partial \dot{m}} = \frac{4}{\pi D_h \mu} = \frac{Re}{\dot{m}} \qquad (D.21)$$

$$\frac{\partial Re}{\partial D_h} = \frac{-4\dot{m}}{\pi D_h{}^2 \mu} = \frac{-Re}{D_h} \qquad (D.22)$$

Substituting these terms in equation D.20, thus, the relative uncertainty of Reynolds number is presented as:

$$\frac{U_{Re}}{Re} = \pm \sqrt{\left(\frac{U_{\dot{m}}}{\dot{m}}\right)^2 + \left(\frac{U_{D_h}}{D_h}\right)^2} \qquad (D.23)$$

$$= \pm \sqrt{\left(\frac{0.0000665}{0.00133}\right)^2 + \left(\frac{0.1}{22.2}\right)^2} = \pm 5.0202\% \qquad (D.24)$$

D.1.6 Friction Factor Uncertainty

The friction factor was expressed as follows:

$$f = \frac{2\Delta p \, \rho \, A_c^2}{\dot{m}^2} \frac{D_h}{L} \qquad (D.25)$$

The friction factor uncertainty is as shown by:

$$U_f = \pm \sqrt{\begin{array}{l} \left(\dfrac{\partial f}{\partial \Delta p} U_{\Delta p}\right)^2 + \left(\dfrac{\partial f}{\partial \dot{m}} U_{\dot{m}}\right)^2 + \left(\dfrac{\partial f}{\partial A_c} U_{A_c}\right)^2 \\[2mm] + \left(\dfrac{\partial f}{\partial D_h} U_{D_h}\right)^2 + \left(\dfrac{\partial f}{\partial L} U_L\right)^2 \end{array}} \qquad (D.26)$$

Where

$$\frac{\partial f}{\partial \Delta p} = \frac{2\rho\, A_c^2}{\dot{m}^2}\frac{D_h}{L} = \frac{f}{\Delta p} \tag{D.27}$$

$$\frac{\partial f}{\partial \dot{m}} = \frac{-4}{\dot{m}}\frac{\Delta p\, \rho\, A_c^2}{\dot{m}^2}\frac{D_h}{L} = \frac{-2}{\dot{m}}f \tag{D.28}$$

$$\frac{\partial f}{\partial A_c} = \frac{4\Delta p\, \rho\, A_c}{\dot{m}^2}\frac{D_h}{L} = \frac{f}{A_c} \tag{D.29}$$

$$\frac{\partial f}{\partial D_h} = \frac{2\Delta p\, \rho\, A_c^2}{\dot{m}^2}\frac{1}{L} = \frac{f}{D_h} \tag{D.30}$$

$$\frac{\partial f}{\partial L} = \frac{-2\Delta p\, \rho\, A_c^2}{\dot{m}^2}\frac{D_h}{L} = \frac{-f}{L} \tag{D.31}$$

Substituting above terms in equation D.26, thus, the relative uncertainty of friction factor is expressed by:

$$\frac{U_f}{f} = \pm\sqrt{\left(\frac{U_{\Delta p}}{\Delta p}\right)^2 + \left(\frac{-2U_{\dot{m}}}{\dot{m}}\right)^2 + \left(\frac{2U_{A_c}}{A_c}\right)^2 + \left(\frac{U_{D_h}}{D_h}\right)^2 + \left(\frac{-U_L}{L}\right)^2} \tag{D.32}$$

$$\frac{U_f}{f}$$

$$= \pm\sqrt{\left(\frac{0.2284}{6.47}\right)^2 + \left(\frac{-2*0.0000665}{0.00133}\right)^2 + \left(\frac{2*0.00901}{387.076}\right)^2 + \left(\frac{0.1}{22.3}\right)^2 + \left(\frac{1.0}{2000}\right)^2}$$

$$= \pm 10.615\% \tag{D.33}$$

D.1.7 Uncertainty in Q_u

The heat received by base fluid was displayed given by:

$$Q_u = \dot{m} \, C_{p,w} \, (T_{out} - T_{in}) \tag{D.34}$$

The uncertainty of Q_c is achieved by:

$$U_{Q_u} = \pm \sqrt{\left(\frac{\partial Q_u}{\partial \dot{m}} U_{\dot{m}}\right)^2 + \left(\frac{\partial Q_u}{\partial \Delta T} U_{\Delta T}\right)^2} \tag{D.35}$$

Where

$$\frac{\partial Q_u}{\partial \dot{m}} = C_{p,w} \, \Delta T = \frac{Q_u}{\dot{m}} \tag{D.36}$$

$$\frac{\partial Q_u}{\partial \Delta T} = \dot{m} \, C_{p,w} = \frac{Q_u}{\Delta T} \tag{D.37}$$

From equations D.36 and D.37 and re-arranging equation D.35, hence the relative uncertainty of Q_u is determined as:

$$\frac{U_{Q_u}}{Q_u} = \pm \sqrt{\left(\frac{U_{\dot{m}}}{\dot{m}}\right)^2 + \left(\frac{U_{\Delta T}}{\Delta T}\right)^2} \tag{D.38}$$

Here,

$$\frac{U_{\Delta T}}{\Delta T} = \pm \sqrt{\left(\frac{U_{T_{in}}}{T_{in}}\right)^2 + \left(\frac{U_{T_{out}}}{T_{out}}\right)^2} \qquad (D.39)$$

$$= \pm \sqrt{\left(\frac{0.228}{24}\right)^2 + \left(\frac{0.2736}{28.8}\right)^2}$$

$$= \pm 1.3435\% \qquad (D.40)$$

Substitute the above equation in equation D.38 gives:

$$\frac{U_{Q_u}}{Q_u} = \pm \sqrt{\left(\frac{0.0000665}{0.00133}\right)^2 + \left(\frac{0.0456}{4.8}\right)^2}$$

$$= \pm 5.09\% \qquad (D.41)$$

D.2 Calibration

D.2.1 Thermocouples (type K) Calibration

Standards were implemented on a thermometer in the laboratories of the Standardization and Quality Control Unit. This thermometer was adopted as a secondary reference for calibrating the K-type thermocouples used in this research, at different temperature ranges.
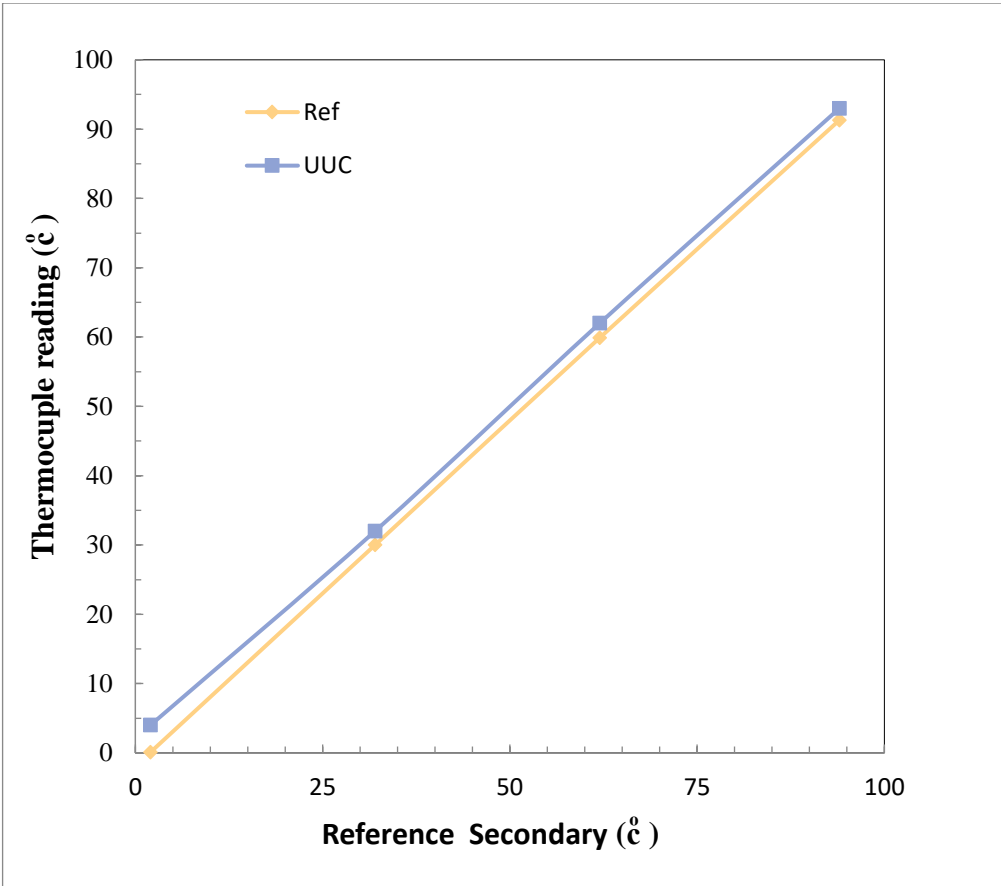

Figure D.2.1: Calibration curve of K-type thermocouples.

Appendix E

Artificial Neural Network

Appendix E

Artificial Neural Network

E.1. Artificial Neural Network Models (ANNₛ)

 The theory and design of the artificial neural network have advanced significantly over the past years. The purpose of ANNₛ is to provide an algorithms solution for complex problems such as classification, clustering, data compression, pattern coupling, function approximation, prediction, control, and optimization applications. In this section, the concept of ANNₛ and the design of ANNₛ structures are briefly introduced. On the other side, the normalization process is summarized. Artificial intelligence models have become the preferred trend for predicting the performance of solar thermal systems due to their ability to learn and adapt to change with little human interaction. The ANN model has a lot of capabilities compared to the traditional methods . A simple design of ANN is shown in Figure E.1
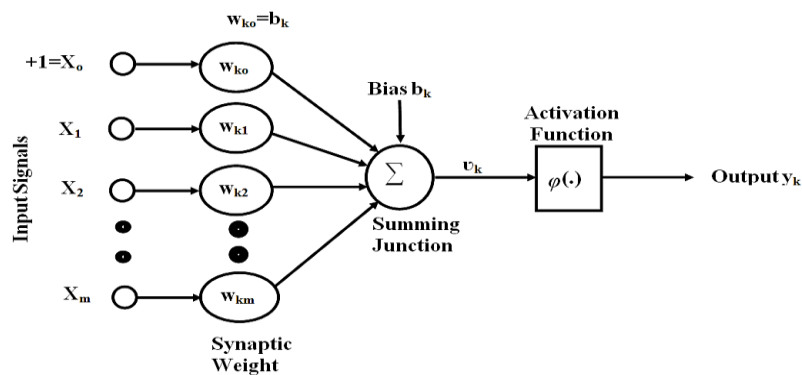
Figure E.1: simplified Artificial Network.

E.1.2 Components of ANN:

E.1.2.A The basic components of an artificial neural network

The general structure of artificial neural networks is formed as shown in Figure E.2 and consisted from:
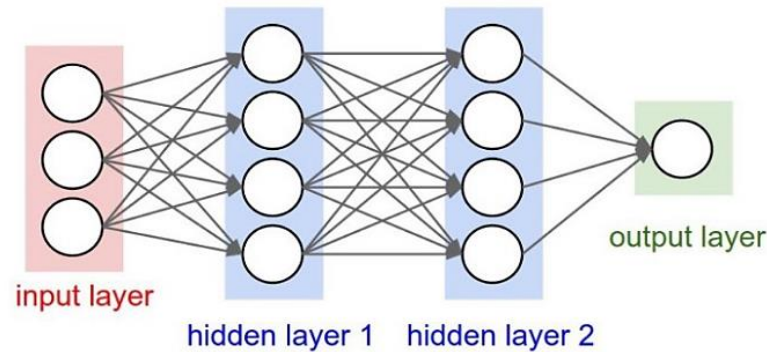
Figure E.2: Artificial neural network architecture model .

1. **Input layer:** It is the process of feeding the input data to receive it by the processing units of the neurons. The processing unit in the input layer does not carry out any arithmetic processing, but only transfers the input data from the input layer to the interfaces (weights) to the processing unit that located in the layer after the input layer .

2. **Output layer:** This layer consists of processing units through which the final output of the neural network is output. This layer contains one or more processing units depending on the network architecture. The process units in the output layer receive the signal coming to it from the previous layer. Usually there is only one output layer in the neural network architecture.

3. **Hidden layer:** This layer is located between the input layer and the output layer. Neural networks come with no hidden layer, one or more hidden layers. The hidden layer receives the signals coming to it from the input layer

through the interfaces. After this, the data is processed and the necessary calculations are made and send through the interfaces to the output layer.

4. **Weights:** It is the communication links between the different layers of the neural network. It connects network layers together or units within each layer to other units through the weights associated with each interface .

5. **Neurons:** Neurons are the units that connected in different ways by giving the overall shape or architecture of the artificial neural network. Neurons follow a parallel processing system that resembles the functioning of the human brain.

E.1.2.B The basic components of neurons

1. Weighting Coefficients: Weight is the main element in artificial neural networks. It represents the various links through which data is transferee from one layer to another. Weight expresses the relative strength and importance of each input to the processing element. Weights represent the main meaning of neural network memory by adjusting weights and symbolizing the weight between two processing elements Wij. Before training the network, the initial values of the weights and biases may be set but sometimes, these values need to re-change to get the optimum weights which can be adopted in forecasting . However, there is no specific way to make a good initial estimation of weights, so it relies on automatically assigning random initial values, and when the training process is finished all weights must be fixed.

2. Summation Function: The first operation performed by the processing unit is the calculation the sum of the weighted inputs coming to the unit using the summation function. Where, this function calculates the average weights for all the inputs to the processing unit and this is done by multiplying each

value entered by its accompanying weight and then finding the sum of all the products of the multiplication.

$$S_i = \sum_{i=1}^{m} x_i * W_{ij} + b \qquad\qquad (E.1)$$

X= input values

b = Represents the bias value. There are default values for bias values within MATLAB.
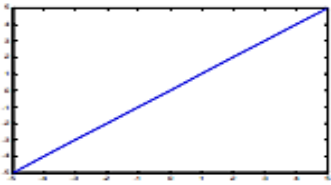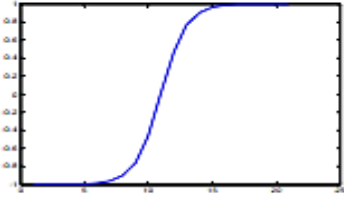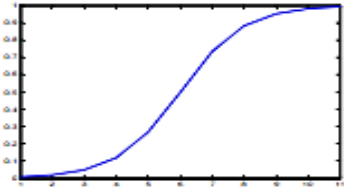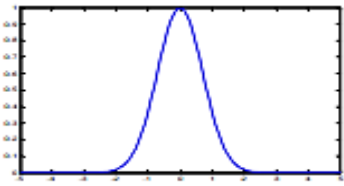
W_{ij} : the weight that links the processing unit between two successive layers, there are also default values for the weights within the program.

3. Transfer function: It is translating the input signal to the output signal using one of the transfer functions. Where this function converts the result of the weighted summation process in the previous step to a value confined to a specific range. The value is called the threshold value, so that the output is determined and applied to the set, the output of this network is confined to the range (0, 1) or the range (-1, +1). One of the most important Transfer functions that can be used in MATLAB 2013 are:

- Linear Function (Purelin): It is a linear function gives outputs equal to the weighted inputs of the processing unit.
- Sigmoid Function (tansig, logsig): This function is considered one of the most widely used functions, which gives outputs that are confined to either (0, 1) or (1, +1).
- Node Functions: There are no limitations to using the node function which can be used explicitly, the best function to use is the one that does the job best.

- Step Function: It is a random step function that used if the output value is less than the threshold value or the output value is greater than the threshold value.
- Gaussian functions: These functions are continuous, differentiable, and have asymptotic lines used in radial-based function networks. The curves of these functions are bell-shaped. Table E.1 show types of transfer functions.

Table E.1 Important types of transfer functions.

Function Name	Graphical Illustration	Mathematical form
Linear		$f(x) = x$
Hyperbolic Tangent Sigmoid		$f(x) = \dfrac{e^x - e^{-x}}{e^x + e^{-x}}$
Logistic Sigmoid		$f(x) = \dfrac{1}{1 + e^{-x}}$
Gaussian RBF		$\varphi_j(x) = \exp\left(-\dfrac{1}{2\sigma_j^2}\|x - x_j\|^2\right)$

4. Output function: After the summation function sums the weighted inputs and then the conversion function converts the summation output to a value

that is limited to a certain range, the output may be in most cases equal to the product of the transformation function.

The work of the processing unit can be summarized in neural network with the following steps :

1. Receiving the input data.

2. Modifying the signal entering the unit by means of weights.

3. Use the addition function to add the weights.

4. Determine the output signal generated by this unit by applying a specific activation function to the total weighted input data.

5. The output generated by this unit can be processes in several other processing units.

E.1.3 The architecture of ANN

The architecture of a neural network is the way in which processing units are linked to each other within each layer or between the different layers that make up the network. Neural networks can be distinguished by the number of layers and the form of interconnection between neurons (architectural) and the method that determines the weights of these correlations (training, learning, algorithms) and the type of activation function used. Network structures can be categorized according to the number of layers into:

- Single-Layer: it is one of the simplest types of network structures, and it consists of a single layer of processing elements that connect direct network inputs with their outputs.

- Multi-Layer: it is contained more than one layer of processing elements interconnected by the interfaces (weights), where the network consists of at least an input layer, one or more hidden layers, and an output layer.

Neural networks can be classified according to the nature of data spread and the type of interconnection between processing units into the following types .

- Forward: it is one of the most widely used networks. This network consists of the input layer, the hidden layers, and the output layer. The arithmetic operations are transmuted in the forward direction from the input layer to the output layer through the hidden layers.
- Feedback: in these networks the outputs become inputs and in a closed loop so that the best results are given.
- Auto Associative: in this type of network, the inputs and outputs operate at the same time, that is, they work in opposite directions.
- Self-Organizing Maps: these networks are used to deal with unexpected and changing circumstances, and they do not have a specific target and these networks follow the method of self-learning.
-

E.1.4 Root Mean Squared Error

Root Mean Squared Error (RMSE): it gives data on short-term performance, which is defined as the deviation of predicted values around the measured data. The lower of the root mean square error (RMSE) is the more accurate in the estimation.

$$\text{MSE} = \sqrt{\frac{\sum_{i=1}^{n}(\text{actual efficiency} - \text{predicted efficiency})^2}{n}} \qquad \text{(E.2)}$$

$$R^2 = 1 - \frac{\sum_{i=1}^{n}(\text{actual efficiency} - \text{predicted efficiency})^2}{\sum_{i=1}^{n}\text{predicted efficiency}^2} \qquad \text{(E.3)}$$

E.2 Data collection

After performing the calculations on the data of the practical part of the current research. The data was collected and prepared, which represents the first step in the design of neural network models and selects the T_{in}, T_{amb}, Tr and I_r data as inputs to the neural network data and represents the thermal efficiency as the output of the neural network. as shown in Table E.2

Table E.2 Select data of the neural network

NO	Tin, (č)	Tamb. (č)	I (w/m2)	Tr (č)	η%	NO.	Tin, (č)	Tamb (č).	I (w/m2)	Tr (č)	η%
1	15.2	9.3	378.7	20.3	13.42	79	17.6	11.6	425.8	26.2	20.36
2	15.8	8.6	448.7	24.8	17.39	80	20.3	12.4	518.5	31.2	22.27
3	17.6	9.6	522.5	31.6	27.04	81	22.4	14.2	622.6	42.2	30.10
4	21.1	11.4	610.5	40.5	37.33	82	25.8	16.8	705.7	49.2	32.14
5	24.6	13.7	678.2	47.2	39.41	83	29.1	18.1	768.9	56.2	43.47
6	26.2	17.3	763.8	50.1	37.79	84	34.8	20.1	820.8	62.1	49.81
7	31.4	23.7	823.6	53.8	43.72	85	36.2	22.4	855.3	69.3	53.22
8	32.1	27.2	857.8	54.6	45.33	86	40.6	23.3	863.9	72.2	48.04
9	34.3	24.8	835.3	56.2	38.77	87	42.3	24.1	849.8	71	43.77
10	35.2	24.1	762.2	56	36.11	88	44.2	21.5	812.9	74.1	37.40
11	37.4	22.6	647.5	55.2	38.88	89	43.1	19.6	744.3	72.3	36.06
12	38.4	21.2	558.4	52.7	32.53	90	41.8	17.8	694.5	68.6	33.01
13	35.6	22.6	487.2	49.8	30.31	91	39.6	17.1	632.8	64.5	23.80
14	16.3	10.2	397.5	22.1	14.00	92	19.2	9.8	380.3	23.2	25.31
15	18.6	11.6	481.6	26.2	16.06	93	21.2	10.3	487.1	26.1	23.71
16	19.1	12.9	570.7	33.4	22.85	94	23.7	13.4	596.4	35	29.03
17	21.8	14.8	643.8	41.3	26.98	95	26.8	15.2	698.3	40.7	32.37
18	23.1	18.2	730.3	48.9	31.02	96	29.7	17.6	796.5	52	38.03
19	24.9	22.8	805.5	52.1	36.77	97	33.8	20.1	825.8	56.6	43.66
20	26.7	24.2	822.7	54.2	44.45	98	37.2	23.5	852.4	59.3	48.50
21	29.2	25.1	838.3	56.1	42.44	99	41.6	24.4	878.8	61.3	49.78
22	31.6	25.7	794.1	56.8	39.93	100	43.3	25.5	852.8	63.5	41.72
23	34.3	25.3	713.6	57.2	37.68	101	45.1	22.7	820.9	62.1	39.24
24	36.1	24.8	637.4	55.8	38.03	102	42.3	19.8	773.1	59.1	33.58
25	35.2	24.1	570.4	53.6	34.10	103	39.6	18.5	685.4	54.1	32.26

E-8

26	33.6	23.6	497.5	51.4	28.02	104	36.7	18	576.8	49.4	25.84
27	15.8	9.3	433.6	21.6	12.56	105	19.6	17.6	418.4	24.7	12.95
28	17.2	11.3	476.3	26.4	17.52	106	21	18.2	487.2	29.6	19.44
29	18.2	14.8	560.6	33.6	24.57	107	22.9	19.6	552.3	36.6	26.61
30	19.6	16.2	617.7	42.4	29.32	108	26.1	20.7	646.7	45.2	34.16
31	20.3	18.6	684.7	49.2	33.84	109	30.9	21	738.2	50.7	39.24
32	22.5	26.4	760.2	51.4	34.26	110	32.2	22.2	828.4	56.3	43.64
33	25.6	23.1	831.5	54.8	37.81	111	35.7	23.8	826.5	61.1	44.87
34	27.3	21.3	818.1	58.6	40.60	112	39.8	26.1	863.8	64.6	46.35
35	30.1	20.9	727.6	57.1	41.65	113	41.9	24.8	842.4	66.8	45.11
36	31.6	20.8	641.5	56.8	40.48	114	44.2	25.2	786.2	65.4	43.83
37	33.7	18.9	609.2	56.2	38.48	115	45.4	23.2	718.6	64.2	40.74
38	32.4	19.6	535.9	53.4	31.65	116	43.7	22.8	626.3	60.3	36.64
39	31.5	18.2	443.6	52.1	27.67	117	42.6	22.2	558.6	56.7	29.42
40	16.7	10.1	412.6	23.1	19.94	118	18.6	19.5	452.3	25	13.81
41	18.3	9.6	478.3	27.6	20.22	119	18.9	20.7	527.7	28.5	15.91
42	20.3	10.8	575.6	32.8	25.18	120	20.3	21.8	616.4	34	22.55
43	21.1	13.3	637.5	40.2	29.54	121	22.4	23.1	694.8	42.6	29.98
44	22.8	15.4	705.7	50.4	36.25	122	25.1	22.1	780.7	46.5	35.53
45	24.1	14.5	733.6	53.2	39.45	123	30.7	23.8	833.2	51.7	39.54
46	26.2	15.2	776.6	58.3	39.70	124	35.3	24.7	852.7	58.5	45.00
47	30.1	16.4	826.1	60.5	36.69	125	38.7	27.2	872.3	62.6	47.21
48	32.9	24	759.4	61.2	31.03	126	41.2	26.3	841.9	63.7	47.19
49	33.4	20.6	667.9	58.6	33.13	127	43.2	23.4	786.3	64	41.72
50	32.6	21	657.8	56.1	31.45	128	42.6	22.4	725.9	62	40.31
51	31.8	19.2	578	53.2	25.82	129	40.8	21.6	614.9	59.3	33.70
52	30.5	19.1	458.5	48.4	23.11	130	37.4	21.1	546.8	55.4	30.53
53	16.1	10.2	447.5	24.4	11.91	131	19.3	17.3	414.3	25	17.40
54	17.7	12.8	546.4	30.8	20.12	132	19.7	18.5	478.7	28.5	18.80
55	21.6	15.4	634.3	40.1	28.19	133	20.3	19.8	546.4	34	30.28
56	25.1	16.5	712.5	46.6	34.24	134	22.5	21.4	631.8	42.6	31.84
57	28.6	18.8	781.8	51.6	39.97	135	24.7	22.9	705.7	46.5	42.18
58	31.3	20.6	820.5	57.5	48.98	136	27.8	21.7	787.2	51.7	43.67
59	33.7	22.6	844.3	64.3	51.26	137	32.6	23.6	824.7	58.5	44.23
60	37.3	23.7	850.3	67.6	54.55	138	37.8	25.7	840.3	62.6	45.49
61	40.7	24.7	836.7	68.7	53.29	139	41.6	26.6	823.9	63.7	39.87
62	44.3	21.2	796.2	69.6	49.80	140	43.3	24.8	767.3	64	37.71
63	45.8	20.4	753.8	67.8	43.54	141	40.8	23.1	755.9	62	33.11
64	44.3	19.1	686.5	65.2	37.36	142	38.6	22.5	694.9	59.3	27.81

| 65	43.2	18.7	628.6	58.2	29.38	143	36.8	20.9	606.8	55.4	21.25
66	14.6	9.3	491.6	28.6	14.19	144	20.4	18.3	479	23.4	18.05
67	15.2	11.6	546.4	31.2	18.47	145	22.8	19.8	562	28.7	17.93
68	18.8	12.5	600.8	42.6	28.35	146	24.9	21.3	750.6	34.2	20.44
69	21	14.7	676.9	47.5	37.52	147	27.2	22.7	768.2	42.9	27.43
70	25.5	13.3	798.4	55.3	41.07	148	30.1	24.4	833.9	46.5	33.26
71	29.8	14.8	876.4	61.7	43.90	149	32.3	26.6	886.7	52.7	36.08
72	34.2	18.6	934.6	67.1	47.23	150	34.4	27.8	896.5	58.8	37.76
73	38.5	20.3	861.5	69.2	54.22	151	38.2	27.2	835	63.6	44.49
74	43.8	21.8	834.9	72.8	50.75	152	40.7	25.6	796	64.8	36.48
75	47.6	19.2	795.3	73.1	47.27	153	39.8	24.5	732	64	37.09
76	47.1	18.6	736.5	71.6	41.03	154	37.4	23.7	615	62.5	39.53
77	45.1	18.2	647.4	66.2	38.24	155	35.8	22.4	523	59.6	36.49
78	42.9	17.4	588.1	62.1	29.17	156	33.4	21.5	436	55.4	32.85

E.3 Data pre-processing

After data collection, the data is prepared by performing data normalization, distribution and exclusion of anomalous data to obtain better neural network training and more accurate thermal efficiency.

E.4 ANN Structure

The artificial neural network model was built using MATLAB 2016, where the structure consists of an input layer consisting of four parameters (Tin, T_{amb}, T_r and I_r) and an output layer with one output (η), and two hidden layers. The number of neurons was calculated according to Equation 3.7. In this work, a neural network model containing the number of neurons, the Figure E.3.a. shows the structure 4-2-2-1 and the Figure E.3.b shows the structure 4-9-9-1 was use in this work.
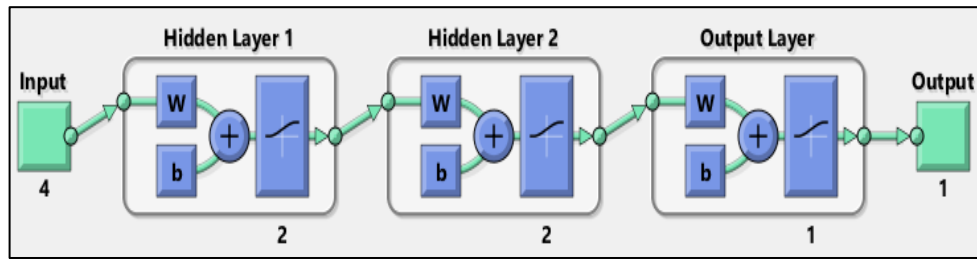
(a)
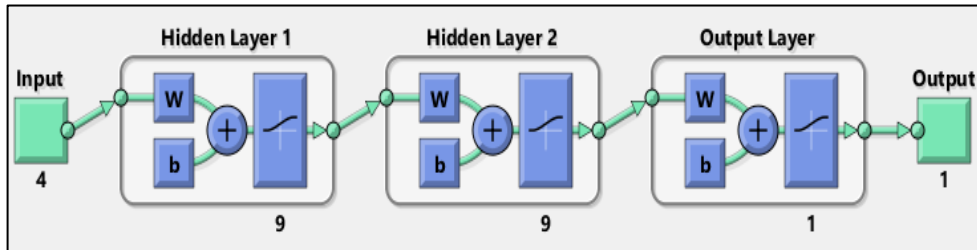
(b)

Figure E.3 Structure artificial neural network model (a) Structure (4-2-2-1), (b) Structure (4-9-9-1).

E.5 Data Training

After preparing the data and building the appropriate neural network, the process of training the network model is carried out using nn-tool in MATLAB program. To get the best neural network architecture, the data is divided into a training set of 70% of the total data, a check set of 15% of the total data, and a comparison set of 15% of the total data as shown in Figure E.4
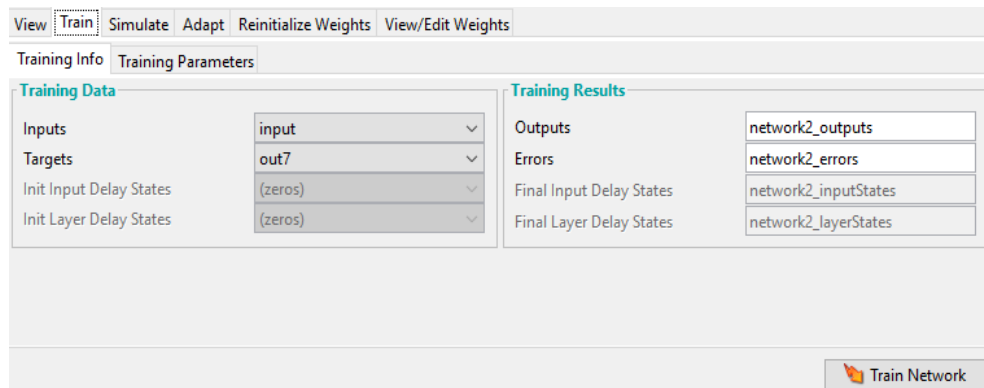

Figure E.4 Toolbox of Training data in MATLAB program.

E.6 Predicting the Thermal efficiency

The 4-2-2-1 neural network architecture, which has been trained and shows that the best thermal efficiency prediction model is with the best performance validation 0.040726 at epoch 68 as shown in Figure D5.a

The 4-9-9-1 neural network architecture trained and shows that the best thermal efficiency prediction model with the best performance validation is 0.0049769 at epoch 178 as shown in Figure E.5.b
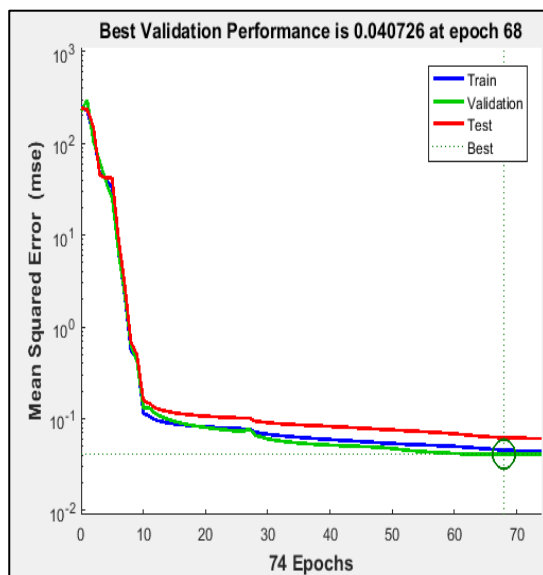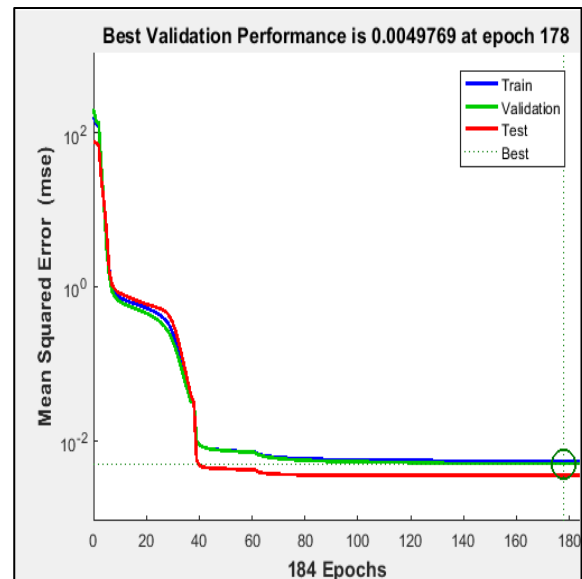
(a)   (b)

Figure E.5 Best validation performances in thermal efficiency (a) for ANN structure 4-2-2-1 and (b) for ANN structure 4-9-9-1.

Table: E.3 Comparison of Testing ANN results with the experimental data

NO.	η% , exp.	η%, ANN 4-2-2-1	η%, ANN 4-9-9-1	Difference,% 4-2-2-1	Difference ,% 4-9-9-1
1	30.28	22.52	24.42	8.451	72.086
2	31.84	29.16	30.03	2.972	90.665
3	42.18	32.95	37.25	13.071	69.015
4	43.67	38.25	41.40	8.245	81.119
5	44.23	42.31	43.47	2.743	93.798
6	45.49	43.50	45.43	4.438	90.244
7	39.87	42.74	42.35	0.926	97.679
8	37.71	41.05	38.56	6.060	83.929
9	33.11	40.23	34.21	14.958	54.821
10	27.81	37.21	31.20	16.152	41.911
11	21.25	32.45	28.05	13.567	36.143
12	18.05	16.98	14.99	11.684	35.286
13	17.93	19.34	18.11	6.372	64.471
14	20.44	26.26	22.02	16.175	20.873
15	27.43	31.42	26.98	14.149	48.418
16	33.26	34.75	33.33	4.082	87.727
17	36.08	40.10	38.64	3.646	89.894
18	37.76	43.50	45.08	3.629	90.389
19	44.49	43.77	43.19	1.328	97.015
20	36.48	43.01	38.75	9.905	72.851
21	37.09	41.24	35.36	14.251	61.574
22	39.53	37.53	31.04	17.279	56.292
23	36.49	33.24	29.15	12.318	66.242
24	32.85	28.92	27.09	6.330	80.734

الخلاصة

تم تصنيع و اختبار مجمع الطاقة الشمسية المركز بشكل تجريبي لتحسين الكفاءة الحرارية لمجمع الطاقة الشمسية. تم استخدام ثلاثة موائع عمل مختلفة (ماء ، ماء مقطر مع جسيمات اوكسيد النحاس النانوية ، ماء مقطر مع جسيمات اوكسيد التيتانيوم النانوية) بتركيز حجمي قدره 0.02. أجريت الاختبارات التجريبية في جامعة الأنبار ـ الرمادي (32.559 درجة شمالاً ـ 41.9196 درجة شرقاً) خلال أيام محددة من شهر يناير 2021 إلى شهر مارس 2021 اثناء وقت النهار (9 صباحاـ 15 مساءا). تم حساب ثلاث مؤشرات رئيسية: درجة حرارة المائع الخارجة ، والطاقة المفيدة و الكفاءة الحرارية بتطبيق تأثير معدل التدفق الكتلي من (30 إلى 80) لتر/ ساعة. تم محاكاة للنتائج التجريبية باستخدام برنامج الماتلاب وذلك باقتراح شبكة عصبية اصطناعية للتنبؤ بالكفاءة الحرارية لمجمع الطاقة الشمسية. يتكون نموذج الشبكة العصبية الاصطناعية من أربعة مدخلات ومعلمة إخراج واحدة. تتضمن معلمات الإدخال درجة حرارة المائع الداخل ، شدة الاشعاع الشمس المقاسة، ودرجة حرارة الجو ودرجة حرارة اللوح الماص (انبوب الاستقبال). بينما تتضمن معلمة الإخراج الكفاءة الحرارية. تم بناء نموذجين للشبكة العصبية (1-2-2-4) و (1-9-9-4). أظهرت النتائج التجريبية ان مائع اوكسيد النحاس النانوي سجل أقصى زيادة في الكفاءة الحرارية حوالي 19.2٪ بينما مائع اوكسيد التيتانيوم النانوي سجل أقصى زيادة في الكفاءة الحرارية حوالي 7.12٪ مقارنة بالماء.

UNIVERSITY OF ANBAR

التحقيق التجريبي لتحسين انتقال الحرارة في مجمّع شمسي ذو القطع المكافئ باستخدام موائع نانوية

رسالة مقدمة

الى كلية الهندسة – جامعة الانبار

وهي جزء من متطلبات نيل شهادة الماجستير في علوم

الهندسة الميكانيكية

أعداد

تحسين علي صالح

(بكالوريوس هندسة ميكانيك ـ 2004)

بأشراف

أ.م .د. ستار عبد مطلك   أ.م .د. هيثم كامل داود

1443 هـ   2021 م